NANYANG TECHNOLOGICAL UNIVERSITY
SINGAPORE

STRUCTURAL PERFORMANCE AND ANALYSES OF S960 ULTRA-HIGH STRENGTH STEEL WELDED I-SECTION MEMBERS

ANDI SU

SCHOOL OF CIVIL AND ENVIRONMENTAL ENGINEERING

2021

Structural Performance and Analyses of S960 Ultra-High Strength Steel Welded I-Section Members

Andi Su

School of Civil and Environmental Engineering

A thesis submitted to the Nanyang Technological University
in partial fulfilment of the requirements for the degree of
Doctor of Philosophy

Statement of Originality

I hereby certify that the work embodied in this thesis is the result of original research, is free of plagiarised materials, and has not been submitted for a higher degree to any other University or Institution.

Andi Su.

. . . . 20/01/2022. . . . . .

. . . . . .

Su Andi

Supervisor Declaration Statement

I have reviewed the content and presentation style of this thesis and declare it is free of plagiarism and of sufficient grammatical clarity to be examined. To the best of my knowledge, the research and writing are those of the candidate except as acknowledged in the Author Attribution Statement. I confirm that the investigations were conducted in accord with the ethics policies and integrity standards of Nanyang Technological University and that the research data are presented honestly and without prejudice.

. . . 20/01/2022. . . . . .

. . . . . .

Zhao Ou

Authorship Attribution Statement

This thesis contains material from 4 papers published (or accepted) and 2 papers submitted in the following peer-reviewed journals in which I am listed as an author.

Chapter 3 is published as A. Su, Y. Sun, Y. Liang, and O. Zhao. Membrane residual stresses and local buckling of S960 ultra-high strength steel welded I-section stub columns. *Thin-Walled Structures* **161**, 107497 (2021). DOI: 10.1016/j.tws.2021.107497.

The contributions of the co-authors are as follows:

- Dr Zhao provided the initial research direction.
- I prepared the manuscript drafts. The manuscript was revised by Dr Zhao.
- I co-designed the test plan with Dr Zhao and performed all the physical testing at laboratories of CEE. I also analysed the data.
- Dr. Sun provided guidance in the interpretation of the experimental data and Dr. Liang provided guidance in numerical modelling part.

Chapter 4 is published as A. Su, Y. Liang, and O. Zhao. Experimental and numerical studies of S960 ultra-high strength steel welded I-section columns. *Thin-Walled Structures* **159**, 107166 (2021). DOI: 10.1016/j.tws.2020.107166

The contributions of the co-authors are as follows:

- Dr Zhao provided the initial research direction.
- I prepared the manuscript drafts. The manuscript was revised by Dr Zhao.
- I co-designed the test plan with Dr Zhao and performed all the physical testing at laboratories of CEE. I also analysed the data.
- Dr. Liang provided guidance in the interpretation of the experimentally

measured data.

Chapter 5 is submitted as A. Su, Y. Liang, and O. Zhao. Experimental and numerical studies of S960 ultra-high strength steel slender welded I-section columns prone to local–global interactive buckling. *Thin-Walled Structures* (2021), Under Review.

The contributions of the co-authors are as follows:

- Dr Zhao provided the initial research direction.
- I prepared the manuscript drafts. The manuscript was revised by Dr Zhao.
- I co-designed the test plan with Dr Zhao and performed all the physical testing at laboratories of CEE. I also analysed the data.
- Dr Liang provided guidance in the interpretation of the experimentally measured data.

Chapter 6 is published as
(i) A. Su, Y. Sun, Y. Liang, and O. Zhao. Experimental and numerical studies of S960 ultra-high strength steel welded I-sections under combined compression and minor-axis bending. *Engineering Structures* 243, 112675 (2021). DOI: 10.1016/j.engstruct.2021.112675

(ii) A. Su, Y. Sun, O. Zhao and Y. Liang. Local buckling of S960 ultra-high strength steel welded I-sections subjected to combined compression and major-axis bending. *Engineering Structures* 248, 113213 (2021). DOI: 10.1016/j.engstruct.2021.113213

The contributions of the co-authors are as follows:

- Dr Zhao provided the initial research direction.
- I prepared the manuscript drafts. The manuscript was revised by Dr Zhao.
- I co-designed the test plan with Dr Zhao and performed all the physical testing

at laboratories of CEE. I also analysed the data.

- Dr Liang provided guidance in the interpretation of the experimentally measured data.
- Dr Sun helped to perform the parametric studies in numerical modelling part.

Chapter 7 is submitted as A. Su, Y. Liang. and O. Zhao. S960 ultra-high strength steel slender welded I-section beam-columns: Testing, modeling and design, *Thin-Walled Structures* (2021), Under Review.

The contributions of the co-authors are as follows:

- Dr Zhao provided the initial research direction.
- I prepared the manuscript drafts. The manuscript was revised by Dr Zhao.
- I co-designed the test plan with Dr Zhao and performed all the physical testing at laboratories of CEE. I also analysed the data.
- Dr Liang provided guidance in the interpretation of the experimentally measured data.

Andi Su.

. . 20/01/2022 . . . .

Su And

ACKNOWLEDGEMENTS

The research work presented in this PhD thesis was conducted under the supervision of Dr Ou Zhao, Assistant Professor in the School of Civil and Environmental Engineering at Nanyang Technological University. I would like to give my deepest gratitude to him for his highly professional guidance, invaluable advice and continuous encouragement and emotional support throughout my whole PhD career. The academic collaborations with Dr Yating Liang at University of Glasgow, Dr An He at South China University of Technology and Dr Yao Sun at Nanyang Technological University, are also greatly appreciated.

The support of all the technicians in the Construction Technology Laboratory and the Protective Engineering Laboratory at Nanyang Technological University, where the testing programmes presented in this PhD thesis were carried out, is greatly acknowledged.

I am thankful to the financial support from the NTU Research Scholarship. I cannot also miss the opportunity to thank all of my friends and colleagues at Nanyang Technological University, whose company and encouragement make my PhD a fantastic experience.

Finally, I would like to express my heartfelt gratitude to my parents Delin Su and Xue Bai for their unconditional love and continuous encouragement. This work is dedicated to them with all my sincere love.

Table of Contents

ACKNOWLEDGEMENTS i
ABSTRACT vi
LIST OF PUBLICATIONS viii
LIST OF TABLES x
LIST OF FIGURES xii
LIST OF SYMBOLS xvii
CHAPTER 1 – Introduction 1
1.1 Background 1
1.2 Structural applications 2
1.3 Research objectives 5
1.4 Thesis outline 5
CHAPTER 2 – Literature Review 8
2.1 Introduction 8
2.2 International design codes 8
2.3 Previous research on high strength steel and ultra-high strength steel welded I-sections 9
2.3.1 Material properties 9
2.3.2 Local buckling behaviour 13
2.3.3 Global instability 19
2.4 Concluding remarks 24
CHAPTER 3 – Membrane Residual Stresses and Local Buckling of S960 Ultra-High Strength Steel Welded I-Section Stub Columns 26
3.1 Introduction 26
3.2 Testing 27
3.2.1 General 27
3.2.2 Material testing 27
3.2.3 Membrane residual stress measurements 30
3.2.4 Initial geometric imperfection measurements 38
3.2.5 Stub column tests 40
3.3 Numerical modelling 43

3.3.1 General 43
3.3.2 Development of FE models 44
3.3.3 Validation of FE models 45
3.3.4 Parametric studies 48
3.4 Evaluation of existing design codes 48
3.4.1 General 48
3.4.2 Slenderness limits for cross-section classification 49
3.4.3 Cross-section compression resistances 53
3.5 Concluding remarks 57
CHAPTER 4 – Flexural Buckling of S960 Ultra-High Strength Steel Welded I-Section Columns 58
4.1 Introduction 58
4.2 Testing 59
4.2.1 General 59
4.2.2 Initial geometric imperfection measurements 61
4.2.3 Pin-ended column tests 63
4.3 Numerical modelling 68
4.3.1 General 68
4.3.2 Development of FE models 68
4.3.3 Validation of FE models 71
4.3.4 Parametric studies 75
4.4 Assessment of international design standards and development of new design method 78
4.4.1 General 78
4.4.2 EN 1993-1-12 (EC3) 78
4.4.3 ANSI/AISC 360-16 (AISC) 81
4.4.4 AS 4100 (AS) 83
4.4.5 Revised EC3 design approach 85
4.5 Concluding remarks 85
CHAPTER 5 – Local–Flexural Interactive Buckling of S960 Ultra-High Strength Steel Slender Welded I-Section Columns 87
5.1 Introduction 87

5.2 Testing 88
5.2.1 General 88
5.2.2 Initial geometric imperfection measurements and pin-ended column tests 89
5.3 Numerical modelling 94
5.3.1 General 94
5.3.2 Development of FE models 94
5.3.3 Validation of FE models 96
5.3.4 Parametric studies 99
5.4 Assessment of current design standards and development of new design approach 100
5.4.1 General 100
5.4.2 EN 1993-1-12 (EC3) 101
5.4.3 ANSI/AISC 360-16 (AISC) 104
5.4.4 AS 4100 (AS) 106
5.4.5 New design proposal 108
5.5 Concluding remarks 109
CHAPTER 6 – Local Buckling of S960 Ultra-High Strength Steel Welded I-Section Stub Columns under Combined Loading 110
6.1 Introduction 110
6.2 Testing 111
6.2.1 General 111
6.2.2 Initial local geometric imperfection measurements and eccentric compression tests 114
6.3 Numerical modelling 124
6.3.1 General 124
6.3.2 Development of FE models 124
6.3.3 Validation of FE models 125
6.3.4 Parametric studies 131
6.4 Evaluation of current design standards 133
6.4.1 General 133
6.4.2 EN 1993-1-12 (EC3) 133

6.4.3 ANSI/AISC 360-16 (AISC) 138
6.4.4 AS 4100 (AS) 142
6.5 Concluding remarks 144
CHAPTER 7 – Buckling of S960 Ultra-High Strength Steel Welded I-Section Beam-Columns 146
7.1 Introduction 146
7.2 Testing 147
7.2.1 General 147
7.2.2 Beam-column tests 148
7.3 Numerical modelling 153
7.3.1 General 153
7.3.2 Development of FE models 153
7.3.3 Validation of FE models 154
7.3.4 Parametric studies 157
7.4 Assessment of current design standards 158
7.4.1 General 158
8.4.2 EN 1993-1-12 (EC3) 159
7.4.3 AS 4100 (AS) 161
7.4.4 ANSI/AISC 360-16 (AISC) 163
7.4.5 Improved design approach 164
7.5 Concluding remarks 166
CHAPTER 8 – Conclusions and Suggestions for Future Research Work 168
8.1 Conclusions 168
8.2 Suggestions for future research 171
REFERENCES 173

ABSTRACT

Ultra-high strength steel grade S960, with the nominal yield stress of 960 MPa, has been gaining increasing attention and possesses high potential to be extensively utilised in high-rise and long-span structural applications, primarily due to its unique mechanical advantage of superior strength-to-weight ratio, which provides the possibility of design structural members with the reduced dimensions and self-weights. However, its actual use is restricted by the lack of appropriate design rules, since the current international design standards can only be applicable to steel components with material grades lower than S700. The behaviour and design analysis of S960 ultra-high strength steel welded I-section components under different loading cases are already out of their scopes and therefore the focus of this PhD thesis.

A comprehensive testing programme was firstly undertaken, which adopted eight welded I-sections made of S960 ultra-high strength steel. Material testing was conducted to derive the material stress–strain responses of S960 ultra-high strength steel, and membrane residual stresses were measured to determine the residual stress patterns and amplitudes in S960 ultra-high strength steel welded I-sections. At the cross-section level, a total of 16 concentrically loaded stub column tests and 20 eccentrically loaded stub column tests were carried out to investigate the cross-section resistances and local stability of S960 ultra-high strength steel welded I-sections. At the member level, 20 column tests, 8 beam-column tests as well as initial geometric imperfection measurements were conducted to study the global instability and resistances of S960 ultra-high strength steel welded I-sections. The testing programme was supplemented by a numerical modelling programme, where finite element models were initially developed and validated against the test results and

then adopted to conduct the extensive parametric studies to generate further numerical data over a wider range of cross-section dimensions, member lengths and loading combinations. The obtained test and numerical results were used to evaluate the applicability of the current design rules for S690 high strength steel welded I-section members under different loading cases to their S960 ultra-high strength steel counterparts (i.e. assessments of slenderness limits for cross-section classification, effective width expressions, column buckling curves and load-moment interaction curves). The evaluation results which demonstrate the applicability of the existing codified rules, and the newly proposed design methods provide the basis for the future revisions of international design codes for high strength steel structures.

LIST OF PUBLICATIONS

1. Su, A., Sun, Y., Liang, Y. and Zhao, O. (2020). Material properties and membrane residual stresses of S690 high strength steel welded I-sections after exposure to elevated temperatures. Thin-Walled Structures, 152, 106723.

2. Su, A., Liang, Y. and Zhao, O. (2021). Experimental and numerical studies of S960 ultra-high strength steel welded I-section columns. Thin-Walled Structures, 159, 107166.

3. Su, A., Sun, Y., Liang, Y. and Zhao, O. (2021). Membrane residual stresses and local buckling of S960 ultra-high strength steel welded I-section stub columns. Thin-Walled Structures, 161, 107497.

4. Su, A., Sun, Y., Liang, Y. and Zhao, O. (2021). Experimental and numerical studies of S960 ultra-high strength steel welded I-sections under combined compression and minor-axis bending. Engineering Structures, 243, 112675.

5. Su, A., Liang, Y. and Zhao, O. (2021). Post-fire behaviour and resistances of S690 high strength steel welded I-section stub columns. Thin-Walled Structures, 169, 108422.

6. Su, A., Sun, Y., Liang, Y. and Zhao, O. (2021). Local buckling of S960 ultra-high strength steel welded I-sections subjected to combined compression and major-axis bending. Engineering Structures, 248, 113213.

7. He, A., Su, A., Liang, Y. and Zhao, O. (2021). Experimental and numerical

investigations of circular recycled aggregate concrete-filled stainless steel tube columns. Journal of Constructional Steel Research, 179, 106566.

8. Sun, Y., Su, A., Jiang, K., Liang, Y. and Zhao, O. (2021). Testing, numerical modelling and design of stainless steel welded I-sections under minor-axis combined loading. Engineering Structures, 243, 112513.

9. Sun, Y., Liang, Y., Su, A. and Zhao, O. (2021). Local–flexural interactive buckling of S690 high strength steel slender welded I-section columns: Testing, modelling and design. Thin-Walled Structures, 166, 108064.

10. Su, A., Liang, Y. and Zhao, O. (2021). Experimental and numerical studies of S960 ultra-high strength steel slender welded I-section columns prone to local–global interactive buckling. Thin-Walled Structures, Under Review.

11. Su, A., Liang, Y., and Zhao, O. (2021). S960 ultra-high strength steel slender welded I-section beam-columns: Testing, modeling and design, Thin-Walled Structures, Under Review.

LIST OF TABLES

Table 2.1: Summary of existing tests on high strength steel and ultra-high strength steel welded I-sections prone to local buckling 17

Table 2.2: Summary of existing column and beam-column tests on high strength steel and ultra-high strength steel welded I-section members.....24

Table 3.1: Nominal material properties and chemical compositions of grade S960 ultra-high strength steel.....29

Table 3.2: Summary of key average measured material properties from S960 ultra-high strength steel longitudinal and transverse coupons.....30

Table 3.3: Normalised measured peak tensile and compressive membrane residual stresses of S960 ultra-high strength steel welded I-sections.....35

Table 3.4: Membrane residual stress predictive models. 36

Table 3.5: Measured geometric dimensions and initial local geometric imperfection magnitudes of S960 ultra-high strength steel welded I-section stub columns.....39

Table 3.6: Summary of key stub column test results. 43

Table 3.7: Comparisons of FE failure loads with test failure loads for varying initial local geometric imperfection magnitudes. 47

Table 3.8: Summary of EC3, AISC and AS slenderness limits between slender and non-slender plate elements in compression. 50

Table 4.1: Measured geometric dimensions and initial geometric imperfection magnitudes of S960 ultra-high strength steel welded I-section column specimens. 60

Table 4.2: Key test results for S960 ultra-high strength steel welded I-section column specimens. 68

Table 4.3: Comparisons of FE failure loads with test failure loads for varying global and local geometric imperfection magnitude combinations. 72

Table 4.4: Cross-section dimensions and effective member lengths of modelled S960 ultra-high strength steel welded I-section columns in parametric studies. 77

Table 4.5: Comparisons of test and numerical failure loads with flexural buckling resistance predictions. 80

Table 5.1: Measured geometric properties of S960 ultra-high strength steel slender welded I-section column specimens. 89

Table 5.2: Key experimental results for S960 ultra-high strength steel slender welded I-section column specimens. 91

Table 5.3: Comparisons of FE failure loads with test failure loads for different global and local geometric imperfection magnitude combinations. 97

Table 5.4: Comparisons of test and numerical failure loads with local–flexural interactive buckling resistance predictions. 103

Table 6.1: Measured geometric dimensions and initial local geometric imperfections of S960 ultra-high strength steel welded I-section stub column specimens under minor-axis combined loading.....113

Table 6.2: Measured geometric dimensions and initial local geometric imperfections of S960 ultra-high strength steel welded I-section stub column specimens under major-axis combined loading.....114

Table 6.3: Key minor-axis eccentric compression test results. 121

Table 6.4: Key test results for major-axis eccentric compression tests.....121

Table 6.5: Comparisons between test and numerical failure loads for different initial local geometric imperfection magnitudes of S960 ultra-high strength steel welded I-sections under minor-axis combined loading.....126

Table 6.6: Comparisons between test and numerical failure loads for different initial local geometric imperfection magnitudes of S960 ultra-high strength steel welded I-sections under major-axis combined loading.....126

Table 6.7: Comparisons of test and numerical failure loads with EC3, AISC and AS predicted failure loads for S960 ultra-high strength steel welded I-sections under minor-axis combined loading.....136

Table 6.8: Comparisons of test and numerical failure loads with EC3, AISC and AS predicted failure loads for S960 ultra-high strength steel welded I-sections under major-axis combined loading.....138

Table 7.1： Key geometric properties of S960 ultra-high strength steel welded I-section beam-column specimens.....148

Table 7.2: Key test results for S960 ultra-high strength steel welded I-section beam-column specimens.....150

Table 7.3: Comparison between test and numerical failure loads for measured and generalised initial global and local imperfection combinations. 157

Table 7.4: Comparisons of FE and test failure loads with AS, AISC and EC3 failure load predictions.....161

LIST OF FIGURES

Figure 1.1: Landmark Tower, Japan 3

Figure 1.2: Fast Bridge 48 Military Bridge, Sweden (Collin and Johansson, 2006) .3

Figure 1.3: Latitude Building, Australia 4

Figure 1.4: Sony Centre, Germany 4

Figure 3.1: Notations of welded I-section.....28

Figure 3.2: Tensile coupon test setup. 29

Figure 3.3: Measured stress–strain curves of S960 ultra-high strength steel longitudinal and transverse coupons. 30

Figure 3.4: Location of strips along specimen length direction (note that d is equal to b_f herein). 32

Figure 3.5: Locations and dimensions of strips within S960 ultra-high strength steel welded I-sections (dimension in mm). 32

Figure 3.6: Measured membrane residual stress patterns and amplitudes for S960 ultra-high strength steel welded I-sections I-200×150×6 and I-150×150×6. 34

Figure 3.7: Comparisons of measured membrane residual stresses in S960 ultra-high strength steel welded I-sections with predictive models.....37

Figure 3.8: Membrane residual stress distribution pattern for welded I-sections. 38

Figure 3.9: Test setup for initial local geometric imperfection measurements. 39

Figure 3.10: Stub column test setup. 41

Figure 3.11: Load–end shortening curves of S960 ultra-high strength steel welded I-section stub columns. 41

Figure 3.12: Local buckling failure modes of typical S960 welded I-section stub column specimens (from left to right: I-150×150×6-1 and I-90×70×6-1).....42

Figure 3.13: Typical membrane residual stress pattern and amplitudes (in MPa) in modelled S960 ultra-high strength steel welded I-section stub column I-150×150×6-1.....45

Figure 3.14: Experimental and numerical load–end shortening curves for typical S960 ultra-high strength steel welded I-section stub column specimens I-150×150×6-1 and I-90×70×6-1. 47

Figure 3.15: EC3 Class 3 limit for outstand plate elements in compression. 51

Figure 3.16: AISC limiting width-to-thickness ratio for outstand plate elements in

compression. 51

Figure 3.17: AS yield slenderness limit for outstand plate elements in compression. 52

Figure 3.18: EC3 Class 3 limit for internal plate elements in compression. 52

Figure 3.19: AISC limiting width-to-thickness ratio for internal plate elements in compression. 53

Figure 3.20: AS yield slenderness limit for internal plate elements in compression. 53

Figure 3.21: Comparisons of test and FE failure loads with EC3 cross-section compression resistance predictions. 55

Figure 3.22: Comparison of test and FE failure loads with AISC cross-section compression resistance predictions. 56

Figure 3.23: Comparison of test and FE failure loads with AS cross-section compression resistance predictions. 56

Figure 4.1: Notations of welded I-sections and locations of strain gauges attached to column specimens. 61

Figure 4.2: Illustration of initial local and global geometric imperfections. 62

Figure 4.3: Test setup for initial global geometric imperfection measurements.....63

Figure 4.4: Pin-ended column test setup. 66

Figure 4.5: Flexural buckling failure modes of typical S960 ultra-high strength steel welded I-section column specimens (from left to right: I1-L1, I1-L2, I1-L3, I1-L4 and I1-L5). 66

Figure 4.6: Load–mid-height lateral deflection curves for I-50×50×6 column specimens. 67

Figure 4.7: Load–mid-height lateral deflection curves for I-80×60×6 column specimens. 67

Figure 4.8: Typical membrane residual stress pattern and amplitudes (in MPa) in modelled S960 ultra-high strength steel welded I-section column I2-L4 (Positive values indicate tensile residual stresses while negative values indicate compressive residual stresses). 70

Figure 4.9: Test and numerical load–mid-height lateral deflection curves for S960 ultra-high strength steel welded I-section column specimen I1-L4. 72

Figure 4.10: Test and numerical load–mid-height lateral deflection curves for S960 ultra-high strength steel welded I-section column specimen I2-L3. 73

Figure 4.11: Test and numerical failure modes for S960 ultra-high strength steel welded I-section column specimen I1-L4. 74

Figure 4.12: Test and numerical failure modes for S960 ultra-high strength steel welded I-section column specimen I2-L3. 75

Figure 4.13: Comparisons of test and numerical failure loads with codified and revised design buckling curves. 80

Figure 4.14: Comparisons of test and numerical failure loads with flexural buckling resistance predictions from EN 1993-1-12 (CEN, 2007) and revised EN 1993-1-12 design approach. 81

Figure 4.15: Comparisons of test and numerical failure loads with flexural buckling resistance predictions from ANSI/AISC 360-16 (AISC, 2016) and revised EN 1993-1-12 design approach. 82

Figure 4.16: Comparisons of test and numerical failure loads with flexural buckling resistance predictions from AS 4100 (AS, 2016) and revised EN 1993-1-12 design approach. 84

Figure 5.4: Typical membrane residual stress pattern and amplitudes (in MPa) in modelled S960 ultra-high strength steel slender welded I-section column I1-L5 (Positive values indicate tensile residual stresses while negative values indicate compressive residual stresses). 95

Figure 5.5: Test and numerical load–mid-height lateral deflection curves for S960 ultra-high strength steel slender welded I-section column specimen I1-L3. 97

Figure 5.6: Test and numerical load–mid-height lateral deflection curves for S960 ultra-high strength steel slender welded I-section column specimen I1-L5. 98

Figure 5.7: Test and numerical failure modes for S960 ultra-high strength steel slender welded I-section column specimen I1-L3. 98

Figure 5.8: Test and numerical failure modes for S960 ultra-high strength steel slender welded I-section column specimen I1-L5. 99

Figure 5.9: Comparisons of test and numerical failure loads with EC3 design buckling curve. 103

Figure 5.10: Comparisons of test and numerical failure loads with local–flexural buckling resistance predictions from EC3 and revised EC3 design approach. 103

Figure 5.11: Comparisons of test and numerical failure loads with AISC design buckling curve. 105

Figure 5.12: Comparisons of test and numerical failure loads with local–flexural buckling resistance predictions from ANSI/AISC 360-16 (AISC, 2016). 105

Figure 5.13: Comparisons of test and numerical failure loads with AS design buckling curve.....107

Figure 5.14: Comparisons of test and numerical failure loads with local–flexural buckling resistance predictions from AS 4100 (AS, 2016).....108

Figure 6.1: Notations of welded I-section and locations of strain gauges for minor-axis combined loading. 112

Figure 6.2: Notations of welded I-section and locations of strain gauges for major-axis combined loading. 113

Figure 6.3: Measured initial local geometrical imperfection distributions for specimen A1.....115

Figure 6.4: Eccentric compression test setups. 116

Figure 6.5: Load–lateral deflection curves for minor-axis compression tests on S960 ultra-high strength steel welded I-section stub column specimens.....119

Figure 6.6: Load–lateral deflection curves for major-axis compression tests on S960 ultra-high strength steel welded I-section stub column specimens.....120

Figure 6.7: Failure modes of S960 ultra-high strength steel welded I-section stub column specimens under minor-axis eccentric compression. 122

Figure 6.8: Failure modes of S960 ultra-high strength steel welded I-section stub column specimens under major-axis eccentric compression. 123

Figure 6.9: Test and numerical load–lateral deflection curves of S960 ultra-high strength steel welded I-sections under minor-axis combined loading. 127

Figure 6.10: Test and numerical load–lateral deflection curves of S960 ultra-high strength steel welded I-sections under major-axis combined loading. 128

Figure 6.11: Test and numerical failure modes for specimens under minor-axis combined loading.....129

Figure 6.12: Test and numerical failure modes for specimens under major-axis combined loading.....130

Figure 6.13: Comparisons of test and FE data with EC3 design interaction curve for minor-axis combined loading.....136

Figure 6.14: Comparisons of test and FE data with EC3 design interaction curve for major-axis combined loading.....137

Figure 6.15: Comparisons of test and FE data with AISC design interaction curve for minor-axis combined loading.....141

Figure 6.16: Comparisons of test and FE data with AISC design interaction curve for major-axis combined loading.....141

Figure 6.17: Comparisons of test and FE data with AS design interaction curve for minor-axis combined loading.....143

Figure 6.18: Comparisons of test and FE data with AS design interaction curve for major-axis combined loading.....144

Figure 7.1: Beam-column test setup 149

Figure 7.2: Failure modes of I-150×75×6 beam-column specimens. 151

Figure 7.3： Failure modes of I-120×120×6 beam-column specimens. 151

Figure 7.4: Load–mid-height lateral deflection curves for I-150×75×6 beam-column specimens.....152

Figure 7.5: Load–mid-height lateral deflection curves for I-120×120×6 beam-column specimens.....152

Figure 7.6: Test and numerical failure modes for S960 ultra-high strength steel slender welded I-section beam-column specimen A2.....155

Figure 7.7: Test and numerical failure modes for S960 ultra-high strength steel slender welded I-section beam-column specimen B3.....155

Figure 7.8: Test and numerical load–mid-height lateral deflection curves for S960 ultra-high strength steel slender welded I-section beam-column specimen A2.....156

Figure 7.9: Test and numerical load–mid-height lateral deflection curves for S960 ultra-high strength steel slender welded I-section beam-column specimen B3.....156

Figure 7.10: Definition of θ. 159

Figure 7.11: Comparisons of test and numerical failure loads with AISC predicted failure loads.....161

Figure 7.12: Comparisons of test and numerical failure loads with AISC predicted failure loads.....163

Figure 7.13: Comparisons of test and numerical failure loads with AISC predicted failure loads.....164

Figure 7.14: Comparisons of test and numerical failure loads with predicted failure loads from new design approach.....166

LIST OF SYMBOLS

A	Gross cross-section area
A_{eff}	Effective cross-section area
$A_{eff,AISC}$	AISC effective cross-section area
$A_{eff,AS}$	AS effective cross-section area
$A_{eff,EC3}$	EC3 effective cross-section area
a, b, c, d	Distribution parameters of membrane residual stress model
b_f	Flange width of I-section
b_s	Distance between strain gauges attached to welded I-section
c	Flat width of plate element
c_{eff}	Effective width of plate element
c_f	Flat width of flange
C_{mz}	Equivalent uniform moment factor
c_w	Flat width of web
d_s	Distance between strain gauge and adjacent flange edge
E	Young's modulus
e_0	Initial loading eccentricity
f	Stress
f_c	Peak compressive residual stress in S960 ultra-high strength steel welded I-section
F_{cr}	AISC critical stress
f_t	Peak tensile residual stress in S960 ultra-high strength steel welded I-section
f_u	Ultimate stress of high strength steel and ultra-high strength steel
f_y	Yield stress of high strength steel and ultra-high strength steel
f_u/f_y	Ultimate-to-yield tensile stress ratio
h	Outer height of I-section

h_w	Clear distance between flanges
I	Second moment of area
k_c	ANSI/AISC 360-16 geometric factor
$k_{yy}, k_{yz}, k_{zy}, k_{zz}$	Eurocode interaction factor
k_σ	EN1993-1-5 buckling factor
L	Member length
L_e	Member effective length
L_m	Distance between the loading points in four-point bending tests
L_0	Nominal length between gauge holes
M_R	Cross-section bending moment resistance
M_{eff}	Effective cross-section bending moment capacity
$M_{eff,AISC}$	ANSI/AISC 360-16 effective cross-section bending moment capacity
$M_{eff,y,AISC}$	ANSI/AISC 360-16 effective cross-section bending moment capacity about major principal axis
$M_{eff,z,AISC}$	ANSI/AISC 360-16 effective cross-section bending moment capacity about minor principal axis
$M_{eff,AS}$	AS 4100 effective cross-section bending moment capacity
$M_{eff,y,AS}$	AS 4100 effective cross-section bending moment capacity about major principal axis
$M_{eff,z,AS}$	AS 4100 effective cross-section bending moment capacity about minor principal axis
$M_{eff,EC3}$	EN 1993-1-12 effective cross-section bending moment capacity
$M_{eff,y,EC3}$	EN 1993-1-12 effective cross-section bending moment capacity about major principal axis
$M_{eff,z,EC3}$	EN 1993-1-12 effective cross-section bending moment capacity about minor principal axis

M_{el}	Cross-section elastic moment capacity
$M_{el,y}$	Cross-section elastic moment capacity about major axis
$M_{el,z}$	Cross-section elastic moment capacity about minor axis
M_{pl}	Cross-section plastic moment capacity
$M_{pl,y}$	Cross-section plastic moment capacity about major axis
$M_{pl,z}$	Cross-section plastic moment capacity about minor axis
M_u	Failure bending moment
$M_{u,pred}$	Design ultimate cross-section bending moment resistance
$M_{u,1st,el}$	First-order elastic failure bending moment at mid-height
$M_{u,2nd,el}$	Second-order elastic failure bending moment at mid-height
$M_{u,2nd,inel}$	Second-order inelastic failure bending moment at mid-height
N_b	EC3 column buckling strength about minor principal axis
N_c	AS column buckling strength about minor principal axis
N_{eff}	Effective cross-section compression capacity
$N_{eff,AISC}$	AISC effective cross-section compression capacity
$N_{eff,AS}$	AS effective cross-section compression capacity
$N_{eff,EC3}$	EC3 effective cross-section compression capacity
N_R	Column flexural buckling resistance
N_{cr}	Euler buckling load
N_u	Failure load
$N_{u,AISC}$	AISC design compression resistance
$N_{u,EC3}$	EC3 design compression resistance
$N_{u,pred}$	Design ultimate compression resistance
P_s	AISC column buckling strength about minor principal axis
r_1	Reading of Demec gauge taken before sectioning
r_2	Reading of Demec gauge taken after sectioning
t	Plate thickness of I-section

t_f	Flange thickness of I-section
t_w	Web thickness of I-section
t_1	Length of temperature reference bar before sectioning
t_2	Length of temperature reference bar after sectioning
W_{eff}	Effective section modulus
$W_{eff,EC3}$	EN 1993-1-12 effective section modulus
$W_{eff,z}$	EN 1993-1-12 minor-axis effective section modulus
W_{el}	Elastic section modulus
$W_{el,y}$	Elastic section modulus about major axis
$W_{el,z}$	Elastic section modulus about minor axis
W_{pl}	Plastic section modulus
$W_{pl,y}$	Plastic section modulus about major axis
$W_{pl,z}$	Plastic section modulus about minor axis
α	Eurocode imperfection factor
α_a	AS 4100 compression member factor
α_b	AS 4100 member section constant
α_c	AS 4100 flexural buckling reduction factor
χ	Eurocode 3 reduction factor for global buckling
Δ	Mid-height lateral deflection of member
Δ_u	Mid-height lateral deflection of member at failure load
δ	Maximum deviation of curved strip
δ_b	AS 4100 moment amplification factor
δ_u	End shortening at failure
ε	Strain or Eurocode 3 material parameter
ε_{AISC}	ANSI/AISC 360-16 material parameter
ε_{AS}	AS 4100 material parameter
ε_c	Corrected relived strain

ε_{EC3}	EN1993-1-12 material parameter
ε_f	Fracture strain measured over standard gauge length of 50 mm
ε_{ln}^{pl}	Logarithmic plastic strain
ε_{nom}	Engineering strain
ε_u	Strain at ultimate stress
ε_y	Material yield strain
ε_0	Relieved strain
η	AS 4100 compression member imperfection factor
ψ	Stress ratio
κ	Curvature
$\bar{\lambda}$	Member non-dimensional slenderness
$\bar{\lambda}_{AISC}$	AISC member non-dimensional slenderness
$\bar{\lambda}_{AS}$	AS member non-dimensional slenderness
$\bar{\lambda}_{EC3}$	EC3 member non-dimensional slenderness
$\bar{\lambda}_l$, $\bar{\lambda}_p$	Plate element slenderness
λ_n	AS 4100 modified member slenderness
λ_{pf}	AISC compact limiting width-to-thickness ratio for flange
λ_{rf}	AISC non-compact limiting width-to-thickness ratio for flange
$\bar{\lambda}_{r,int}$	AISC limiting width-to-thickness ratio for internal plate elements
$\bar{\lambda}_{r,out}$	AISC limiting width-to-thickness ratio for outstand plate elements
λ_s	AS section slenderness
λ_{sy}	AS yield limits for most slender constituent plate element
ω_g	Initial global geometric imperfection magnitude of specimen
ω_0	Initial local geometric imperfection magnitude of specimen

ϕ	Eurocode 3 buckling parameter
ρ	Eurocode 3 reduction factor for plate width
σ_{nom}	Engineering stress
σ_{true}	True stress
θ	Angle parameter
ξ	AS 4100 buckling parameter

CHAPTER 1

INTRODUCTION

1.1 Background

Ultra-high strength steels, with the nominal yield stresses over 690 MPa, have been gaining popularity in the past decade, due to their superior strength-to-weight ratio (Shi et al., 2015; Wang et al., 2019; Li et al., 2019). In place of normal strength steels, the use of ultra-high strength steels can offer steel structures smaller cross-section dimensions and lighter self-weights, which are considered as the significant factors, especially in high-rise and long-span structures. Their use in the automotive industries is also expanding, for example, the load-bearing members of heavy lifting systems of truck-mounted cranes and container trailers are typically made of ultra-high strength steels. The characteristics of ultra-high strength steels will meanwhile facilitate the transportation, handing and disassembly of the structural members, featuring the lower long-term maintenance costs. However, their actual use in construction field is restricted by the absence of the experimental data on ultra-high strength steel components and lack of the efficient design provisions. Therefore, the experimental and numerical investigations on ultra-high strength steel members and the relevant design analyses (i.e. devising more accurate design approaches) are worthy of undertaking.

On the other hand, the relatively low ductility of ultra-high strength steels is also the key concern that may affect their popularisation in the construction industry. But recent advancements in manufacturing techniques have enabled the improvement of the ductility of ultra-high strength steels to an acceptable level by means of special

quenching and tempering, which indicates that ultra-high strength steels may also be adopted for general structural members. This thus prompted the current study on S960 ultra-high strength steel welded I-section components under different loading cases, with the aim of establishing the experimental data pool and devising the relating accurate design approaches in different countries.

1.2 Structural applications

The structures made of ultra-high strength steels S960 and S1100 and high strength steel S690 have risen throughout the world, particularly in Sweden, Japan, Australia and Germany. The Landmark Tower (Figure 1.1) in Japan, was built by adopting S690 high strength steel I-sections to structure columns, with the aim of reducing self-weights and hence the seismic reaction forces of the structure when subjected to earthquake loading. The Fast Bridge 48 Military Bridge in Sweden (Figure 1.2), was constructed using S960 ultra-high strength steel coupling plates and S1100 ultra-high strength steel decks, to achieve the strength requirements and reduce structure weights and fabrication costs. The Latitude Building (Figure 1.3) in Sydney employed concrete filled S690 high strength steel box sections in the transfer trusses to provide additional space inside the building. In the Sony Centre (Figure 1.4), Germany, S690 high strength steel was adopted in the roof truss to achieve the small component cross-sections and provide the envelope for fire protection.

Figure 1.1: Landmark Tower, Japan

(https://en.wikipedia.org/wiki/Yokohama_Landmark_Tower)

Figure 1.2: Fast Bridge 48 Military Bridge, Sweden (Collin and Johansson, 2006)

Figure 1.3: Latitude Building, Australia

(https://en.wikipedia.org/wiki/Latitude_(building))

Figure 1.4: Sony Centre, Germany

(https://www.sonycenter.de/en/architecture)

1.3 Research objectives

Up to date, there have been no available design provisions for ultra-high strength steel structures. Therefore, the applicability of the current design rules for high strength steel structures to ultra-high strength steel counterparts need to be evaluated and the relating efficient design approaches are necessary to be proposed.

Most of the current design provisions for high strength steel welded I-section components with the material grades up to S690 (or S700) were developed by directly mirroring those specified for normal strength steel counterparts, with the design accuracy evaluated by the extensive investigations on high strength steel welded I-section members under different loading cases. But in this thesis, the design of S960 ultra-high strength steel structures is out of their scopes and the applicability of the design provisions for S690 or S700 high strength steel welded I-sections to S960 counterparts needs to be assessed. Testing and analysis of S960 ultra-high strength steel welded I-sections under pure compression and combined loading, are therefore the objectives of this thesis, to provide the basis for the further development of the efficient design rules in different countries.

1.4 Thesis outline

There are 8 chapters in the present thesis, with the contents in each chapter summarised as follows. This chapter introduces the background of ultra-high strength steels and their actual engineering applications in the construction field. The research objectives of this thesis and the outline are also included.

Chapter 2 contains an extensive review of previous relevant studies, for the purpose of providing an overview of significant topics, including the existing experimental and numerical studies of high strength steel and ultra-high strength steel welded I-section components under various loading cases from the cross-section and member levels.

Chapter 3 describes thorough experimental and numerical investigations into the membrane residual stresses and local stability of S960 ultra-high strength steel welded I-section stub columns. An extensive laboratory testing programme is performed firstly, with the new predictive model for membrane residual stresses in S960 ultra-high strength steel welded I-sections proposed and concentrically loaded stub column tests conducted. This is followed by the numerical modelling study, in which the validation and parametric studies are carried out. The experimental and numerical results are adopted to evaluate the applicability of the codified provisions for S690 high strength steel welded I-section stub columns to S960 ultra-high strength counterparts.

Chapter 4 and Chapter 5 present the experimental and numerical investigations of minor-axis flexural buckling and local–flexural interactive buckling behaviour of S960 ultra-high strength steel welded I-section columns, respectively. In each chapter, the detailed experimental procedures, setups and key findings are reported. The numerical simulations are also conducted, with the aim of replicating the test observations. The obtained experimental and numerical results are adopted to evaluate the applicability of the design buckling curves and the codified design formulations to S960 ultra-high strength steel welded I-section columns. New design approaches are also proposed based on the European code.

Chapter 6 focuses on the cross-section behaviour and resistances of S960 ultra-high

strength steel welded I-section stub columns under combined compression and bending moment. A series of major-axis and minor-axis combined loading tests are conducted as part of the study, followed by the numerical simulations. On the basis of the experimentally and numerically derived results, the applicability of the design interaction formulations, as prescribed in the European, American and Australian standards, to S960 ultra-high strength steel welded I-sections under combined loading is evaluated.

Chapter 7 investigates the global instability of S960 ultra-high strength steel welded I-section beam-columns under minor-axis combined loading. A thorough testing programme, in conjunction with a systematic numerical modelling programme, is presented. The codified beam-column interaction curves and relating provisions are fully described; their applicability to S960 ultra-high strength steel counterparts is afterwards evaluated through comparing the results obtained from the codified rules against the derived experimental and numerical data.

Finally, the key findings of the current research and suggestions for future research work are summarised in Chapter 8.

CHAPTER 2

LITERATURE REVIEW

2.1 Introduction

A broad review of the previous relevant studies is presented in this chapter. As there are no available design standards for ultra-high strength steel (i.e. material yield stress over 690 MPa) structures, the development of international design codes (i.e. European code, American specification and Australian standard) for high strength steel structures, is firstly introduced. Existing research on high strength steel and ultra-high strength steel welded I-section components at the material, residual stress, cross-section and member levels, are then reviewed and summarised, together with the relating discussions of codified design rules and devised design approaches. Also, the research gaps of the previous research were also highlighted in the following sections, prompting the necessity of the current research work reported in this thesis.

2.2 International design codes

Currently, there are no available design standards for ultra-high strength steel structures, the corresponding existing design standards for high strength steel structures are therefore introduced. The European code EN 1993-1-12 (CEN, 2007), specifically for the design of high strength steel with material grades higher than S460 up to S700, was released in 2007, with most design rules directly mirroring those for normal strength steel structures. The American Institute of Steel Constructions (AISC) published the American specification, named as "Specification for Structural Steel Buildings" (AISC, 2016), in 2013 and revised it in 2016, specifically for high strength

steel structures with material yield stress up to 690 MPa. In Australia, the Australian standard AS 4100 (AS, 2016) was initially developed in 1998 and covered the steel design with the nominal yield stresses lower than 450 MPa; this is followed by the revision and extension of the application scope to material grades up to S690 in 2016.

2.3 Previous research on high strength steel and ultra-high strength steel welded I-sections

2.3.1 Material properties

2.3.1.1 Material response

The material properties for high strength steels with their yield stresses over 355 MPa and ultra-high strength steels with their yield stresses over 690 MPa are detailed in this section. For high strength steels and ultra-high strength steels, their stress–strain curves are similar to those of normal strength steels, featuring a linear elastic history until the attainment of the distinct yield point, the yield plateau and some strain hardening. Despite the higher yield stress, high strength steels and ultra-high strength steels own essentially the same elastic modulus E as normal strength steels. Previous literature (Li et al., 2015; Wang et al., 2017; Ban & Shi, 2018; Wang et al., 2019) in relation to S960 ultra-high strength steel and high strength steels revealed that the yield stress f_y is not increasing at the same degree as the ultimate tensile stress f_u. As a result, the ability of material strain hardening, normally represented by the ultimate-to-yield stress ratio f_u/f_y, decreases with the increased material grades. Empirical formulations between f_u/f_y and f_y, as defined in Equation (2.1) and Equation (2.2), were respectively proposed by Fukumoto (1998) and Langenberg (2008). Shi et al. (2016) also developed the multi-linear material constitutive model for high strength steels, defining material stress–strain responses, as given in Equation (2.3), where ε

and f are respectively the strain and stress, ε_y and ε_u are the strains at the yield and ultimate stresses, ε_h is the strain at the stress of $(f_y+f_u)/2$.

$$f_u / f_y = 0.83 + 203.8 / f_y \tag{2.1}$$

$$f_u / f_y = \left[1 - 0.72 e^{\left(-0.0027 f_y\right)}\right]^{-1} \tag{2.2}$$

$$\varepsilon = \begin{cases} \dfrac{f}{E} & \text{for } f \le 0.85 f_y \\ \dfrac{0.85 f_y}{E} + \dfrac{f - 0.85 f_y}{0.15 f_y}\left(\varepsilon_y - \dfrac{0.85 f_y}{E}\right) & \text{for } 0.85 f_y < f \le f_y \\ \varepsilon_y + \dfrac{f - f_y}{0.5\left(f_u - f_y\right)}\left(\varepsilon_h - \varepsilon_y\right) & \text{for } 0.5\left(f_y + f_u\right) < f \le f_u \\ \varepsilon_h + \dfrac{f - 0.5\left(f_u + f_y\right)}{0.5\left(f_u - f_y\right)}\left(\varepsilon_u - \varepsilon_h\right) & \text{for } f_y < f \le 0.5\left(f_y + f_u\right) \end{cases} \tag{2.3}$$

Ductility is another material property considered in structural design. The parameters adopted in EN 1993-1-1 (CEN, 2005) to place requirements on material ductility of steel grades up to S460 are given as (i) $f_u / f_y \ge 1.10$, (ii) $\varepsilon_u / \varepsilon_y \ge 15$ and (iii) $\varepsilon_f \ge 15\%$, where ε_f is the fracture strain.

In terms of high strength steels with material grades up to S700, the ductility requirements in EN 1993-1-12 (CEN, 2007) are relaxed and given as (i) $f_u / f_y \ge 1.05$, (ii) $\varepsilon_u / \varepsilon_y \ge 15$ and (iii) $\varepsilon_f \ge 10\%$.

In view of the fact that high strength steels and ultra-high strength steels own the lower ductility than that of normal strength steels, their plastic design and design of connections, in which the significant plastic deformation and thus force redistribution may occur, are restricted. But the plastic resistances at Class 1 and 2 sections (CEN, 2006) are still permitted to be exploited.

2.3.1.2 Toughness and weldability

The high strength steel and ultra-high strength steel structures should fulfil the toughness and weldability requirements in structural design. The toughness of material was highlighted in Langenberg et al. (2000) to be independent of steel grades, revealing that high strength steels can be regarded in the same way in this aspect. With regards to weldability, it is generally known that it can be deteriorated by the carbon content, however, the development of the new welding methods on high strength steels and ultra-high strength steels with low carbon contents can gradually eliminate this disadvantage (IABSE, 2005).

2.3.1.3 Residual stresses

Heat from welding may cause localized expansion, and when the finished weldment cools, some areas cool and contract more than other parts, leaving residual stresses. Residual stresses in high strength steel sections can lead to premature structural failure, stiffness loss and load-carrying capacity reductions. It is therefore crucial to investigate the residual stress patterns and magnitudes in these sections. The European convention ECCS (1976) and Swedish regulations BSK 99 (2003) provide residual stress models for normal strength carbon steel welded I-sections, specifying peak residual stress values and distributions. A review of previous studies on residual stresses in high strength steel welded, hot-finished and cold-formed sections is as follows and serves as a basis for the present investigation into membrane residual stresses in S960 ultra-high strength steel welded I-sections. Specifically, Wang et al. (2012a) and Ban et al. (2012) measured the residual stresses in S460 high strength steel welded I-sections, utilising hole-drilling method and sectioning method, respectively; based on the experimentally measured data, two residual stress models were proposed, highlighting the similar pattern to BSK and ECCS counterparts, but

lower peak compressive (and tensile) residual stress values and different distribution parameters. The membrane residual stresses in S690 high strength steel welded I-sections at room temperature and after exposure to elevated temperatures were measured by the authors and respectively reported in Sun et al. (2019a) and Su et al. (2020,2021g), where the effect of temperature on the membrane residual stress distribution pattern and amplitudes was studied and quantified and a three-stage predictive model, including a peak tensile membrane residual stress region, a peak compressive membrane residual stress region and a transition region (where peak tensile membrane residual stresses are changed to peak compressive membrane residual stresses), was proposed. Membrane residual stress measurements on S690 high strength steel welded I-sections were also conducted by Liu and Chung (2018) and Le et al. (2020) and similar three-stage membrane residual stress predictive models were proposed. Li et al. (2020) measured the membrane residual stresses in S960 ultra-high strength steel welded box-sections and I-sections, highlighted that the peak compressive and tensile membrane residual stresses were relating to the wall thickness and proposed a two-stage predictive model with no transition regions. Wang et al. (2016) measured the membrane residual stresses in hot-finished S690 high strength steel square and rectangular hollow sections and pointed out that the peak membrane residual stresses were equal to around $0.055f_y$ in tension and $0.031f_y$ in compression, which were significantly lower than those in S690 high strength steel welded I-sections. Ma et al. (2015) measured the membrane and bending residual stresses in S900 and S1100 high strength steel hollow sections fabricated from cold-forming and seam-welding and summarised that the membrane residual stresses were around $0.2f_y$ in comparison with the bending residual stresses of about $0.55f_y$.

Until now, research on residual stresses in S960 ultra-high strength steel welded I-sections remains limited, with the only available investigation reported in Li et al.

(2020), which therefore prompted the residual stress measurements on S960 ultra-high strength steel welded I-sections, one of the focuses in this thesis. Measurement approaches, key results and comparisons of proposed models with current codified models, are detailed in the following chapters.

2.3.2 Local buckling behaviour

2.3.2.1 Existing experimental studies

Local buckling is generally known as plate element buckling, without overall buckling of the member; it often occurs in thin-walled elements. In the past two decades, there has been a significant expansion in the applications of high strength steel welded I-sections, due to their simple cross-section shape and ease of fabrication, assembly and disassembly. Existing experimental studies into the cross-sectional response and resistances of high strength steel and ultra-high strength steel welded I-section structural components are reviewed in this sub-section. Table 2.1 summarises the previous stub column tests, three-point as well as four-point bending tests, and combined loading tests on high strength and ultra-high strength steel welded I-sections. Specifically, Shi et al. (2014) carried out the experimental and numerical studies on 9 S460 high strength steel welded I-section stub columns, and highlighted that (i) the local buckling stress and the ultimate stress decrease with the increasing plate slenderness and (ii) the current design methods in Europe, America and China were found conservative in terms of the cross-section resistances of S460 high strength steel welded I-section stub columns, especially for those with plate elements of high width-to-thickness ratios. Kim et al. (2012) and Yoo et al. (2013) performed stub column tests on S650 welded I-sections and compared the local buckling failure modes with those obtained from finite element models; based on the test and numerical results, the design slenderness limits were checked. Rasmussen and

Hancock (1992) conducted 6 stub column tests on S690 high strength steel welded I-sections, with results obtained from these high strength steel welded I-sections and the ordinary steel counterparts compared; the following conclusions were drawn – (i) the same yield slenderness limits can be applied to both ordinary and high strength steel plate elements, (ii) residual stress has less influence on stocky sections than slender sections and (iii) the inferior strain hardening property of high strength steel leads to the nondimensional strengths of stocky high strength steel welded I-sections less than those of stocky ordinary steel counterparts. Sun et al. (2019) also performed 16 stub column tests on S690 high strength steel welded I-sections, based on which, the slenderness limits and the cross-section capacities were checked against with the relating provisions in the international design standards, with their design accuracy and consistency highlighted. Kim et al. (2014) carried out the strength and residual stress evaluation of I-section stub columns fabricated from S800 high strength steel; the experimental results indicated that residual stress bears no relation to the yield stress of material and the impact of the residual stress on inelastic local buckling of S800 high strength steel welded sections is insignificant. Shi et al. (2015) conducted 4 stub column tests on S960 ultra-high strength steel welded I-sections, based on which, the conclusion that the American specification (AISC, 2016) and European code (CEN, 2007) were found not safe when the flanges are stocky and too conservative when plate elements become slender was drawn. Li et al. (2019) also conducted the experimental and numerical investigations on S960 ultra-high strength steel welded I-section stub columns; slenderness limits were highlighted to be conservative in all the considered standards, while American specification (AISC, 2016) were found to provide the closest predictions. Although extensive experimental and numerical studies of high strength steel welded I-section stub columns were performed, the investigations of membrane residual stresses and local buckling

behaviour of S960 ultra-high strength steel welded I-section stub columns remain scarce, thus one of the focuses of this thesis.

In terms of the flexural behaviour of high strength steel welded I-sections, Green et al. (2002) carried out 10 in-plane bending tests on S550 high strength steel welded I-sections, with the effects of various loading conditions (i.e. monotonic moment gradient, monotonic uniform moment and cyclic moment gradient) on the flexural behaviour and rotation capacities assessed, and the results were evaluated against the design criteria specified in the AISC-LRFD specifications (AISC, 1994), with some recommendations made for revising the specifications. Lee et al. (2013) conducted 8 three-point bending tests and 3 four-point bending tests on S650 high strength steel welded I-section members, with test results compared with the ordinary steel counterparts; the inferior rotation capacity and vulnerability to brittle fracture of high strength steel welded I-section beams were highlighted. McDermott (1969) carried out 9 beam tests on S690 high strength steel welded I-section members, with the conclusion of their sufficient rotation capacity drawn. Beg and Hladinik (1996) performed the thorough experimental and numerical investigations on the structural behaviour of S690 high strength steel welded I-section beams, the results of which were used to check the Class 3 slenderness limit, with the new proposal provided based on European code (CEN, 2007). S690 high strength steel welded I-section beams were also studied in Sun et al. (2019b), where 12 four-point in-plane bending tests were carried out, based on which, the accuracy of the codified provisions (i.e. slenderness limit and cross-section capacity) in European, American and Australian standards was assessed, with the advantages and disadvantages of the codified rules highlighted.

Combined loading tests were also conducted to study the local buckling behaviour of high strength steel welded I-section members. Sun et al. (2021a) conducted 10 eccentric compression tests on S690 high strength steel welded I-section stub columns, with 5 on major-axis combined loading and the other 5 on minor-axis combined loading. The experimental results, combined with the numerical results derived from the numerical modelling study, were used to assess the codified rules specified in the international standards, with their design accuracy and consistency evaluated. Kim et al. (2014) carried out 3 combined loading tests on S800 high strength steel welded I-section members, the results of which were adopted to assess the P–M interaction curve specified in American Specification (AISC, 2016), with its conservativity revealed. Until now, the structural behaviour and resistances of S960 ultra-high strength steel welded I-section stub columns under combined loading remain unexplored, and thus studied and reported in this thesis.

Table 2.1: Summary of existing tests on high strength steel and ultra-high strength steel welded I-sections prone to local buckling

Tests	Grade	Reference	No. of tests
Stub column tests	S460	Shi et al. (2014)	9
	S650	Kim et al. (2012)	10
		Yoo et al. (2013)	7
	S690	Rasmussen and Hancock (1992)	6
	S690	Sun et al. (2019a)	16
	S800	Kim et al. (2014)	3
	S960	Shi et al. (2015)	4
		Li et al. (2019)	4
In-plane bending tests	S550	Green et al. (2002)	10
	S650	Lee et al. (2013)	11
	S690	McDermott (1969)	9
		Beg and Hladinik (1996)	10
		Sun et al. (2019b)	12
Combined loading tests	S690	Sun et al. (2021a)	10
	S800	Kim et al. (2014)	3

2.3.2.2 Codified design rules for local buckling

In place of normal strength steels, the use of high strength steels and ultra-high strength steels leads to more slender sections; these sections are more susceptible to local buckling, which limits their cross-section resistances and deformation capacities. Therefore, local buckling behaviour and relevant design rules need to be well understood.

As there are currently no design standards for ultra-high strength steel structures, the design codes for normal strength and high strength steel (with material grades up to S690 or S700) structural components are described herein. The cross-section classification framework and a bi-linear elastic, perfectly plastic stress–strain curve without the consideration of strain hardening, are employed for the design of normal strength steel and high strength steel (with material yield stresses less than 700 MPa) welded I-sections prone to local buckling in the current international design codes. The welded I-section class is defined on the basis of its most slender constituent plate element without the consideration of interaction between plate elements. For welded I-sections in pure compression, the European code, American specification and Australian standard prescribe the yield loads Af_y (A is gross cross-section area) as non-slender (Class 1, 2 and 3) section compression resistances and effective compression capacities N_{eff} for slender (Class 4) sections. Regarding the bending resistance of a welded I-section, the European code EN 1993-1-12 (CEN, 2007) specifies the plastic moment capacities M_{pl}, the elastic moment capacities M_{el} and the effective moment capacities M_{eff} as the design bending resistances for Class 1 and 2 (plastic) sections, Class 3 (elastic) sections and Class 4 (slender) sections, respectively. American specification (AISC, 2016) and Australian standard (AS, 2016) classify the cross-sections in bending as compact, non-compact and slender sections. For compact welded I-section beams, the design bending moment resistance is prescribed as M_{pl}, while the partial plasticity and the effective bending moment resistance M_{eff} is adopted for non-compact and slender sections. It is worth noting that the effective compression and bending capacities for slender sections are derived on the basis of the effective width approach, which was previously proposed by Winter (1947) and later modified in the considered design codes; this method takes the cross-section as an assemblage of isolated outstand and internal plate elements without the

consideration of element interaction and takes the effectiveness loss into account due to local buckling by means of the reduction of each plate element width.

In terms of welded I-sections under combined compression and bending, the European code EN 1993-1-12 (CEN, 2007) employs nonlinear interaction expression, for Class 1 and 2 sections, derived on the basis of full plasticity over the whole cross-section, while the linear interaction formulation, which is expressed as the linear summation of utilisation ratio for compression and bending stress resultants, with an upper limit of unity, is adopted for Class 3 and Class 4 sections under combined loading. The American specification (AISC, 2016) adopts a bi-linear design interaction expression for welded I-sections under combined loading. For Australian standard (AS, 2016), the same linear design interaction formulation is employed as that of EN 1993-1-12 (CEN, 2007), with the differences lying in the derivations of the cross-section compression and bending moment resistances.

The discussions on the design rules for local buckling of high strength steel structural components under pure compression and combined loading are respectively detailed in Chapter 3 and Chapter 6.

2.3.3 Global instability

2.3.3.1 Existing experimental investigations

Global buckling is generally known as buckling of the whole member, not buckling of the individual plate element; it often occurs because of long member length. The global buckling behaviour and resistances of high strength and ultra-high strength steel welded I-section members under pure compression and combined loading were investigated through a series of previous testing programmes, with Table 2.2

summarising the column tests and beam-column tests on these sections. More detailed, Ban et al. (2012) conducted the experimental and numerical investigations on 7 I-section columns welded from S460 high strength steel flame-cut plates, with the overall buckling behaviour and buckling capacity studied. Based on the test and numerical results, buckling curves in the international codes were assessed and new curves were respectively proposed for major and minor principal axes. The ultimate strengths of 6 welded I-section columns fabricated from flame-cut steel with the nominal yield stress of 460 MPa were also experimentally and numerically studied in Wang et al. (2012b), where the buckling curve in GB 50017 (MOHURD, 2003) was found applicable, while the buckling curve in EN 1993-1-12 (CEN, 2007) was concluded conservative. The member capacities of 6 S460 high strength steel welded I-sections were also investigated by Zhou et al. (2013), who highlighted that the European code (CEN, 2007) provided the best agreement between the test data and the strength predictions. Regarding S690 high strength steel welded I-sections, Rasmussen and Hancock (1995) conducted 5 long column tests and compared their strengths with the strength predictions from the Australian and European standards (AS, 2016; CEN, 2007), with the results revealing that EC 1993-1-12 (CEN, 2007) design buckling curve was conservative. The same conclusion was also found in Shi et al. (2012), where 4 S690 high strength steel welded I-section columns tests were conducted; based on the experimental and numerical results, the design curves in GB 50017 (MOHURD, 2003) and EN 1993-1-12 (CEN, 2007) were highlighted to be conservative and need to be revised. More recently, Li et al. (2016) also conducted 6 S690 high strength steel welded I-section column tests and assessed the American, Chinese and European codified design curves based on the test results; the conclusion was drawn that the adopted curves in EN 1993-1-12 (CEN, 2007) and GB 50017 (MOHURD, 2003) underestimate the ultimate capacities of the examined members, with the revised curves recommended. Ma et al. (2018b) also preformed the

experimental investigation on the structural behaviour and failure loads of 7 S690 high strength steel welded I-section slender columns, based on which, the American Specification (AISC, 2016) was found to provide the most accurate failure load predictions, compared with those derived from European and Chinese codes (CEN, 2007; MOHURD, 2003). Minor-axis flexural buckling and resistances of S690 high strength steel welded I-section columns were also investigated in Sun et al. (2020), in which the design buckling curves in AS 4100 (AS, 2016) and EN 1993-1-12 (CEN, 2007) were assessed based on the experimental and numerical results and concluded to be conservative, while American specification (AISC, 2016) can provide the relatively accurate resistance predictions though some data points were over-predicted. Sun et al. (2021b) also investigated the local–flexural interactive buckling behaviour of S690 high strength steel slender welded I-section columns and highlighted that cross-section dimensions and lengths of members influence the progression and occurrence of local and flexural buckling. Shi et al. (2012) and Ban et al. (2013) conducted S960 ultra-high strength steel welded I-section column tests, with their rather similar conclusions drawn – the design buckling curves in GB 50017 (MOHURD, 2003), EN 1993-1-12 (CEN, 2007) and ANSI/AISC 360-16 (AISC, 2016) were conservative and need to be revised. Until now, there were (i) not enough experimental results on S960 ultra-high strength steel welded I-section columns failing by minor-axis flexural buckling and (ii) no experimental data on S960 ultra-high strength steel slender welded I-section columns failing by local–flexural interactive buckling, and are thus part of the focuses of this thesis.

Eccentric compression tests on S460 and S690 high strength steel welded I-section members were also conducted to investigate their global instability and are reviewed herein. Li et al. (2012) conducted 6 beam-column tests on S460 high strength steel welded I-sections, with the residual stresses in each examined I-section also studied;

the results revealed that (i) the residual stress distribution pattern of S460 high strength steel welded I-sections was almost identical to the counterpart of the ordinary steel and (ii) the design rules in Chinese code were conservative to predict the bearing capacity of these members. Ma et al. (2017) performed the experimental investigation on S690 high strength steel welded I-section members under combined compression and minor-axis bending, with global buckling observed on all the specimens. Based on the experimental results, the design rules in Chinese, European and American codes (MOHURD, 2003; CEN, 2007; AISC, 2016) were assessed, among which, the European code was concluded to be effective and efficient for predicting the buckling resistances. However, the investigations on S960 ultra-high strength steel welded I-section beam-columns are unexplored and hence presented in this thesis.

2.3.3.2 Codified design rules for global instability

To date, there are no international design standards for ultra-high strength steel structures, the codified design rules for high strength steel members failing by flexural buckling are described in this sub-section. The same concept of employing column buckling curves is adopted for the design of high strength steel welded I-section columns susceptible to flexural buckling in the existing European code EN 1993-1-12 (CEN, 2007), American specification (AISC, 2016) and Australian standard (AS, 2016). For high strength steel welded I-section failing by local–flexural interactive buckling, all the aforementioned standards combine the effective width approach for taking local buckling behaviour of slender plate elements into account and column buckling curves for considering flexural buckling. The column buckling curves, as specified in the considered design standards, are detailed in Chapters 4 and 5.

In terms of high strength steel welded I-section members under combined compression and bending, the interaction curves with the end points respectively taken as the member resistances under pure compression and pure bending, and their shapes defined by the interaction factors, are employed in the existing design codes (CEN, 2007; AISC, 2016; AS, 2016). Specifically, two alternative design interaction formulations for high strength steel beam-columns, as prescribed in EN 1993-1-12 (CEN, 2007), directly mirror those specified in EN 1993-1-1 (CEN, 2005); these two formulae are referred to as Methods 1 and 2 (Greiner, 2001), which were further developed by Boissonnade el al. (2006). Four interaction factors (k_{yy}, k_{yz}, k_{zy} and k_{zz}) are adopted for considering all the plasticity effects and second-order geometric effects in the interaction between compression force and bending moment, which were obtained on the basis of numerical simulations of beam-columns with uniform first-order bending moment along the member length. The interaction factors k_{yy} and k_{zz} consider the interaction effects when the bending plane is same as the buckling plane, whilst the interaction factors k_{yz} and k_{zy} allow for the concern that bending plane is perpendicular to the buckling plane. Previous literature indicated that the aforementioned interaction factors are dependent of the member slenderness, cross-section profiles and compression force. Detailed derivations of these factors, as utilised in Methods 1 and 2, are reported in Boissonnade et al. (2002, 2004, 2006), Rusch and Lindner (2004), Lindner (1997, 2003), and Greiner and Lindner (2006). The design interaction expressions for high strength steel components under combined compression and bending are also utilised for beam-column design, as specified in American and Australian standards (AISC, 2016; AS, 2016), but with the adoption of amplification factors to account for the second-order effects. The detailed codified design rules and interaction curves for high strength steel welded I-section beam-columns under combined loading are discussed in Chapter 7.

Table 2.2: Summary of existing column and beam-column tests on high strength steel and ultra-high strength steel welded I-section members.

Tests	Grade	Reference	No. of tests
Column tests	S460	Ban et al. (2012)	7
		Wang et al. (2012b)	6
		Zhou et al. (2013)	6
	S690	Rasmussen and Hancock (1995)	5
		Shi et al. (2012)	4
		Li et al. (2016)	6
		Ma et al. (2018b)	7
		Sun et al. (2020, 2021b)	20
	S960	Shi et al. (2012)	4
		Ban et al. (2013)	6
Beam-column tests	S460	Li et al. (2012)	6
	S690	Ma et al. (2017)	8

2.4 Concluding remarks

This chapter has provided an overview of the existing research work on high strength steel and ultra-high strength steel welded I-section components from cross-section and member levels, and the recent developments in international design codes. It is revealed from the literature review that (i) although comprehensive research on high strength steel welded I-section components with material grades up to S690 has been performed, the structural response and resistances of S960 ultra-high strength steel welded I-section components remain scarce, and (ii) the international design codes only cover the design of the steel structures with material grades up to S690 or S700, prompting the need of efficient design rules for S960 ultra-high strength steel

structures. Therefore, experimental and numerical investigations of S960 ultra-high strength steel welded I-section structural components under different loading cases, assessments of the applicability of the current design rules for S690 (or S700) to S960 counterparts and new design proposals for international design standards, are the focuses of this thesis.

CHAPTER 3

MEMBRANE RESIDUAL STRESSES AND LOCAL BUCKLING OF S960 ULTRA-HIGH STRENGTH STEEL WELDED I-SECTION STUB COLUMNS

3.1 Introduction

This chapter extensively investigates the membrane residual stresses and local buckling behaviour of S960 ultra-high strength steel welded I-section stub columns, underpinned by a comprehensive testing and numerical modelling programme. The testing programme included material testing, membrane residual stress measurements, initial local geometric imperfection measurements and sixteen stub column tests. On the basis of the measured data, a membrane residual stress predictive model was developed. Following the testing programme, a numerical modelling programme was conducted, where finite element models were firstly developed and validated against the test results and then adopted to conduct parametric studies to generate further numerical data. The obtained test and numerical data were used to assess the applicability of the relevant design provisions for S700 (or S690) high strength steel welded I-section stub columns, as given in the European code, American specification and Australian standard, to their S960 ultra-high strength steel counterparts, as discussed later. The assessment results and key findings have also been presented in Su et al. (2021b).

3.2 Testing

3.2.1 General

Eight different I-sections – I-200×150×6, I-150×150×6, I-150×75×6, I-120×120×6, I-90×70×6, I-80×60×6, I-70×70×6 and I-50×50×6 – were adopted in the testing programme; the cross-section designation system begins with a letter 'I' (indicating an I-section), followed by the nominal cross-section size in millimetres (outer section height h × flange width b_f × wall thickness t – see Figure 3.1). All the I-sections were fabricated from 6 mm thick S960 ultra-high strength steel plates through robotic gas metal arc welding (GMAW) by SSAB, Singapore. The nominal material properties and chemical compositions of grade S960 ultra-high strength steel, as specified in EN 10025-6 (CEN, 2019), are reported in Table 3.1. It is worth mentioning that the non-copper coated, low-alloy (0.4% Cr, 2.2% Ni and 0.55% Mo) electrode OK AristoRod 89, with the ultimate stress equal to 1000 MPa, was used for welding S960 ultra-high strength steel plates and the nominal widths of the welds were equal to 6 mm. The robotic welding velocity was equal to 350 mm/min, with the welding current of 180 A and arc voltage of 25 V, which resulted in the heat input equal to 0.77 kJ/mm. Overall, the testing programme included material testing, membrane residual stresses measurements, initial local geometric imperfection measurements and stub column tests.

3.2.2 Material testing

Tensile coupon tests were conducted to determine the material stress–strain curves and key material properties of the examined S960 ultra-high strength steel welded I-sections. Coupons were extracted from the same batch of plates as used for the fabrication of the stub column specimens. Specifically, two longitudinal coupons

were cut along the rolling direction of the plates, while two additional transverse coupons were extracted perpendicularly to the plate rolling direction. The dimensions of the coupons were in compliance with the geometric requirements specified in EN ISO 6892-1 (CEN, 2016). All the coupons were tested in a displacement-controlled Schenck 250 kN tensile testing machine, with the applied displacement rates respectively equal to 0.05 mm/min and 0.8 mm/min up to and beyond the nominal yield stress of 960 MPa. The resulting strain rates satisfied the relevant requirements given in EN ISO 6892-1 (CEN, 2016). Figure 3.2 displays the tensile coupon test setup, including a pair of strain gauges attached to the two parallel wider faces of the coupon at mid-height to record the tensile strains and an extensometer mounted onto the central 50 mm of the necked portion of the coupon to measure the elongations. The measured stress–strain curves for the transverse and longitudinal coupons are displayed in Figure 3.3; it is worth noting that each measured stress–strain curve of S960 ultra-high strength steel exhibits very short if any yield plateau and a rather low level of strain hardening. The key average measured material properties and error for the pair tests are reported in Table 3.2, including the Young's modulus E, the yield stress f_y, the ultimate stress f_u, the strain at the ultimate stress ε_u and the fracture strain ε_f.

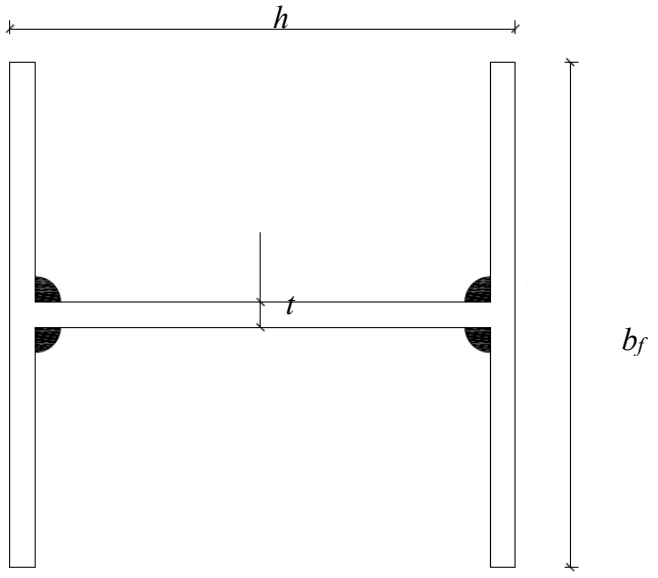

Figure 3.1: Notations of welded I-section.

Table 3.1: Nominal material properties and chemical compositions of grade S960 ultra-high strength steel.

(a) Nominal material properties

Grade	Yield strength (MPa)	Tensile strength (MPa)	Elongation (%)
S960	960	980–1150	12

(b) Chemical compositions.

Grade	C (%)	Si (%)	Mn (%)	P (%)	S (%)	Cr (%)	Cu (%)	Ni (%)	Mo (%)	B (%)
S960	0.20	0.50	1.60	0.02	0.01	0.80	0.30	2.00	0.70	0.005

Figure 3.2: Tensile coupon test setup.

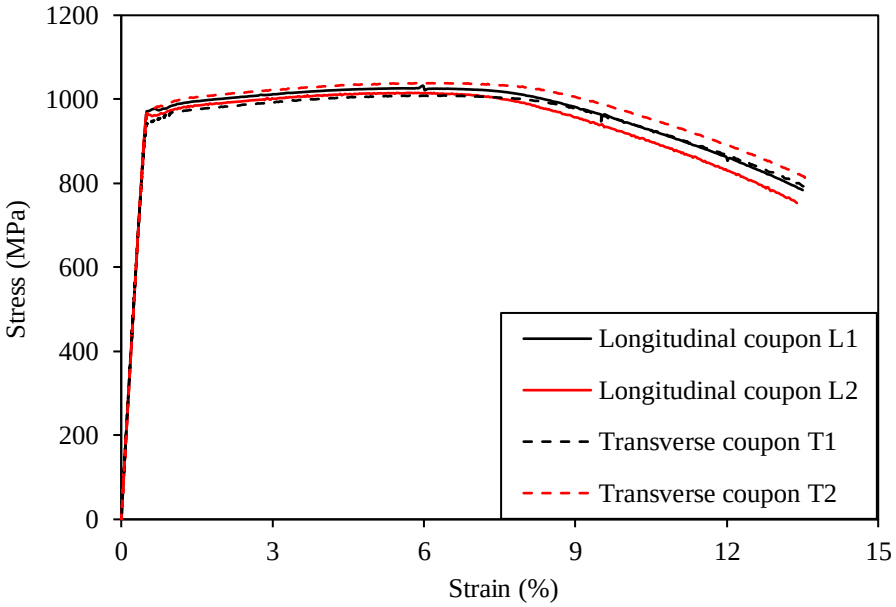

Figure 3.3: Measured stress–strain curves of S960 ultra-high strength steel longitudinal and transverse coupons.

Table 3.2

(a) Summary of key average measured material properties from S960 ultra-high strength steel longitudinal and transverse coupons.

Direction	E (MPa)	f_y (MPa)	f_u (MPa)	ε_u (%)	ε_f (%)
Longitudinal	204393	969	1024	5.8	16.0
Transverse	202289	974	1025	6.0	16.0

(b) Error for the repeat tests.

$\Delta E/E$ (%)	$\Delta f_y/f_y$ (%)	$\Delta f_u/f_u$ (%)	$\Delta \varepsilon_u/\varepsilon_u$ (%)	$\Delta \varepsilon_f/\varepsilon_f$ (%)
1.03	0.52	0.10	3.45	0

3.2.3 Membrane residual stress measurements

Membrane residual stresses inherently exist in high strength steel welded sections and can result in premature failure of structures (Liu & Chung, 2018; Sun et al., 2019a; Le et al., 2020; Li et al., 2020). Measurements of membrane residual stresses in the examined S960 ultra-high strength steel welded I-sections were therefore carried out.

The sectioning method was employed for the membrane residual stress measurements on two representative S960 ultra-high strength steel welded I-sections I-200×150×6 and I-150×150×6, with the procedures conforming to those recommended by Ziemian (2010). The dimensions and locations of the strips within the two representative I-sections before sectioning are displayed in Figures 3.4 and 3.5; the nominal length of each strip was equal to 150 mm, with the nominal width of 10 mm. A pair of gauge holes (2 mm in diameter) were drilled along the centreline of the exterior face of each strip by an automatic dot puncher and the nominal distance from the centroid of each gauge hole to the strip end was equal to 25 mm; this resulted in the nominal strip length between gauge holes L_0 equal to 100 mm, while the actual length r_1 of each strip between gauge holes within the intact welded I-section specimens before sectioning was measured by means of a Demec gauge. The welded I-section specimens were then sectioned into strips through the use of a waterjet cutting machine, which induced little if any heat input into the strips during the sectioning process, without affecting their original membrane stress patterns and amplitudes. Upon sectioning, the length between gauge holes for each strip r_2 was measured again by the Demec gauge. In order to capture the influence of temperature variation on the change in strip lengths, a temperature reference bar, cut from the same batch of material as used for the fabrication of the welded I-section specimens, was adopted. Two gauge holes were also drilled on the temperature reference bar, and its length between gauge holes was firstly measured by the Demec gauge on the same day when length measurements of the strips within the intact welded I-section specimens were conducted and then also recorded on the same day when length measurements of the strips upon sectioning were performed; the values of the first and second measurements were denoted as t_1 and t_2, respectively.

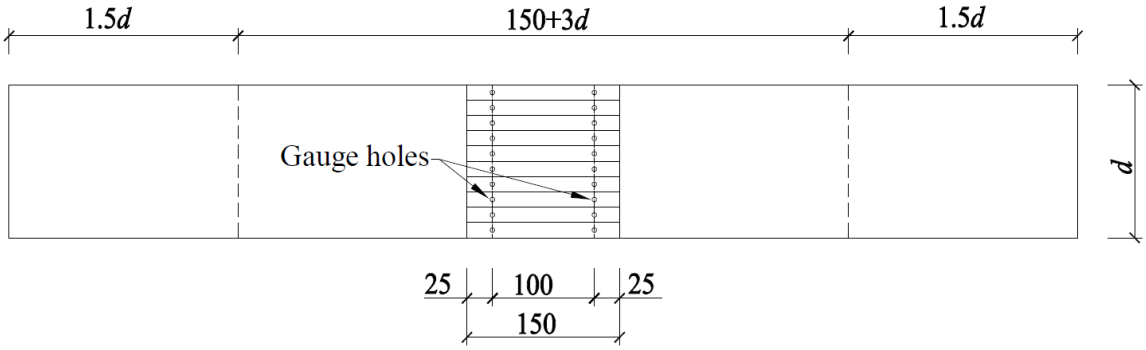

Figure 3.4: Location of strips along specimen length direction (note that d is equal to b_f herein).

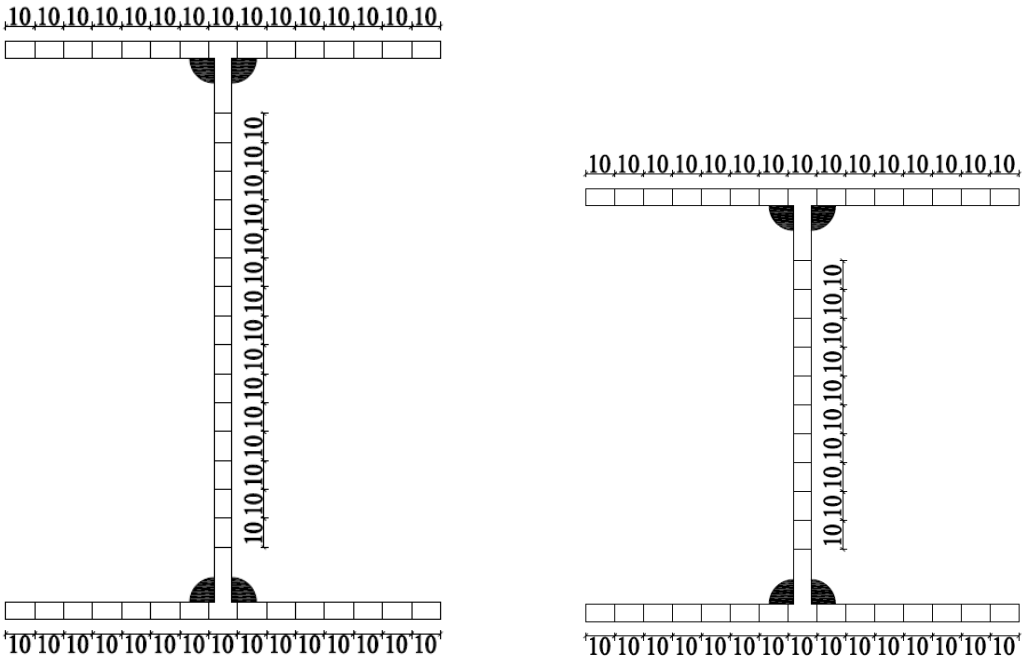

(a) I-200×150×6 (b) I-150×150×6

Figure 3.5: Locations and dimensions of strips within S960 ultra-high strength steel welded I-sections (dimension in mm).

For each strip, the relived membrane residual strain ε_0 was calculated by Equation (3.1), with negative and positive values of ε_0 indicating the release of compressive and tensile membrane residual strains, respectively. It is worth noting that the sectioned strips in the vicinity of welds displayed slightly curved shapes; this can be attributed to the existence of a relatively high level of through-thickness bending residual stresses near the welds, and corrections to the relieved membrane residual strains calculated from Equation (3.1) were then made according to Equation (3.2) (Tebedge et al., 1973), where δ is the deviation measured from the mid-point of the strip to a straight reference line connecting the centroids of gauge holes and $\varepsilon_{0,c}$ is the corrected relieved membrane residual strain. Finally, the membrane residual stresses can be computed by multiplying the corresponding membrane residual strains by the Young's modulus.

$$\varepsilon_0 = \frac{(r_1 - t_1) - (r_2 - t_2)}{L_0 + (r_1 - t_1)} \tag{3.1}$$

$$\varepsilon_{0,c} = \varepsilon_0 + \frac{(\delta / L_0)^2}{6(\delta / L_0)^4 + 1} \tag{3.2}$$

Figures 3.6(a) and 3.6(b) depict the distribution patterns and amplitudes of the measured membrane residual stresses for the two S960 ultra-high strength steel welded I-sections I-200×150×6 and I-150×150×6, while the peak membrane residual stress amplitudes, normalised by the material yield stress, are given in Table 3.3, where f_t is the peak tensile membrane residual stress amplitude and f_c is the peak compressive membrane residual stress amplitude. The measured membrane residual stresses of the flanges and webs are also displayed in a normalised format – see Figures 3.7(a) and 3.7(b), where the membrane residual stresses, normalised by the material yield stress, are plotted against the normalised positions; the origin point (0.0) stands for the flange-to-web junctions, while the end point (1.0) represents the flange tips or web mid-points.

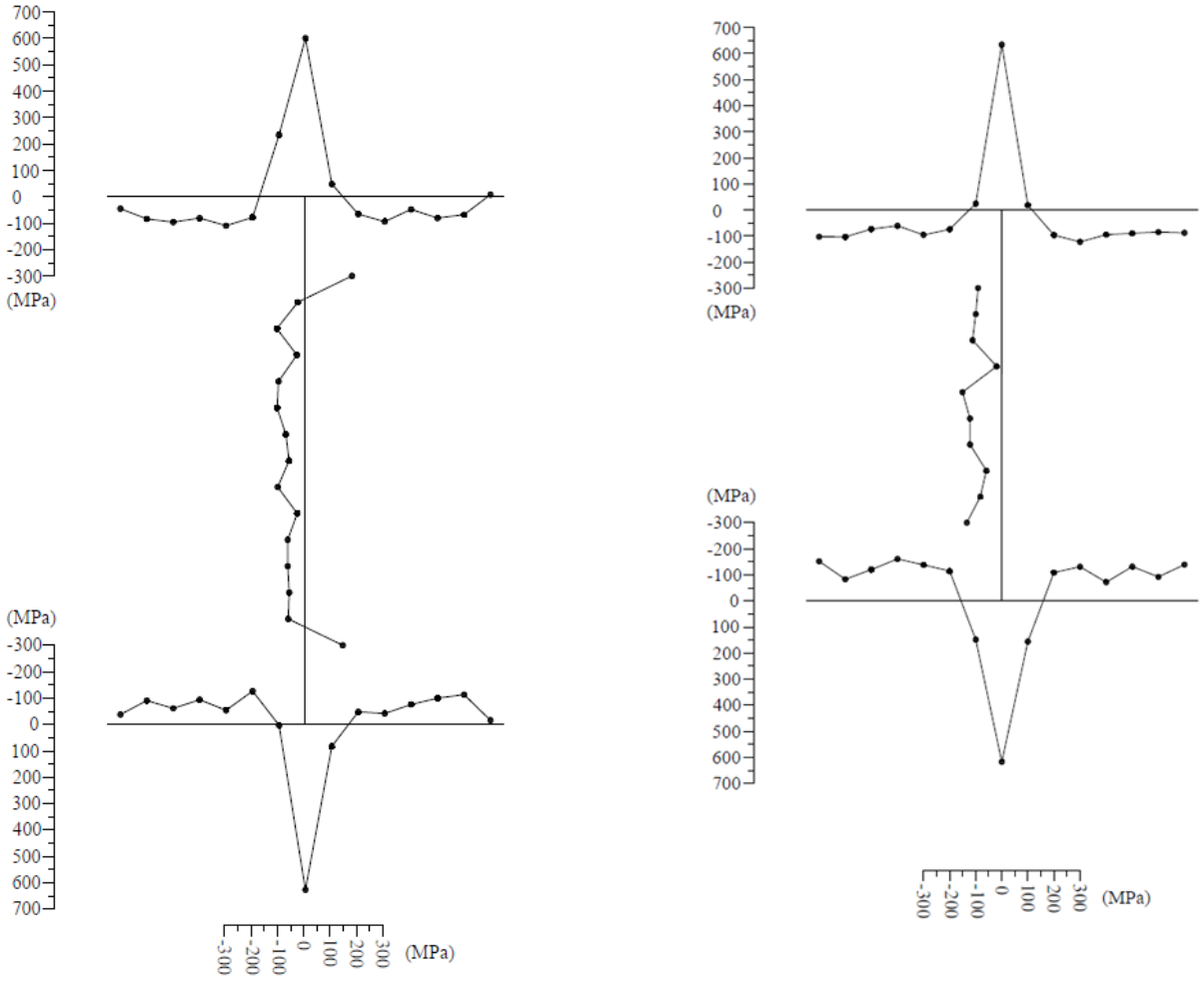

(a) I-200×150×6 (b) I-150×150×6

Figure 3.6: Measured membrane residual stress patterns and amplitudes for S960 ultra-high strength steel welded I-sections I-200×150×6 and I-150×150×6.

Table 3.3: Normalised measured peak tensile and compressive membrane residual stresses of S960 ultra-high strength steel welded I-sections.

Specimen ID	Peak tensile residual stresses (f_t/f_y)		Peak compressive residual stresses (f_c/f_y)	
	Flange	Web	Flange	Web
I-200×150×6	0.62	0.18	-0.11	-0.11
	0.64		-0.13	
I-150×150×6	0.65	–	-0.13	-0.15
	0.63		-0.17	
Mean	0.64	0.18	-0.14	-0.13
Maximum	0.65	0.18	-0.17	-0.15

Given that there have been no codified models for predicting membrane residual stresses in S960 ultra-high strength steel welded I-sections, the two existing membrane residual stress predictive models for normal strength steel welded I-sections, as specified in ECCS (1976) and BSK 99 (2003), were evaluated for their applicability to S960 ultra-high strength steel welded I-sections. The two existing codified membrane residual stress predictive modes for normal strength steel welded I-sections were established based on the same three-stage distribution pattern, as shown in Figure 3.8, though different distribution parameters (a, b, c and d) and peak membrane residual stress magnitudes were adopted, as reported in Table 3.4. Comparisons of the ECCS and BSK 99 predictive models with the measured membrane residual stress data points in Figures 3.7(a) and 3.7(b) revealed that (i) both the predictive modes in ECCS (1976) and BSK 99 (2003) unduly over-predict the peak tensile membrane residual stresses and (ii) the BSK 99 (2003) predictive mode also underestimates the peak compressive membrane residual stresses, especially in flanges. The two stage-predictive model with no transition regions, as proposed by Li et al. (2020), is also compared with the measured membrane residual stress data points in Figures 3.7(a) and 3.7(b) and shown to result in a higher level of accuracy over the two codified predictive models, however, the membrane residual

stress transition regions are not well captured. Finally, a new predictive model was developed, through the use of the same three-stage distribution pattern (see Figure 3.8) but a different set of distribution parameters and peak membrane residual stress magnitudes, as reported in Table 3.4. Comparisons of the measured membrane residual stresses in S960 ultra-high strength steel welded I-sections with the new proposed predictive model are displayed in Figures 3.7(a) and 3.7(b), indicating a better level of agreement.

Table 3.4: Membrane residual stress predictive models.

Preditive models	Peak tensile residual stresses	Peak compressive residual stresses	a	b	c	d
ECCS (1976)	f_y	$0.25f_y$	$0.05b_f$	$0.15b_f$	$0.075h_w$	$0.05h_w$
BSK 99 (2003)	f_y	From equilibrium	$0.75t_f$	$1.5t_f$	$1.5t_w$	$1.5t_w$
Li et al. (2020)	$(0.3\ln t+0.3)f_y$	From equilibrium	0	$20\ln t+2$	$8\ln t+2$	0
Proposed model	$0.8f_y$	From equilibrium	$0.075b_f$	$0.15b_f$	$0.075h_w$	$0.075h_w$

Note: b_f is the flange width and h_w is the clear distance between flanges; t_f is the flange thickness and t_w is the web thickness.

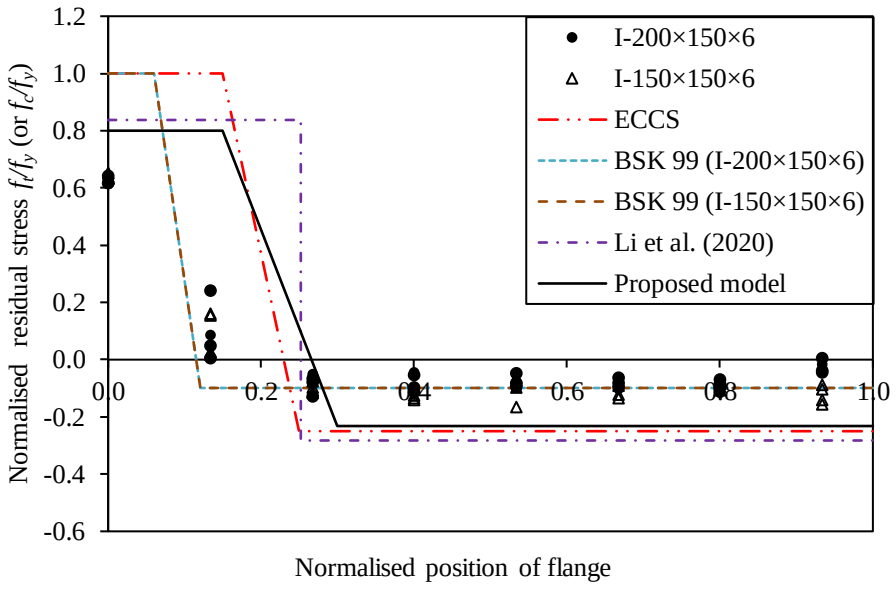

(a) flange

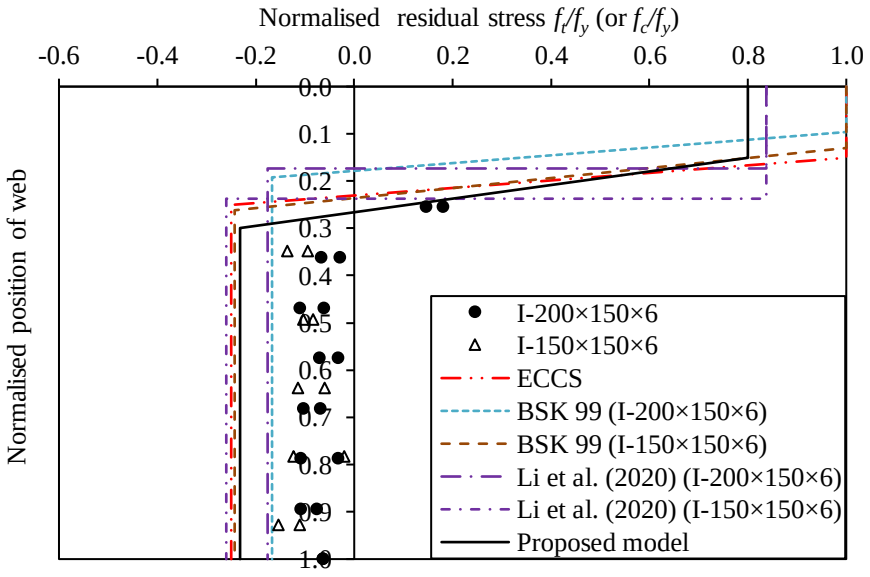

(b) web

Figure 3.7: Comparisons of measured membrane residual stresses in S960 ultra-high strength steel welded I-sections with predictive models.

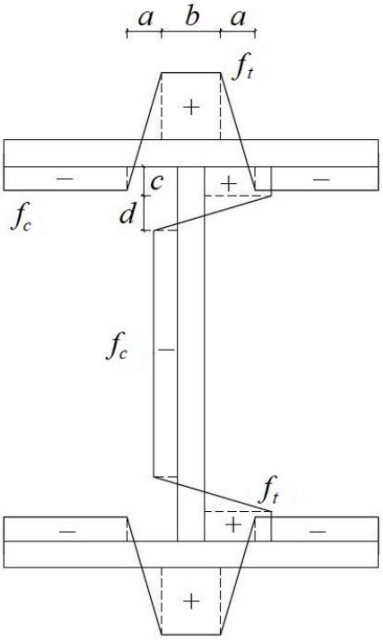

Figure 3.8: Membrane residual stress distribution pattern for welded I-sections.

3.2.4 Initial geometric imperfection measurements

The local buckling of thin-walled steel stub columns is known to be influenced by their initial local geometric imperfections, measurements of which are thus conducted for each S960 ultra-high strength steel welded I-section stub column specimen. The test setup for initial local geometric imperfection measurements is similar to that used by Schafer and Peköz (1998) and shown in Figure 3.9, where three LVDTs, mounted onto the head of a milling machine, are moving transversely along two flanges and one web at several cross-sections of the stub column specimen. For each plate element, the initial local geometric imperfections were defined as the deviations from a linear regression line fitted to the measured data set, while the largest measured deviation from all the three plate elements was defined as the initial local geometric imperfection magnitude of the stub column specimen ω_0, as reported in Table 3.5.

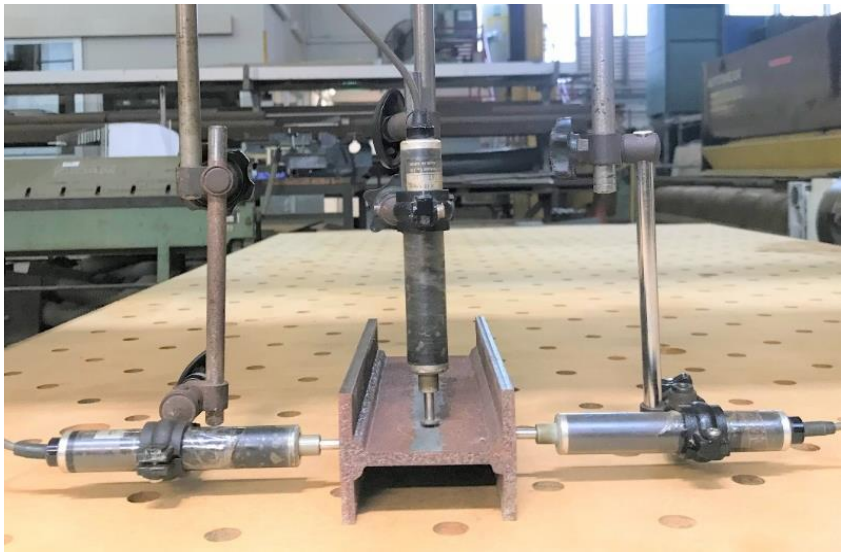

Figure 3.9: Test setup for initial local geometric imperfection measurements.

Table 3.5: Measured geometric dimensions and initial local geometric imperfection magnitudes of S960 ultra-high strength steel welded I-section stub columns.

Specimen ID	L (mm)	h (mm)	b_f (mm)	t (mm)	ω_0 (mm)
I-200×150×6-1	599.2	199.73	149.71	6.01	0.10
I-200×150×6-2	600.3	200.06	150.03	5.96	0.11
I-150×150×6-1	448.6	149.34	149.23	5.98	0.11
I-150×150×6-2	450.0	149.54	150.01	6.07	0.13
I-150×75×6-1	321.4	149.76	75.93	6.14	0.09
I-150×75×6-2	319.8	149.11	75.98	6.10	0.07
I-120×120×6-1	358.9	119.13	119.30	5.99	0.06
I-120×120×6-2	360.5	118.94	119.64	6.03	0.12
I-90×70×6-1	238.5	89.69	69.20	5.97	0.07
I-90×70×6-2	240.0	90.56	69.47	6.01	0.05
I-80×60×6-1	209.0	78.95	59.24	6.03	0.09
I-80×60×6-2	210.0	79.04	59.30	5.96	0.04
I-70×70×6-1	208.5	69.84	69.30	6.01	0.10
I-70×70×6-2	210.5	69.97	69.34	5.94	0.07
I-50×50×6-1	148.0	49.81	49.15	5.98	0.05
I-50×50×6-2	148.5	49.09	49.23	6.06	0.03

3.2.5 Stub column tests

For each of the eight S960 ultra-high strength steel welded I-sections, two repeated stub column tests were carried out, to investigate their local buckling behaviour and compression resistances. Table 3.5 reports the measured cross-section dimensions and member length L for all the stub column specimens; note that the two repeated stub column specimens for each welded I-section were differentiated by using a number '1' or '2' in the specimen ID. Prior to stub column tests, milling and deburring were carried out on the specimen ends; this enabled the achievement of flat and parallel end surfaces of the specimens and thus uniformly distributed compressive stresses over the whole end sections during testing. A displacement-controlled INSTRON 5000 kN hydraulic testing machine was used for all the stub column tests, with a constant rate of 0.3 mm/min, and equipped with parallel fixed platens, to provide fixed-ended boundary conditions to the specimen ends. The stub column test setup is displayed in Figure 3.10, including a pair of longitudinally-placed LVDTs to measure the specimen end shortenings and two strain gauges, attached to the web-to-flange junctions of the specimen at mid-height, to record the axial strains. It is worth noting that the measured end shortening values from the LVDTs included the deformations of both the stub column specimen and the platens of the testing machine(Centre for Advanced Structural Engineering, 1990; Gardner & Nethercot, 2004a); the end shortening values were thus corrected, based on the strain gauge readings, to eliminate the deformations of the platens. Figure 3.11 displays the corrected load–end shortening curves for the S960 ultra-high strength steel welded I-section stub column specimens, while the key experimental results upon testing, including the failure load N_u, the end shortening at the failure load δ_u and the ratio of the failure load to the cross-section yield load N_u/Af_y (A is the gross cross-section area), are reported in Table 3.6. Local buckling was identified for all the sixteen S960 ultra-high strength steel welded I-section stub column specimens upon testing, with

typical failed specimens I-150×150×6-1 and I-90×70×6-1 displayed in Figure 3.12.

Figure 3.10: Stub column test setup.

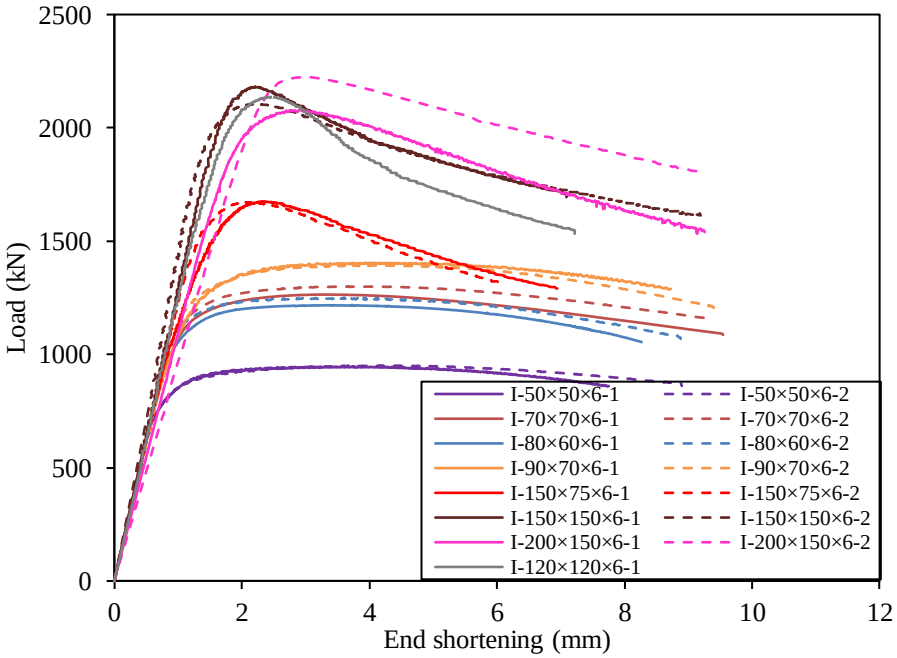

Figure 3.11: Load–end shortening curves of S960 ultra-high strength steel welded I-section stub columns.

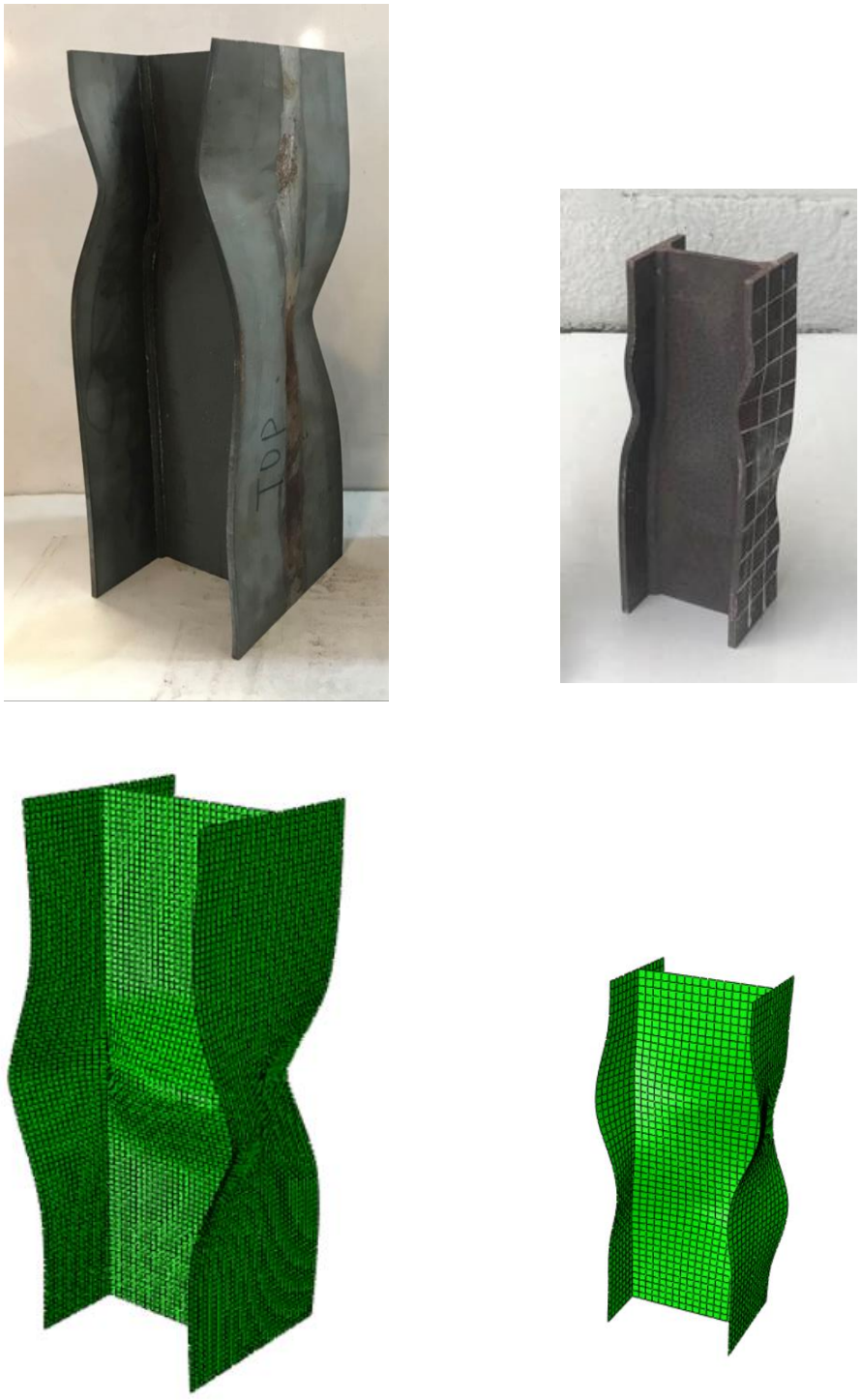

Figure 3.12: Local buckling failure modes of typical S960 welded I-section stub column specimens (from left to right: I-150×150×6-1 and I-90×70×6-1).

Table 3.6: Summary of key stub column test results.

Specimen ID	N_u (kN)	δ_u (mm)	N_u/Af_y
I-200×150×6-1	2223.14	2.99	0.78
I-200×150×6-2	2080.20	2.92	0.74
I-150×150×6-1	2104.29	2.24	0.83
I-150×150×6-2	2180.35	2.21	0.85
I-150×75×6-1	1621.09	2.06	1.24
I-150×75×6-2	1671.03	2.27	1.25
I-120×120×6-1	2135.85	2.47	1.06
I-120×120×6-2 [a]	1930.33	–	0.95
I-90×70×6-1	1393.82	3.95	1.11
I-90×70×6-2	1405.18	3.94	1.11
I-80×60×6-1	1250.50	3.60	1.15
I-80×60×6-2	1217.18	3.72	1.13
I-70×70×6-1	1300.34	3.68	1.14
I-70×70×6-2	1263.98	3.33	1.12
I-50×50×6-1	950.92	4.17	1.21
I-50×50×6-2	946.92	3.74	1.19

[a] LVDTs dropped down during testing and no end-shortening data was obtained.

3.3 Numerical modelling

3.3.1 General

Following the testing programme, a numerical modelling programme was conducted by using the finite element (FE) modelling software ABAQUS (2014) and fully presented in this section. The detailed modelling assumptions, techniques and procedures were firstly described. Then, the developed FE models were validated against the test results. Finally, parametric studies were performed by using the validated FE models to generate further numerical data over a wide range of cross-section dimensions.

3.3.2 Development of FE models

Each S960 ultra-high strength steel welded I-section stub column specimen was modelled according to the corresponding measured dimensions – see Table 3.5. The shell element 'S4R', as provided in the element library of ABAQUS (2014), has been proven to be capable of accurately simulating S690 high strength steel and S960 ultra-high strength steel welded I-section members (Ma et al., 2018a; Sun et al., 2019a; Li et al., 2020) and was also adopted throughout the present numerical modelling. On the basis of a mesh sensitivity study examining element sizes varied between 0.5t to 3t, the size of the S4R element was selected as t, which was found to be able to provide accurate numerical simulation results with satisfactory computational efficiency and also allowed for accurate inclusion of membrane residual stresses into the modelled S960 ultra-high strength steel welded I-section stub columns. In terms of the material modelling of S960 ultra-high strength steel, the true stress–plastic strain curves, converted from the measured (engineering) stress–strain curves for the longitudinal coupons – see Figure 3.3, were assigned to the S960 ultra-high strength steel welded I-section stub column FE models. The membrane residual stresses, as determined from the predictive model proposed in Section 3.2.3, were included into each S960 ultra-high strength steel welded I-section stub column FE model by means of the 'Predefined Field' command (ABAQUS, 2014); Figure 3.13 illustrates the membrane residual stresses incorporated into the FE model for typical S960 ultra-high strength steel welded I-section stub column specimens I-150×150×6-1. With regard to the modelling of the fixed-ended boundary conditions employed in the tests, the two end sections of each stub column FE model were coupled to two concentric reference points and fully restrained against all degrees of freedom, except for displacement along the longitudinal direction at one end. For the inclusion of initial local geometric imperfection into each stub column FE model, an elastic eigenvalue analysis (ABAQUS, 2014) was firstly performed to derive the lowest elastic local

buckling mode shape, which was taken as the initial local geometric imperfection distribution pattern along the model length and then factored by appropriate imperfection magnitudes. A total of four imperfection magnitudes, including the measured value ω_0 and 1/100, 1/30 and 1/10 of the wall thickness, were adopted, to evaluate their influences on the numerical failure loads and seeking the most appropriate imperfection magnitude to be used in the parametric studies. Finally, a static Riks analysis (ABAQUS, 2014), accounting for material and geometric nonlinearity, was conducted on each S960 ultra-high strength steel welded I-section stub column FE model to derive the numerical failure load, load–end shortening curve and failure mode.

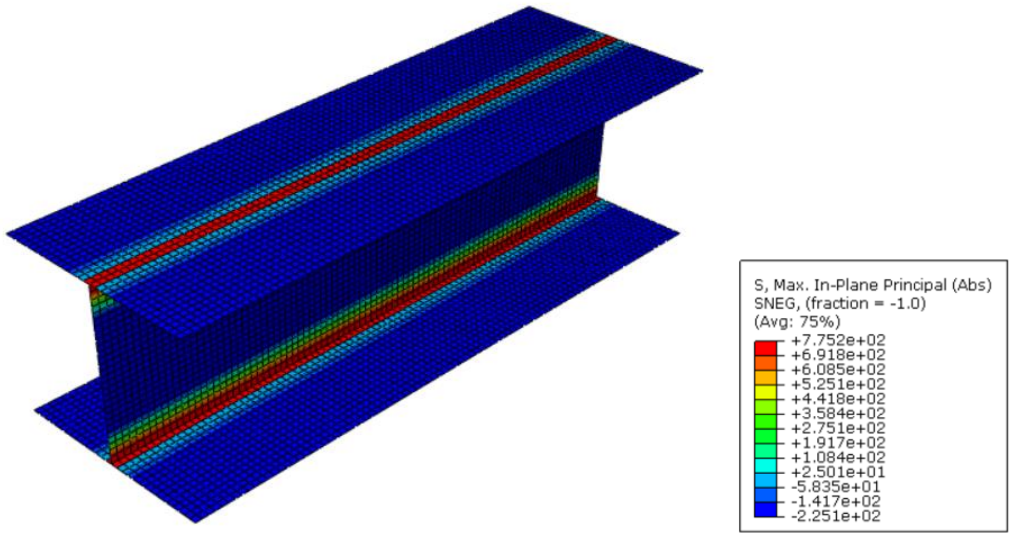

Figure 3.13: Typical membrane residual stress pattern and amplitudes (in MPa) in modelled S960 ultra-high strength steel welded I-section stub column I-150×150×6-1.

3.3.3 Validation of FE models

Validation of the developed S960 ultra-high strength steel welded I-section stub column FE models was conducted by comparing the obtained numerical results with the experimental observations. The numerical to test failure load ratios for all the S960 ultra-high strength steel welded I-section stub column specimens are reported

in Table 3.7, with the results revealing that (i) all the four considered imperfection magnitudes lead to relatively accurate and consistent predictions of the test failure loads and (ii) the best agreement between the test and numerical failure loads was achieved when the measured magnitude or $t/100$ was adopted. The test and numerical load–end shortening curves for typical S960 ultra-high strength steel welded I-section stub column specimens I-150×150×6-1 and I-90×70×6-1 are displayed in Figure 3.14, where the test load–deformation histories are well captured by their numerical counterparts. Excellent agreement between the test and numerical failure modes was also observed, as illustrated in Figure 3.12. Overall, the developed FE models are capable of simulating the test responses of the S960 ultra-high strength steel welded I-section stub column specimens and therefore deemed to be validated. It is also worth mentioning that although the simple combination of the material properties of the tensile coupons (cut from the virgin plates without any heat input) and the membrane residual stresses lead to good numerical modelling results, more accurate consideration of the material properties within the heat affected zones may involve the use of the post-fire material properties within these zones (Qiang, et al., 2013; Li et al., 2017; Li and Young, 2018; Liu and Chung, 2018; Chen et al., 2019; Su et al., 2020).

Table 3.7: Comparisons of FE failure loads with test failure loads for varying initial local geometric imperfection magnitudes.

Specimen ID	FE N_u/Test N_u			
	ω_0	t/10	t/30	t/100
I-200×150×6-1	0.99	0.98	0.99	1.01
I-200×150×6-2	0.98	0.97	0.97	0.99
I-150×150×6-1	0.97	0.96	0.97	0.98
I-150×150×6-2	1.00	0.99	0.99	1.01
I-150×75×6-1	0.85	0.85	0.85	0.86
I-150×75×6-2	0.88	0.87	0.88	0.89
I-120×120×6-1	0.96	0.93	0.95	0.96
I-120×120×6-2	0.95	0.92	0.94	0.95
I-90×70×6-1	0.97	0.97	0.97	0.98
I-90×70×6-2	0.98	0.96	0.97	0.98
I-80×60×6-1	0.98	0.96	0.97	0.99
I-80×60×6-2	0.94	0.91	0.93	0.94
I-70×70×6-1	0.91	0.90	0.91	0.92
I-70×70×6-2	0.88	0.85	0.86	0.88
I-50×50×6-1	0.87	0.86	0.86	0.87
I-50×50×6-2	0.90	0.87	0.88	0.90
Mean	0.94	0.92	0.93	0.94
COV	0.05	0.05	0.05	0.05

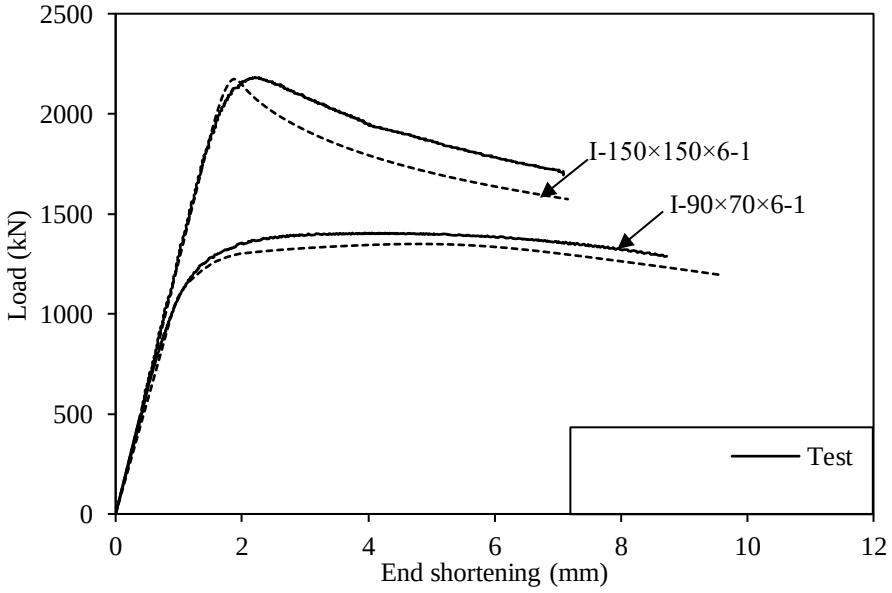

Figure 3.14: Experimental and numerical load–end shortening curves for typical S960 ultra-high strength steel welded I-section stub column specimens I-150×150×6-1 and I-90×70×6-1.

3.3.4 Parametric studies

Parametric studies were conducted by using the validated FE models, to obtain a numerical data pool on S960 ultra-high strength steel welded I-section stub columns over a wide range of cross-section dimensions. In the present parametric studies, the modelling assumptions, techniques and procedures were the same as those reported in Section 3.3.2, but the magnitudes of the local imperfections were set equal to $t/100$. With regard to the geometric dimensions of the modelled I-sections, the outer section heights were fixed at 150mm, while the flange widths were selected as 150 mm, 90 mm and 75 mm, respectively, resulting in the cross-section aspect ratios from 1.0 to 2.0 being considered; the flange and web thicknesses were set to be equal and varied from 3 mm to 20 mm. The member length of each modelled stub column was set equal to three times its mean cross-section dimension (Ziemian, 2010), to prevent global buckling. Overall, 84 numerical data on S960 ultra-high strength steel welded I-section stub columns have been generated through the present parametric studies.

3.4 Evaluation of existing design codes

3.4.1 General

The existing EN 1993-1-12 (CEN, 2007), ANSI/AISC 360-16 (AISC, 2016) and AS 4100 (AS, 2016) only cover the design of steel structures with the nominal material yield stresses less than or equal to 700 MPa (or 690 MPa) and thus none of the existing design codes can be directly used for the studied S960 ultra-high strength steel welded I-section stub columns. In this section, the applicability of the relevant codified local buckling design provisions, including the slenderness limits for cross-section classification and the effective width methods, were assessed for S960 ultra-high strength steel welded I-section stub columns, based on the obtained test and

numerical data.

3.4.2 Slenderness limits for cross-section classification

With regard to the design of steel sections under compression, the concept of cross-section classification was adopted in all the three aforementioned design codes. Two types of cross-section, namely non-slender and slender cross-sections, are defined in ANSI/AISC 360-16 (AISC, 2016) and AS 4100 (AS, 2016), while four classes (i.e. Class 1, 2, 3 and 4) of cross-section are defined in EN 1993-1-12 (CEN, 2007). For non-slender cross-sections (corresponding to Class 1–3 cross-sections defined in EN 1993-1-12 (CEN, 2007)), the compression resistance is given as the yield load Af_y, whereas for slender cross-sections (corresponding to Class 4 cross-sections defined in EN 1993-1-12 (CEN, 2007)), the occurrence of local buckling prevents the achievement of the yield load at failure and the compression resistance is now given as the effective compression resistance $A_{eff}f_y$. The class of a cross-section is defined according to the class of its most slender constituent plate element, while each plate element is classified by comparing the flat width-to-thickness ratio c/t with the corresponding slenderness limit; c is denoted as c_f for outstand plate elements but c_w for internal plate elements. It is worth noting that the slenderness limits between non-slender and slender plate elements are also named as the Class 3 limits in EN 1993-1-12 (CEN, 2007), the limiting width-to-thickness ratios in ANSI/AISC 360-16 (AISC, 2016) and the yield slenderness limits in AS 4100 (AS, 2016). Table 3.8 reports the slenderness limits between non-slender and slender internal plate elements (i.e. webs of I-sections) and outstand plate elements (i.e. flanges of I-sections) in compression, as set out in the aforementioned three design codes, where $\varepsilon_{EC3} = \sqrt{235 / f_y}$, $\varepsilon_{AISC} = \sqrt{E / f_y}$ and $\varepsilon_{AS} = \sqrt{250 / f_y}$ are used in EN 1993-1-12 (CEN, 2007), ANSI/AISC 360-16 (AISC, 2016) and AS 4100 (AS, 2016), respectively, to consider the influence of the material yield stress on the slenderness

limit, and $k_c = 4\sqrt{t/c}$ is adopted in ANSI/AISC 360-16 (AISC, 2016) to take into account the effect of internal plate element dimensions on the slenderness limits for outstand plate elements.

Graphical assessments of the applicability of the existing codified slenderness limits to S960 ultra-high strength steel outstand plate elements are shown in Figures 3.15–3.17, where the test and numerical failure loads of S960 ultra-high strength steel welded I-section stub columns, normalised by the yield loads, N_u/Af_y are plotted against the ratios of $c_f/(t\varepsilon_{EC3})$, $c_f/(tk_c^{0.5}\varepsilon_{AISC})$ and $c_f/t\varepsilon_{AS}$, together with the corresponding codified slenderness limits. The graphical assessment results revealed that all the three codified slenderness limits for slender/non-slender outstand plate elements in compression are accurate when used for flanges of S960 ultra-high strength steel welded I-section stub columns. Similarly, the codified slenderness limits between non-slender and slender internal plate elements in compression were also assessed for their applicability to webs of S960 ultra-high strength steel welded I-section stub columns, with the graphical assessment results depicted in Figures 3.18–3.20, indicating good applicability. Overall, it can be concluded that the existing slenderness limits for slender/non-slender outstand and internal plate elements in compression, as set out in EN 1993-1-12 (CEN, 2007), ANSI/AISC 360-16 (AISC, 2016) and AS 4100 (AS, 2016), can be accurately used for classifying flanges and webs of S960 ultra-high strength steel welded I-section stub columns.

Table 3.8: Summary of EC3, AISC and AS slenderness limits between slender and non-slender plate elements in compression.

Design codes	Outstand elements	Internal elements
EN 1993-1-12	$14\varepsilon_{EC3}$	$42\varepsilon_{EC3}$
AISC 360	$0.64k_c^{0.5}\varepsilon_{AISC}$	$1.49\varepsilon_{AISC}$
AS 4100	$14\varepsilon_{AS}$	$35\varepsilon_{AS}$

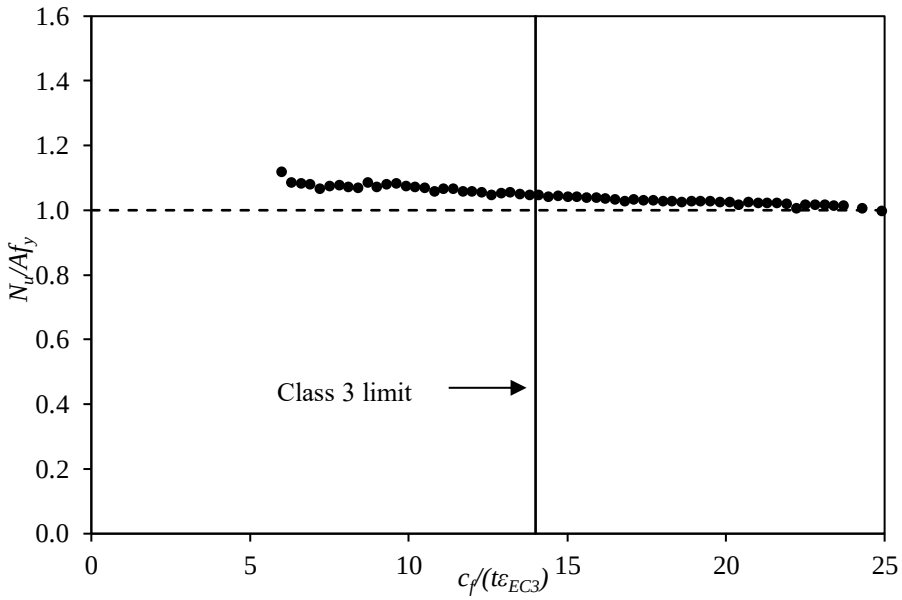

Figure 3.15: EC3 Class 3 limit for outstand plate elements in compression.

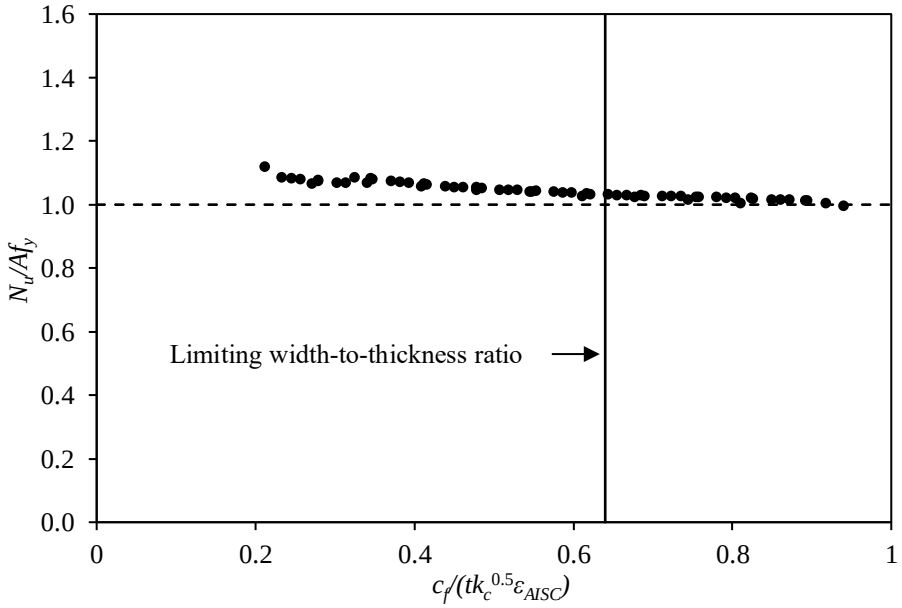

Figure 3.16: AISC limiting width-to-thickness ratio for outstand plate elements in compression.

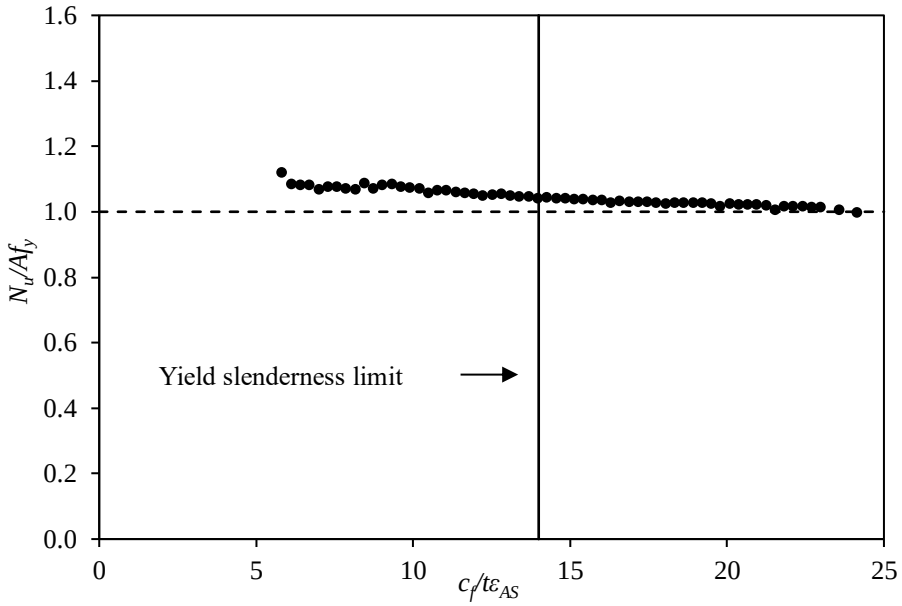

Figure 3.17: AS yield slenderness limit for outstand plate elements in compression.

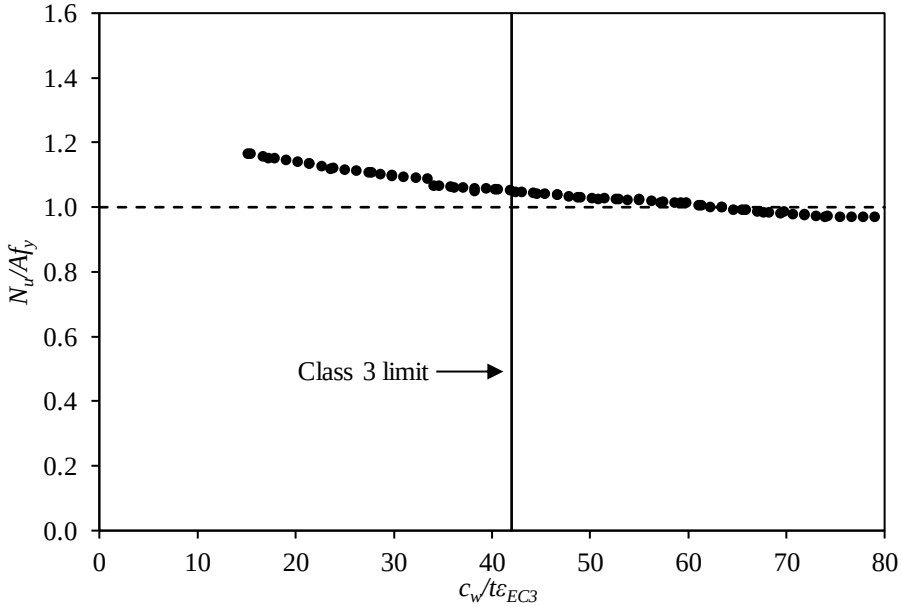

Figure 3.18: EC3 Class 3 limit for internal plate elements in compression.

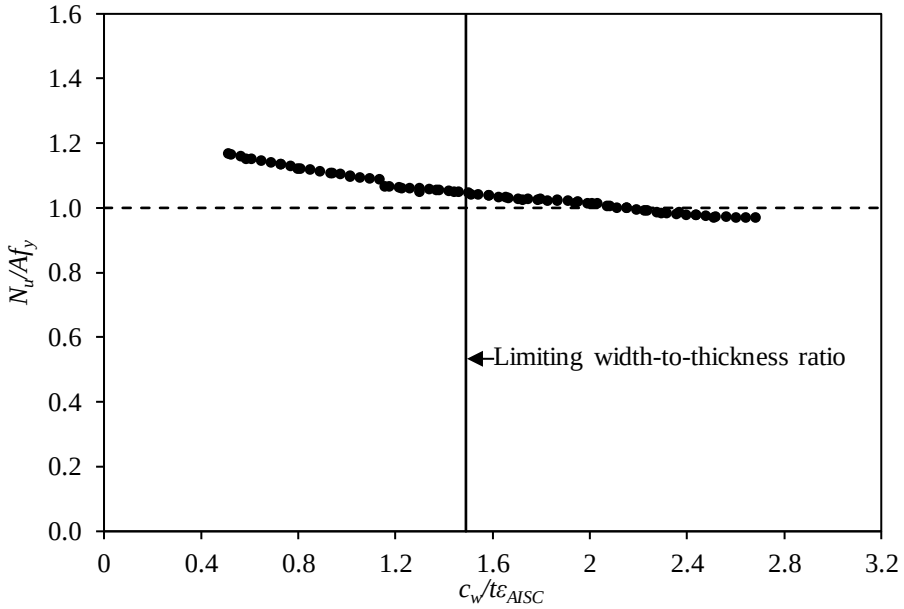

Figure 3.19: AISC limiting width-to-thickness ratio for internal plate elements in compression.

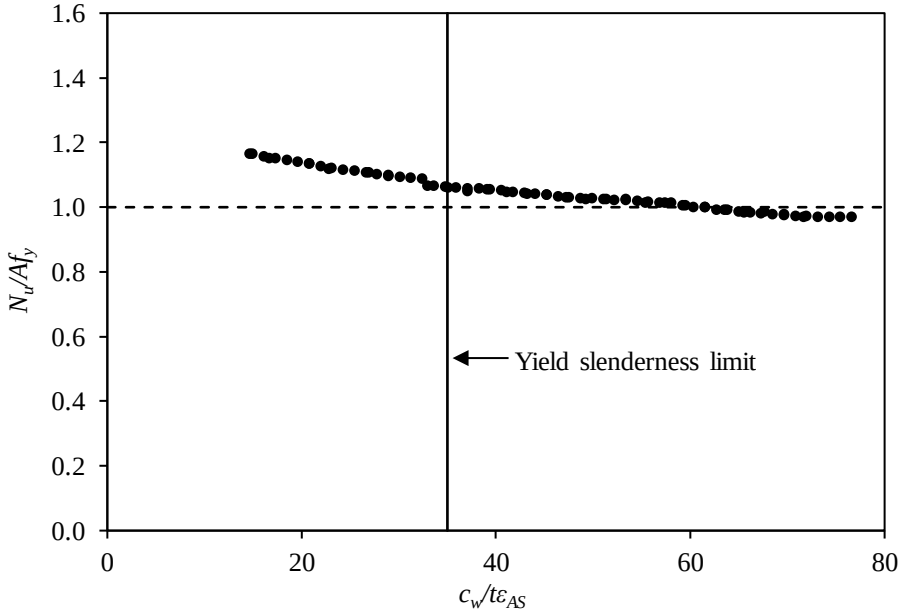

Figure 3.20: AS yield slenderness limit for internal plate elements in compression.

3.4.3 Cross-section compression resistances

In this section, the design provisions for calculating cross-section compression

resistances, as set out in the three considered design codes, were evaluated for their applicability to S960 ultra-high strength steel welded I-section stub columns. All the three considered design codes prescribe that the compression resistance is given as the yield load Af_y for non-slender cross-sections but the effective compression resistance $A_{eff}f_y$ for slender cross-sections. The effective cross-section area of a slender cross-section A_{eff} is equal to the summation of the gross areas of the non-slender constituent plate elements and the effective areas of the slender constituent plate elements, while the effective area of each slender constituent plate element is calculated as the wall thickness t multiplying by the effective plate element width c_{eff} (to account for local buckling). Note that EN 1993-1-12 (CEN, 2007), ANSI/AISC 360-16 (AISC, 2016) and AS 4100 (AS, 2016) employ different expressions for determining the effective plate element width, as shown by Equations (3.3)–(3.5), respectively, where $\bar{\lambda}_l$ is the plate element slenderness and calculated by Equation (3.6) (CEN, 2005), where k_σ is the buckling factor and equal to 0.43 and 4.0 for outstand and internal plate elements in compression, respectively, and $\bar{\lambda}_{r,out}$ and $\bar{\lambda}_{r,int}$ respectively denote the AISC limiting width-to-thickness ratios for outstand and internal plate elements – see Table 3.8.

$$c_{eff,EC3}=\begin{cases} c\left(\dfrac{1}{\bar{\lambda}_l}-\dfrac{0.188}{\bar{\lambda}_l^{\,2}}\right)\le c & \text{for outstand plate elements} \\ c\left(\dfrac{1}{\bar{\lambda}_l}-\dfrac{0.22}{\bar{\lambda}_l^{\,2}}\right)\le c & \text{for internal plate elements} \end{cases} \tag{3.3}$$

$$c_{eff,AISC}=\begin{cases} c\left(\dfrac{1.49\bar{\lambda}_{r,out}}{c/t}-\dfrac{0.49\bar{\lambda}_{r,out}^{2}}{(c/t)^2}\right)\le c & \text{for outstand plate elements} \\ c\left(\dfrac{1.31\bar{\lambda}_{r,\mathrm{int}}}{c/t}-\dfrac{0.31\bar{\lambda}_{r,\mathrm{int}}^{2}}{(c/t)^2}\right)\le c & \text{for internal plate elements} \end{cases} \tag{3.4}$$

$$c_{eff,AS}=\begin{cases} c\left(\dfrac{14}{c/(t\varepsilon_{AS})}\right)\le c & \text{for outstand plate elements} \\ c\left(\dfrac{35}{c/(t\varepsilon_{AS})}\right)\le c & \text{for internal plate elements} \end{cases} \tag{3.5}$$

$$\bar{\lambda}_l = \frac{c/t}{28.4\varepsilon_{EC3}\sqrt{k_\sigma}} \tag{3.6}$$

Figures 3.21–3.23 display the test and numerical failure loads of S960 ultra-high strength steel welded I-section stub columns N_u compared with the predicted cross-section compression resistances $N_{u,pred}$ by the three design codes, while Table 3.9 reports the mean test and numerical to predicted failure load ratios $N_u/N_{u,pred}$ and the corresponding coefficients of variation (COVs), categorised by cross-section type. The graphical and quantitative comparison results generally revealed that the three sets of codified design provisions yield accurate and consistent cross-section compression resistance predictions for S960 ultra-high strength steel welded I-section stub columns with both non-slender and slender cross-sections. The difference between the codified compression resistance predictions for S960 ultra-high strength steel slender welded I-section stub columns is attributed to the use of different slenderness limits and effective width expressions.

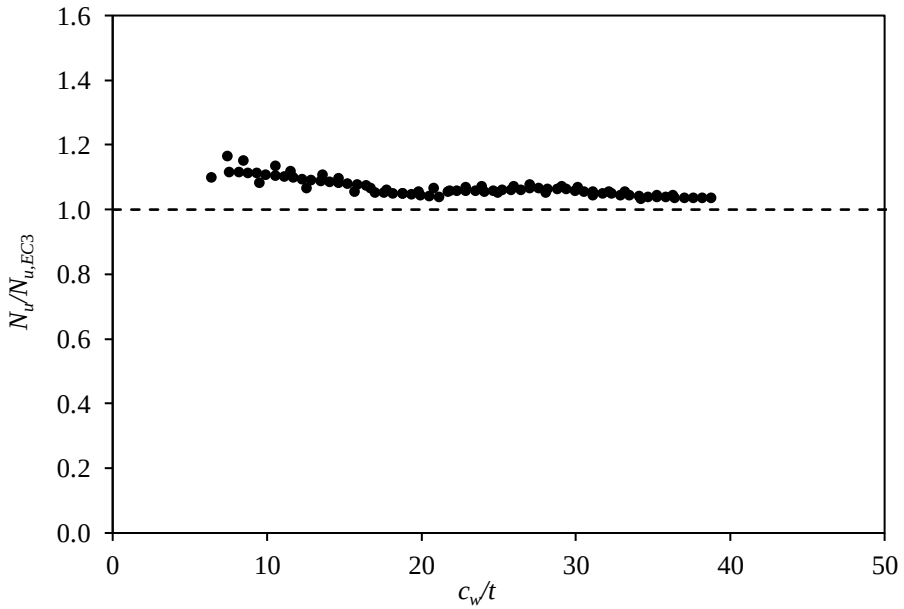

Figure 3.21: Comparisons of test and FE failure loads with EC3 cross-section compression resistance predictions.

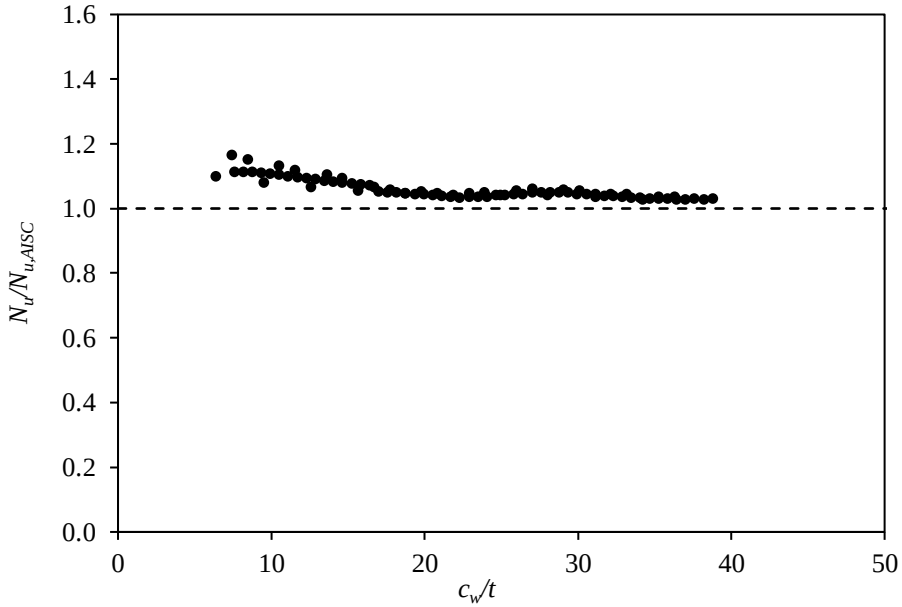

Figure 3.22: Comparison of test and FE failure loads with AISC cross-section compression resistance predictions.

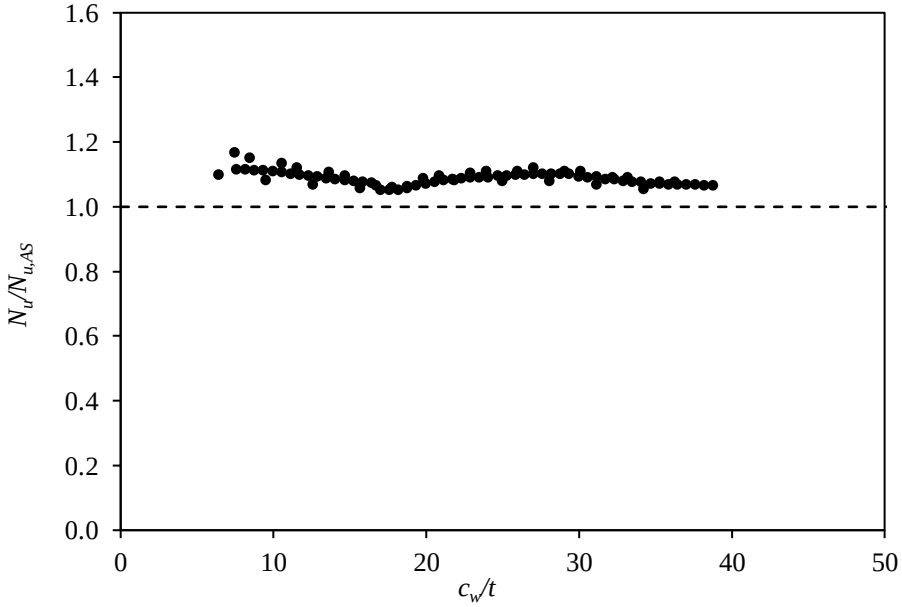

Figure 3.23: Comparison of test and FE failure loads with AS cross-section compression resistance predictions.

3.5 Concluding remarks

Testing and numerical modelling have been conducted to investigate the membrane residual stresses and local buckling behaviour of S960 ultra-high strength steel welded I-section stub columns. The testing programme included material tensile coupon tests, membrane residual stress measurements, initial local geometric imperfection measurements and stub column tests. A predictive model that is capable of capturing membrane residual stresses in S960 ultra-high strength steel welded I-sections was developed, based on the measured data. Following the testing programme, numerical modelling was performed, with FE models firstly developed and validated against the experimental results and then employed to carry out a series of parametric studies to generate further numerical data on S960 ultra-high strength steel welded I-section stub columns. The obtained test and numerical data were adopted to evaluate the applicability of the established codified design provisions for S700 (or S690) high strength steel welded I-section stub columns to their S960 ultra-high strength steel counterparts. The quantitative and graphical evaluation results indicated that (i) the slenderness limits for outstand and internal plate elements in compression, as set out in EN 1993-1-12 (CEN, 2007), ANSI/AISC 360-16 (AISC, 2016) and AS 4100 (AS, 2016), can be accurately used for classifying flanges and webs of S960 ultra-high strength steel welded I-section stub columns and (ii) all three sets of codified design provisions yield accurate and consistent cross-section compression resistance predictions when used for S960 ultra-high strength steel welded I-section stub columns.

CHAPTER 4

FLXURAL BUCKLING OF S960 ULTRA-HIGH STRENGTH STEEL WELDED I-SECTION COLUMNS

4.1 Introduction

This chapter reports a thorough experimental and numerical study of the structural behaviour and resistances of S960 ultra-high strength steel welded I-section columns failing by flexural buckling about the minor principal axis. A testing programme, including initial geometric imperfection measurements and ten pin-ended column tests, was conducted. The testing programme was accompanied by a numerical modelling programme, where finite element models were firstly developed and validated against the test results, and then employed to perform parametric studies to generate further numerical data. The existing codes in Europe, America and Australia only cover the design of steel structures with nominal material yield stresses less than or equal to 700 MPa (or 690 MPa), and design of S960 ultra-high strength steel welded I-section columns is therefore out of their application scopes. The obtained test and numerical results were adopted to assess the applicability of the relevant codified design buckling curves for S700 (or S690) high strength steel welded I-section columns failing by minor-axis flexural buckling to their S960 ultra-high strength steel counterparts. The assessment results have been presented in Su et al. (2021a), with a revised Eurocode design buckling curve also proposed.

4.2 Testing

4.2.1 General

A testing programme was firstly conducted to investigate the minor-axis flexural buckling behaviour and resistances of S960 ultra-high strength steel welded I-section columns. Two different I-sections – I-50×50×6 and I-80×60×6 – were fabricated from 6 mm thick S960 ultra-high strength steel sheets through robotic gas metal arc welding (GMAW), and adopted in the testing programme. The detailed fabrication process is described as follows. Specifically, three plates were cut from the 6 mm thick S960 ultra-high strength steel virgin sheets by a laser cutting machine, positioned onto the flat work bench and constructed into a well-aligned I-shaped profile. Two pairs of robotic arms were placed at the web-to-flange junctions of the I-shaped profile and arranged anti-symmetrically in relation to the centreline of the web, and then started welding at the same time. This welding strategy helped minimise the cross-section and member distortion during welding. It is worth noting that the same electrode and the S960 ultra-high strength steel plates as that described in Chapter 3, were used in the current testing programme. As highlighted in Chapter 3, the slenderness limits in three codified standards are applicable to S960 ultra-high strength steel I-sections, both of the two adopted I-sections are therefore classified as Class 1 based on EN 1993-1-12 (CEN, 2007); meanwhile, these two I-sections are also categorised as non-slender cross-sections, according to the limiting width-to-thickness ratios given in ANSI/AISC 360-16 (AISC, 2016) and yield slenderness limits set out in AS 4100 (AS, 2016). For each S960 ultra-high strength steel welded I-section, five column specimens with varying member lengths were prepared, leading to a total of ten column specimens investigated in the experiments. The key geometric dimensions of the ten S960 ultra-high strength steel welded I-section column specimens are reported in Table 4.1, where L is the member length, h is outer

section height, b_f is the flange width and t is the wall thickness – see Figure 4.1, where the notations of the cross-section geometric parameters for welded I-sections are shown. The identifier of each column specimen comprises the cross-section identifier, with 'I1' and 'I2' respectively signifying the welded I-sections I-50×50×6 and I-80×60×6, a letter '*L*' (indicating length) and a number (differentiating the column specimens with the same cross-section size but different member lengths). Overall, the testing programme included material testing and membrane residual stress measurements, initial global and local geometric imperfection measurements and pin-ended column tests.

Table 4.1: Measured geometric dimensions and initial geometric imperfection magnitudes of S960 ultra-high strength steel welded I-section column specimens.

Cross section	Specimen ID	L (mm)	L_e (mm)	h (mm)	b_f (mm)	t (mm)	$\bar{\lambda}$	ω_0 (mm)	ω_g (mm)
I-50×50×6	I1-L1	347	457	49.28	49.24	5.98	0.86	0.05	0.27
	I1-L2	450	560	49.63	49.27	5.98	1.05	0.05	0.28
	I1-L3	549	659	49.87	49.22	6.03	1.24	0.05	0.36
	I1-L4	650	760	49.54	49.25	5.99	1.43	0.05	0.49
	I1-L5	747	857	49.86	49.67	6.06	1.60	0.05	0.58
I-80×60×6	I2-L1	448	558	80.25	59.35	6.03	0.92	0.07	0.28
	I2-L2	548	658	80.20	59.37	6.04	1.09	0.07	0.31
	I2-L3	650	760	80.51	59.68	6.01	1.25	0.07	0.47
	I2-L4	746	856	80.82	59.42	6.02	1.41	0.07	0.52
	I2-L5	844	954	79.52	59.48	5.99	1.56	0.07	0.64

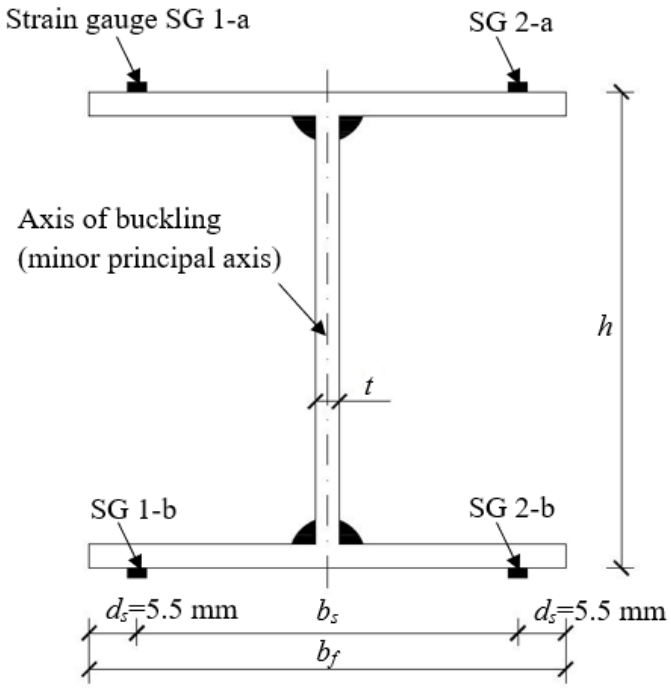

Figure 4.1: Notations of welded I-sections and locations of strain gauges attached to column specimens.

4.2.2 Initial geometric imperfection measurements

Initial geometric imperfections influence the structural behaviour and resistances of thin-walled steel members; therefore, the initial global and local geometric imperfections (as schematically shown in Figure 4.2) of the column specimens were measured. The test setup for initial global geometric imperfection measurements is depicted in Figure 4.3, where a column specimen is positioned on the flat work bench of a CNC router, and a LVDT is mounted onto the arm of the CNC router, moving along the centreline of the web of the column specimen, with the readings recorded at the two ends and mid-height. The initial mid-height global geometric imperfection of each column specimen to the minor principal axis ω_g was taken as the deviation from a linear reference line (i.e. a straight line connecting the measured data points at the two ends) to the measured data point at the mid-height, with the magnitude

reported in Table 4.1. Direct initial local geometric imperfection measurements on the column specimens were significantly influenced by the presence of the member initial global geometric imperfections, and therefore their initial local geometric imperfection magnitudes were taken as those measured from the corresponding stub column specimens with the same cross-section sizes, as reported in Chapter 3.

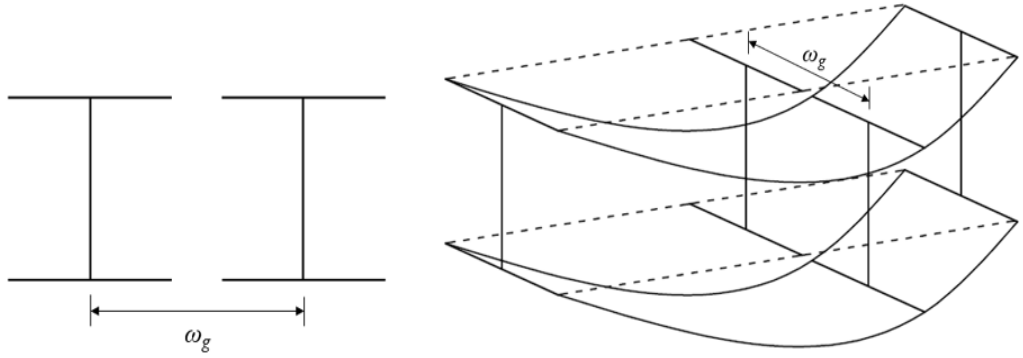

(a) Initial global geometric imperfection

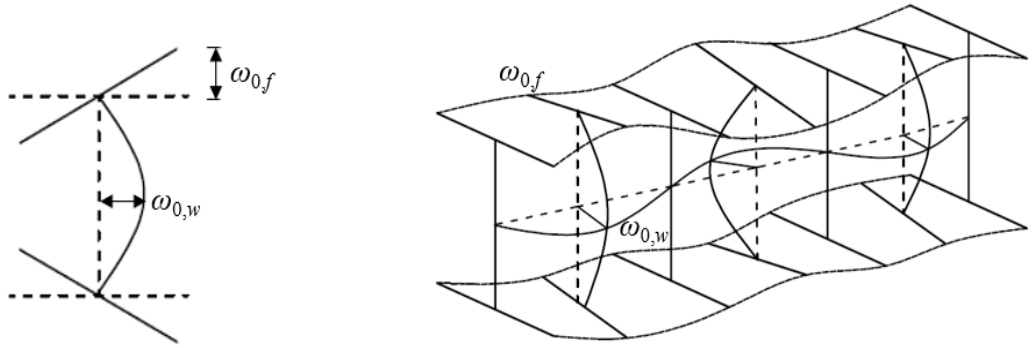

(b) Initial local geometric imperfection

Figure 4.2: Illustration of initial local and global geometric imperfections.

Figure 4.3: Test setup for initial global geometric imperfection measurements.

4.2.3 Pin-ended column tests

The minor-axis flexural buckling behaviour and resistances of S960 ultra-high strength steel welded I-section columns were investigated through pin-ended column tests. A displacement-controlled INSTRON 5000 kN servo-hydraulic testing machine was used to perform all the column tests, with a constant loading rate equal to 0.3 mm/min. Figure 4.4(a) and Figure 4.4(b) depict a photograph and a schematic diagram of the pin-ended column test setup, respectively. Each end of the testing machine was equipped with a knife-edge device, consisting of a pit plate with a semi-circular groove and a wedge plate with a knife-edge wedge, to offer pin-ended boundary conditions to the ends of the column specimens about the minor principal axis (i.e. the axis of buckling). Prior to testing, a column specimen was placed between the top and bottom wedge plates, and their relative position, monitored by means of the spirit levels and lasers, was adjusted such that (i) the member longitudinal axis was perpendicular to the wedge plates and also intersected with the

knife-edges and (ii) the cross-section minor principal axis was parallel to the knife-edges. The column specimen was then anchored at both ends by stiffening plates (bolted to the wedge plates), before placed between the top and bottom pit plates of the testing machine. Note that the distance from the end of the column specimen to the rotation centre of the knife-edge device is equal to 55 mm, and therefore the effective member length of each column specimen is given as L_e=L+110 mm and the corresponding member non-dimensional slenderness about the minor principal axis $\bar{\lambda}$ is determined by Equation (4.1), where A is the cross-section area and I is the second moment of area about the minor principal axis; both L_e and $\bar{\lambda}$ are reported in Table 4.1.

$$\bar{\lambda} = \sqrt{\frac{Af_y L_e^2}{\pi^2 EI}} \tag{4.1}$$

With regard to the instrumentation employed for the pin-ended column tests, as shown in Figure 4.4, a LVDT was attached to the web of the column specimen at mid-height to measure the lateral deflection along the flexural buckling direction (i.e. to the minor principal axis) and two pairs of strain gauges were attached to the mid-height of the column specimen, with the detailed locations depicted in Figure 4.1, to monitor the longitudinal strains at these locations. The readings from the LVDT and strain gauges were used to calculate the actual overall global geometric imperfection magnitude, defined as the sum of the initial mid-height global geometric imperfection magnitude ω_g and the initial loading eccentricity e_0, for each S960 ultra-high strength steel welded I-section column specimen, based on Equation (4.2) (Zhao et al., 2016; Buchanan et al., 2018; Chen and Young, 2020; Sun et al., 2020), where ε_{max}-ε_{min} is the difference of the longitudinal strains measured by the two pairs of strain gauges, N is the applied compression load, b_f-2d_s is the distance between the two pairs of strain gauges – see Figure 4.1, and Δ is the mid-height lateral deflection measured by the LVDT. Note that Equation (4.2) was derived based on the assumption of linear elastic

structural behaviour and it was recommended that no more than 15% of the expected failure load be used in the calculation of the overall global geometric imperfection magnitude (ω_g+e_0) (Zhao et al., 2016; Buchanan et al., 2018; Sun et al., 2020). If the calculated overall global geometric imperfection magnitude (ω_g+e_0) exceeded L_e/1000, the position of the column specimen was then carefully re-adjusted until the achievement of (ω_g+e_0)<L_e/1000 (Gardner et al., 2016; Buchanan et al., 2018; Sun et al., 2020).

$$\omega_g + e_0 = \frac{EI(\varepsilon_{max} - \varepsilon_{min})}{N(b_f - 2d_s)} - \Delta \tag{4.2}$$

All the S960 ultra-high strength steel welded I-section column specimens were found to exhibit minor-axis flexural buckling upon testing; the deformed failure modes of the I-50×50×6 column specimens with member non-dimensional slendernesses ranging from 0.86 to 1.60 are shown in Figure 4.5. The load–mid-height lateral deflection curves are displayed in Figures 4.6 and 4.7 for the I-50×50×6 and I-80×60×6 column specimens, respectively. Table 4.2 reports the key test results, including the overall global geometric imperfection magnitude (ω_g+e_0), the normalised overall global geometric imperfection magnitude (ω_g+e_0)/L_e, the failure load N_u and the mid-height lateral deflection at the failure load Δ_u.

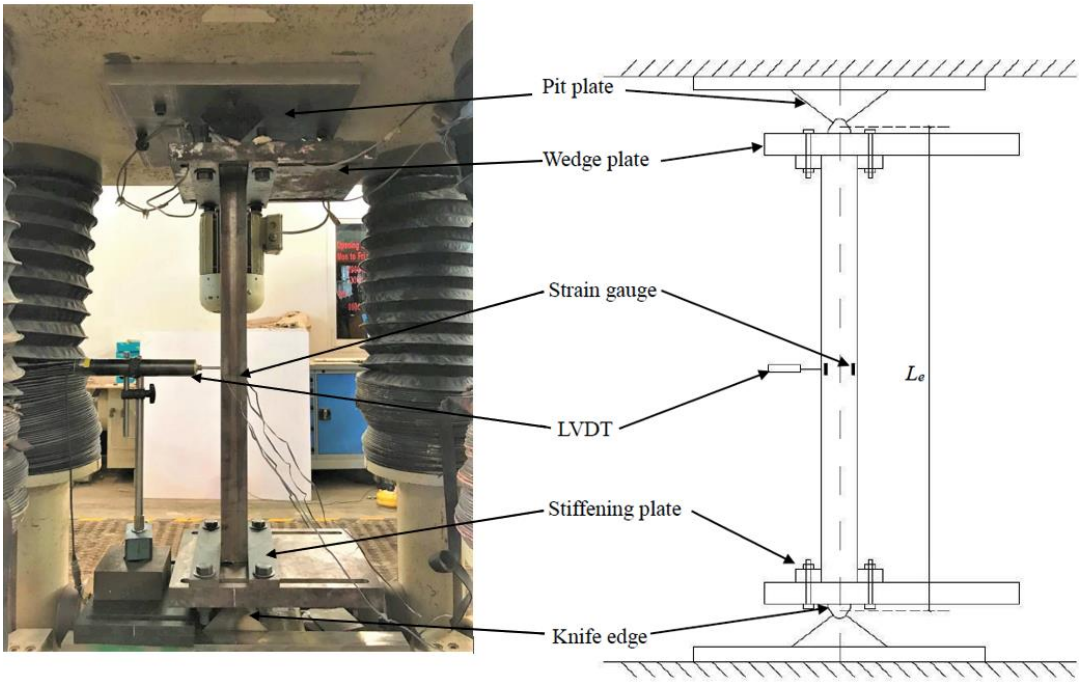

(a) Photograph. **(b)** Schematic diagram.

Figure 4.4: Pin-ended column test setup.

Figure 4.5: Flexural buckling failure modes of typical S960 ultra-high strength steel welded I-section column specimens (from left to right: I1-L1, I1-L2, I1-L3, I1-L4 and I1-L5).

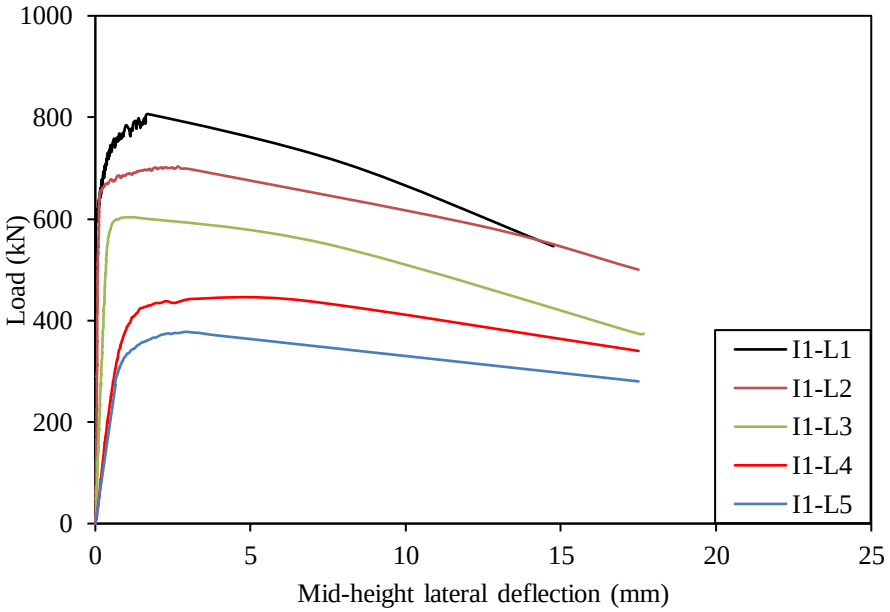

Figure 4.6: Load–mid-height lateral deflection curves for I-50×50×6 column specimens.

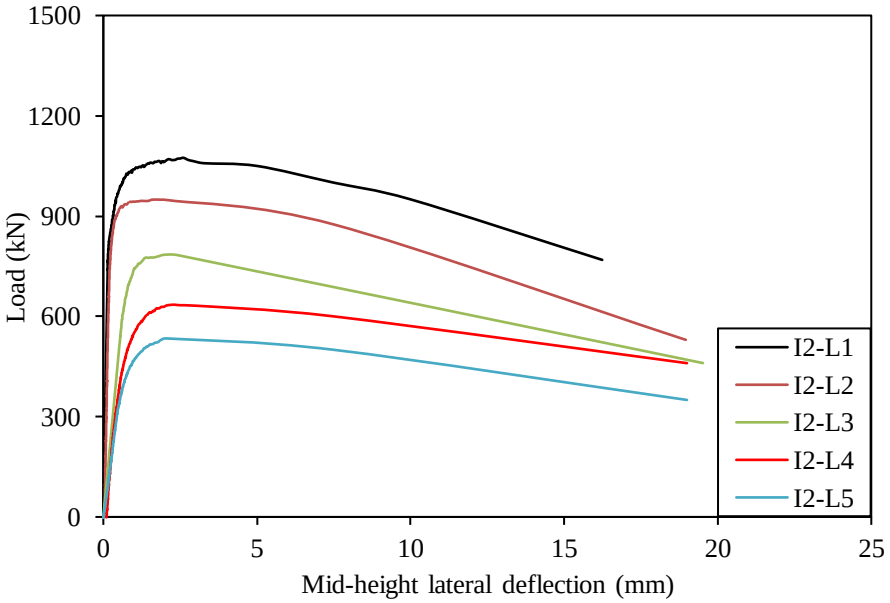

Figure 4.7: Load–mid-height lateral deflection curves for I-80×60×6 column specimens.

Table 4.2: Key test results for S960 ultra-high strength steel welded I-section column specimens.

Cross-section	Specimen ID	ω_g+e_0 (mm)	$(\omega_g+e_0)/L_e$	N_u (kN)	Δ_u (mm)
I-50×50×6	I1-L1	0.39	1/1172	806.50	1.6
	I1-L2	0.47	1/1191	703.35	2.5
	I1-L3	0.56	1/1177	603.20	1.3
	I1-L4	0.64	1/1188	442.50	6.7
	I1-L5	0.79	1/1085	377.55	2.7
I-80×60×6	I2-L1	0.46	1/1213	1074.20	2.9
	I2-L2	0.54	1/1219	949.25	2.2
	I2-L3	0.67	1/1134	784.25	2.4
	I2-L4	0.71	1/1205	634.90	2.5
	I2-L5	0.88	1/1084	533.95	2.2

4.3 Numerical modelling

4.3.1 General

Following the testing programme, a numerical modelling programme was conducted using the nonlinear finite element (FE) software ABAQUS (2014). FE models were firstly developed and validated against the test results. Upon validation, the FE models were employed to perform parametric studies to generate further numerical data over a wide range of cross-section dimensions and member effective lengths.

4.3.2 Development of FE models

FE models were developed according to the measured cross-section dimensions and member effective lengths, as reported in Table 4.1. The four-node shell element S4R (ABAQUS, 2014) was also employed in the present numerical modelling. A mesh sensitive study was conducted to seek suitable element sizes that allowed for accurate incorporation of membrane residual stresses into the S960 ultra-high strength steel welded I-section column FE models and also led to adequate computational accuracy

and efficiency; a series of element sizes ranging from 0.5t to 3t were examined in the mesh sensitive study, and an element size equal to the wall thickness t was finally selected. Regarding the material modelling of grade S960 ultra-high strength steel, the plastic material model with isotropic hardening, as provided in ABAQUS (2014), was adopted. It requires the inputted material properties to be specified in the form of true stress and true plastic strain. Therefore, the average measured (engineering) stress–strain curve of the longitudinal coupons was converted into the true stress–plastic strain curve, based on Equations (4.3) and (4.4), where σ_{true} is the true stress, ε_{ln}^{pl} is the true plastic strain, and σ_{nom} and ε_{nom} are respectively the engineering stress and strain, and then assigned to the FE models.

$$\sigma_{true} = \sigma_{nom}(1+\varepsilon_{nom}) \tag{4.3}$$

$$\varepsilon_{ln}^{pl} = \ln(1+\varepsilon_{nom}) - \frac{\sigma_{nom}}{E} \tag{4.4}$$

For each S960 ultra-high strength steel welded I-section column FE model, the membrane residual stresses, as predicted from the predictive model presented in Chapter 3, were incorporated by means of the 'Predefined Field' command (ABAQUS, 2014). Figure 4.8 depicts the membrane residual stress pattern and amplitudes incorporated into the FE model for a typical column specimen I2-L4. For the ease of setting boundary conditions, each end section of the column FE model was coupled to a concentric reference point, with one reference point allowed to translate in the member longitudinal direction and rotate about the cross-section minor principal axis and the other reference point allowed to rotate about the same axis, in order to mimic the pin-ended boundary conditions that were offered by the knife-edge devices in the column tests. With regard to the incorporation of initial global and local geometric imperfections into each column FE model, an elastic eigenvalue buckling analysis (ABAQUS, 2014) was conducted to obtain the lowest global and local buckling mode shapes, which were adopted as the corresponding

initial global and local geometric imperfection patterns (Yuan et al., 2015; Ma et al., 2017; Buchanan et al., 2018; Sun et al., 2020). Two global geometric imperfection magnitudes, including the measured overall global geometric imperfection magnitude (ω_g+e_0) and L_e/1000, and two local geometric imperfection values, including the measured local geometric imperfection magnitude ω_0 and t/100 (i.e. the verified value in Chapter 3), were employed to scale the corresponding initial global and local geometric imperfection patterns for each column FE model. This led to four combinations of global and local geometric imperfection magnitudes, including (ω_g+e_0) and ω_0, L_e/1000 and ω_0, (ω_g+e_0) and t/100, and L_e/1000 and t/100, which were employed to assess the sensitivity of the developed column FE models to the geometric imperfection magnitudes. Finally, geometrically and materially nonlinear analyses (GMNIA) (Greiner and Lindner, 2006; Taras, 2016; Walport et al., 2019) were carried out by using the modified Risks method (ABAQUS, 2014), to derive the numerical failure loads, load–mid-height lateral deflection curves and failure modes.

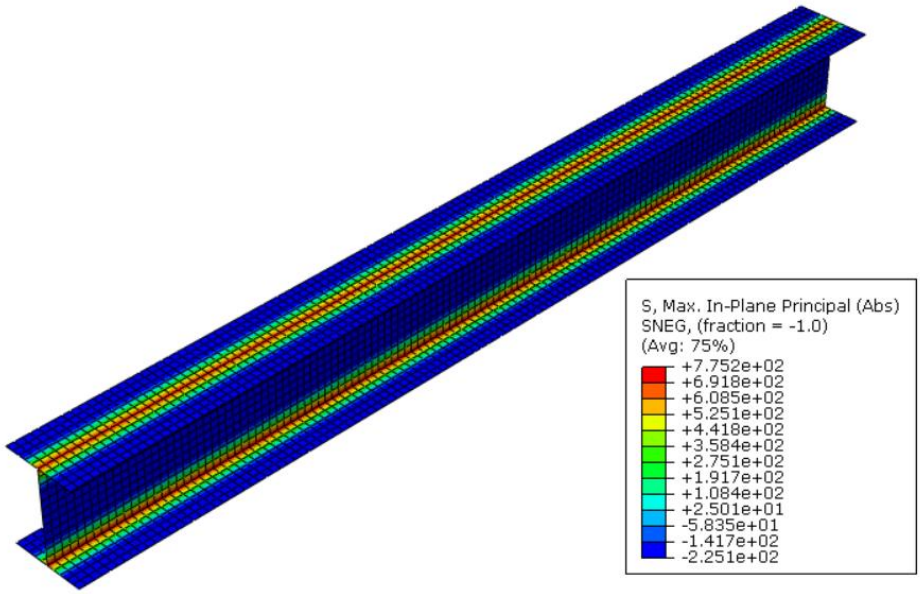

Figure 4.8: Typical membrane residual stress pattern and amplitudes (in MPa) in modelled S960 ultra-high strength steel welded I-section column I2-L4 (Positive values indicate tensile residual stresses while negative values indicate compressive residual stresses).

4.3.3 Validation of FE models

Validation of the developed S960 ultra-high strength steel welded I-section column FE models was conducted through comparisons of the numerically derived results with the corresponding experimental observations. Table 4.3 reports the numerical to test failure load ratios for the ten S960 ultra-high strength steel welded I-section column specimens, indicating that all the four global and local geometric imperfection magnitude combinations generally result in accurate and consistent failure load predictions. Comparisons between the test and numerical load–mid-height lateral deflection curves for typical S960 ultra-high strength steel welded I-section column specimens I1-L4 and I2-L3 are depicted in Figures 4.9 and 4.10, respectively, where the test load–mid-height lateral deflection histories are generally well captured by their numerical counterparts. The test and numerical failure modes for typical column specimens I1-L4 and I2-L3 are presented in Figure 4.11 and 4.12, respectively, exhibiting good agreement. Overall, the developed FE models are capable of simulating the test responses of the S960 ultra-high strength steel welded I-section column specimens failing by minor-axis flexural buckling, and therefore deemed to be validated.

Table 4.3: Comparisons of FE failure loads with test failure loads for varying global and local geometric imperfection magnitude combinations.

Specimen ID	FE N_u / Test N_u			
	$(\omega_g+e_0)+\omega_0$	$L_e/1000+\omega_0$	$(\omega_g+e_0)+t/100$	$L_e/1000+t/100$
I1-L1	0.919	0.908	0.914	0.907
I1-L2	0.943	0.929	0.934	0.928
I1-L3	0.921	0.913	0.918	0.912
I1-L4	0.934	0.924	0.932	0.925
I1-L5	0.914	0.908	0.912	0.908
I2-L1	0.936	0.922	0.934	0.924
I2-L2	0.891	0.884	0.891	0.888
I2-L3	0.936	0.914	0.933	0.924
I2-L4	0.908	0.894	0.904	0.901
I2-L5	0.937	0.924	0.931	0.930
Mean	0.924	0.912	0.920	0.915
COV	0.018	0.016	0.016	0.015

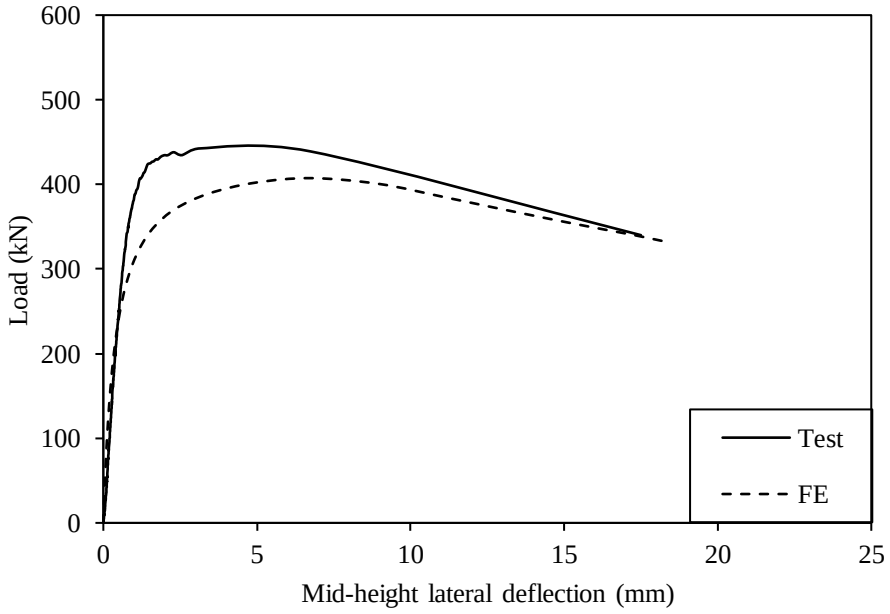

Figure 4.9: Test and numerical load–mid-height lateral deflection curves for S960 ultra-high strength steel welded I-section column specimen I1-L4.

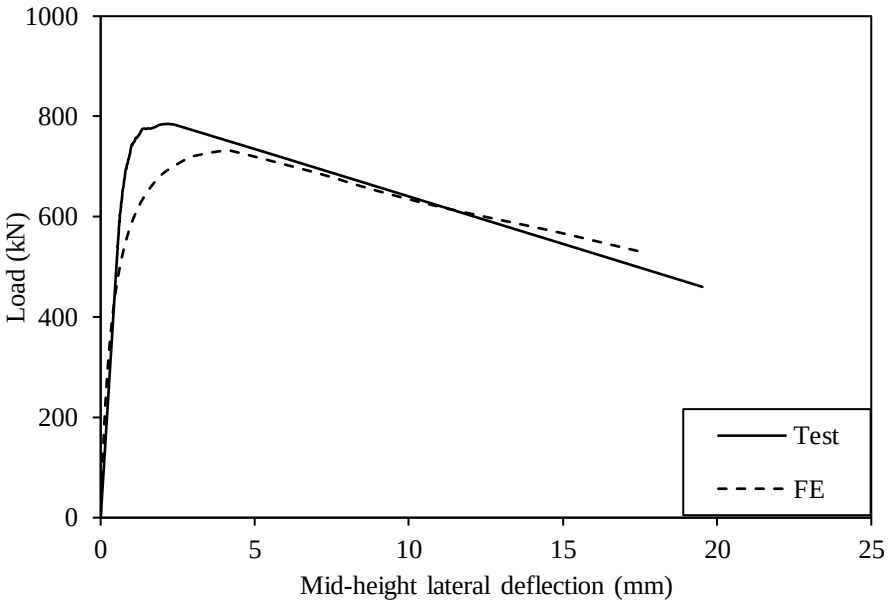

Figure 4.10: Test and numerical load–mid-height lateral deflection curves for S960 ultra-high strength steel welded I-section column specimen I2-L3.

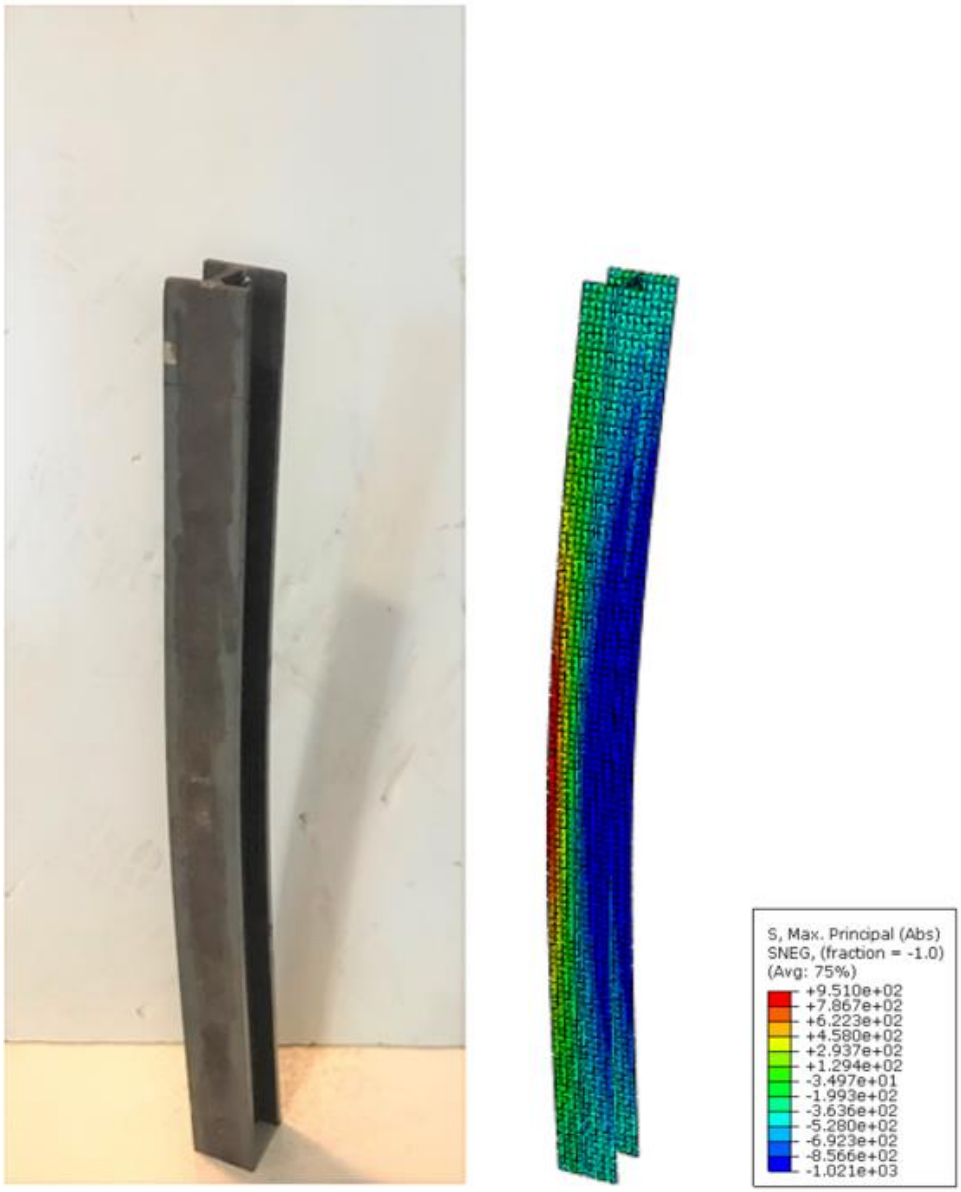

Figure 4.11: Test and numerical failure modes for S960 ultra-high strength steel welded I-section column specimen I1-L4.

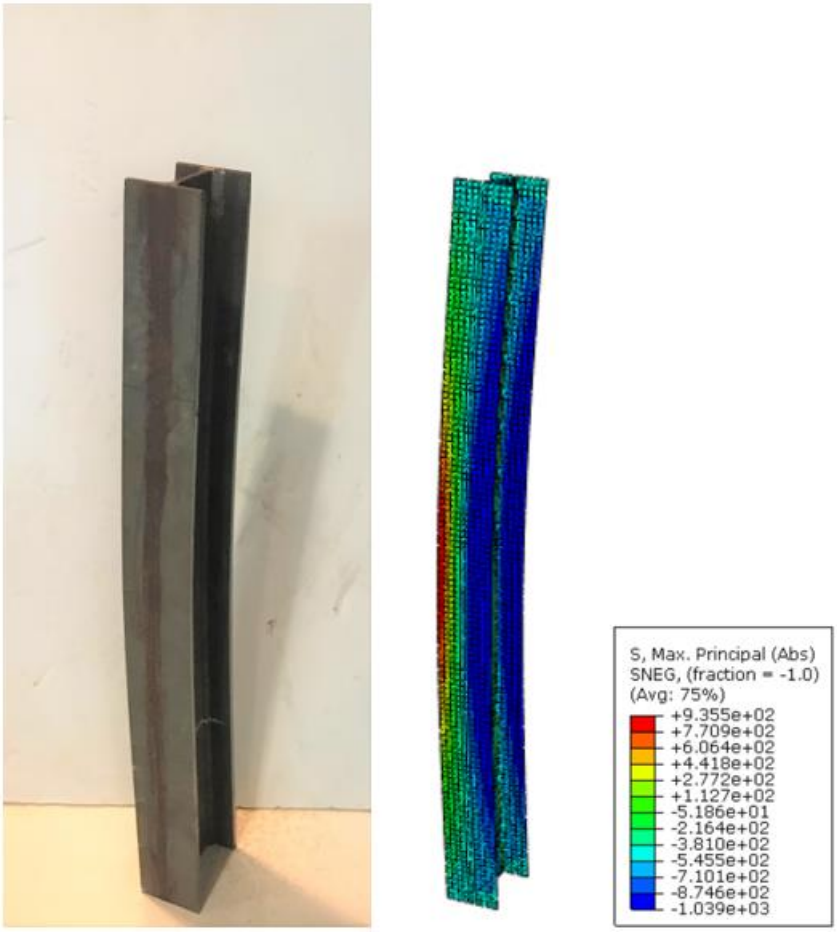

Figure 4.12: Test and numerical failure modes for S960 ultra-high strength steel welded I-section column specimen I2-L3.

4.3.4 Parametric studies

The validated FE models were adopted to perform parametric studies to generate further numerical data over a wide range of cross-section dimensions and member effective lengths. The same modelling procedures and techniques as those described in Chapter 4.3.2 were employed in the present parametric studies. Table 4.4 summaries the key geometric parameters of the modelled S960 ultra-high strength steel welded I-section columns in the parametric studies. Specifically, the outer heights of the modelled I-sections were fixed at 100 mm and the flange widths were varied between 50 mm and 100 mm, leading to the cross-section aspect ratios from 1.0 to 2.0 being considered; the web and flange thicknesses for each modelled I-

section were set to be equal and ranged from 5 mm to 10 mm. The modelled S960 ultra-high strength steel welded I-sections covered all three classes of non-slender cross-sections (i.e. Class 1, 2 and 3) specified in EN 1993-1-12 (CEN, 2007), and also fell in the category of non-slender cross-sections defined in ANSI/AISC 360-16 (AISC, 2016) and AS 4100 (AS, 2016). The effective lengths of the modelled columns were ranged from 260 mm to 2690 mm, resulting in a wide range of member non-dimensional slendernesses $\bar{\lambda}$ from 0.23 to 2.50 being considered. The global and local geometric imperfection magnitude combination of L_e/1000 and t/100 was shown to result in accurate predictions of the test failure loads in Chapter 4.3.3, and thus also adopted in the present parametric studies. Overall, a total of 79 numerical data on S960 ultra-high strength steel welded I-section columns failing by minor-axis flexural buckling were generated through parametric studies.

Table 4.4: Cross-section dimensions and effective member lengths of modelled S960 ultra-high strength steel welded I-section columns in parametric studies.

h (mm)	b_f (mm)	t (mm)	Cross-section class*	L_e (mm)	$\bar{\lambda}$
100	50	7.5	1	310, 450, 530, 630, 820, 960, 1030, 1130	0.63, 0.92, 1.08, 1.29, 1.68, 1.96, 2.11, 2.31
		5.0	2	260, 390, 500, 610, 660, 760, 870, 1140	0.54, 0.81, 1.04, 1.27, 1.38, 1.58, 1.81, 2.38
	60	8.0	1	310, 510, 730, 860, 1010, 1160, 1280, 1410	0.51, 0.84, 1.20, 1.41, 1.66, 1.90, 2.10, 2.31
		5.5	3	260, 460, 700, 830, 970, 1120, 1300, 1400	0.43, 0.77, 1.17, 1.38, 1.61, 1.86, 2.16, 2.33
	75	7.5	2	320, 410, 810, 1060, 1110, 1210, 1360, 1590	0.40, 0.52, 1.02, 1.34, 1.40, 1.53, 1.72, 2.01
		6.0	3	260, 510, 710, 910, 1110, 1210, 1410, 1710	0.33, 0.65, 0.90, 1.16, 1.41, 1.54, 1.79, 2.18
	90	9.0	2	290, 410, 580, 710, 910, 1110, 1510, 1810	0.29, 0.42, 0.59, 0.72, 0.92, 1.13, 1.53, 1.84
		6.5	3	260, 680, 980, 1230, 1440, 1660, 1970, 2220	0.27, 0.70, 1.01, 1.26, 1.48, 1.70, 2.02, 2.28
	100	10.0	2	260, 610, 940, 1280, 1620, 1960, 2300, 2690	0.23, 0.55, 0.84, 1.15, 1.45, 1.76, 2.06, 2.41
		7.0	3	280, 530, 810, 1060, 1340, 1690, 2110	0.25, 0.48, 0.73, 0.96, 1.22, 1.53, 1.91

* The cross-section classes are defined according to EN 1993-1-12 (CEN, 2007).

4.4 Assessment of international design standards and development of new design method

4.4.1 General

The current EN 1993-1-12 (CEN, 2007), ANSI/AISC 360-16 (AISC, 2016) and AS 4100 (AS, 2016) only cover the design of steel structures with nominal material yield stresses less than or equal to 700 MPa (or 690 MPa), and thus none of the current design standards can be directly used for the studied S960 ultra-high strength steel welded I-section columns. In this section, the applicability of the codified design rules for S700 (or S690) high strength steel welded I-section columns was assessed for their S960 ultra-high strength steel counterparts through comparisons of the test and numerical failure loads N_u with the unfactored flexural bucking resistance predictions $N_{u,pred}$. Revised Eurocode design rules were also proposed.

4.4.2 EN 1993-1-12 (EC3)

The European code EN 1993-1-12 (CEN, 2007) provides design rules for high strength steel structural components with material grades greater than S460 up to S700. The buckling curves, which were developed based on the Perry-Robertson buckling formula, were adopted for the design of column members susceptible to global instability (e.g., flexural, torsional and flexural-torsional buckling). The EC3 design resistance of a column $N_{u,EC3}$ is given by Equation (4.5), where χ is the reduction factor, as calculated from Equation (4.6),

$$N_{u,EC3} = \chi A f_y \tag{4.5}$$

$$\chi = \frac{1}{\phi + \sqrt{\phi^2 - \bar{\lambda}^2}} \leq 1 \tag{4.6}$$

where ϕ is a buckling parameter and determined by Equation (4.7), where α is the imperfection factor to consider the effects of membrane residual stresses and initial geometric imperfections on column buckling resistances; for S700 high strength steel welded I-section columns with the flange thicknesses less than or equal to 40 mm failing by minor-axis flexural buckling, it is specified in EN 1993-1-12 (CEN, 2007) (and EN 1993-1-1 (CEN, 2005)) that the buckling curve 'c' should be adopted and the corresponding imperfection factor α is equal to 0.49.

$$\phi = 0.5\left[1+\alpha\left(\bar{\lambda}-0.2\right)+\bar{\lambda}^{2}\right] \tag{4.7}$$

The applicability of the EC3 design buckling curve 'c' for S700 high strength steel welded I-section columns failing by minor-axis flexural buckling to their S960 ultra-high strength steel counterparts was assessed, based on the obtained test and numerical data. The mean ratio of the test and numerical failure loads to the EC3 design flexural buckling resistances $N_u/N_{u,EC3}$, as reported in Table 4.5, is equal to 1.29, with the corresponding coefficient of variation (COV) equal to 0.11, revealing a rather high level of conservatism of the EC3 design flexural buckling resistances. Graphical assessments were also performed, with the results shown in Figure 4.13, where the test and numerical failure loads N_u, normalised by the cross-section yield loads Af_y, are plotted against the member non-dimensional slendernesses $\bar{\lambda}$ and compared with the EC3 design buckling curve 'c', and Figure 4.14, where the test and numerical to EC3 predicted failure load ratios $N_u/N_{u,EC3}$ are plotted against the member non-dimensional slendernesses $\bar{\lambda}$. The results of the graphical assessment also revealed that the design buckling curve 'c' given in EN 1993-1-12 (CEN, 2007) yields conservative flexural buckling resistance predictions, especially for those intermediate columns with member non-dimensional slendernesses ranging from 0.6 to 1.6. It may thus be concluded that the EC3 design buckling curve 'c' leads to safe but rather conservative resistance predictions when used for S960 ultra-high strength steel welded I-section columns failing by minor-axis flexural buckling.

Table 4.5: Comparisons of test and numerical failure loads with flexural buckling resistance predictions.

No. of test data: 10 No. of FE data: 79	$N_u/N_{u,EC3}$	$N_u/N_{u,AISC}$	$N_u/N_{u,AS}$	$N_u/N_{u,pr}$
Mean	1.29	1.10	1.27	1.09
COV	0.11	0.07	0.11	0.07

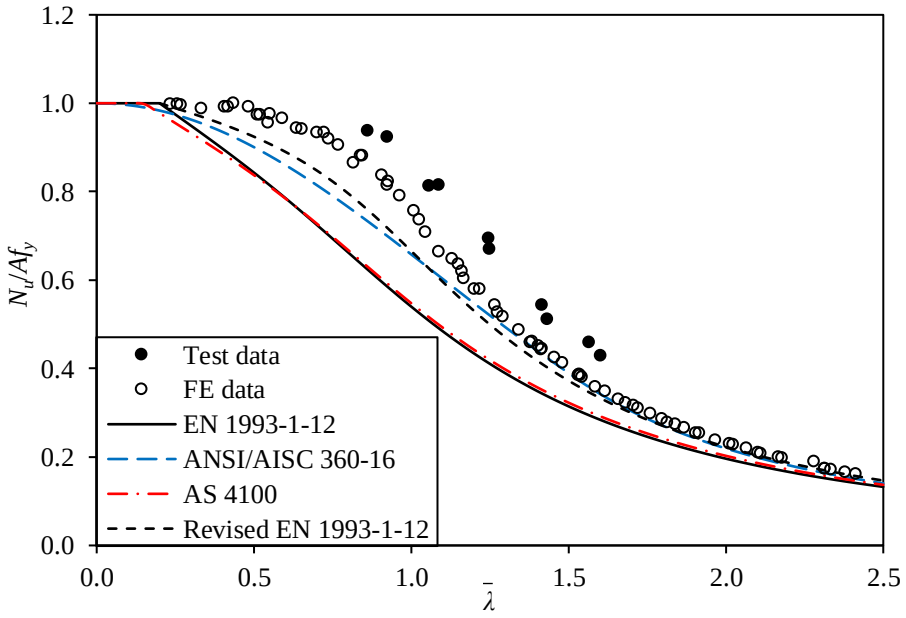

Figure 4.13: Comparisons of test and numerical failure loads with codified and revised design buckling curves.

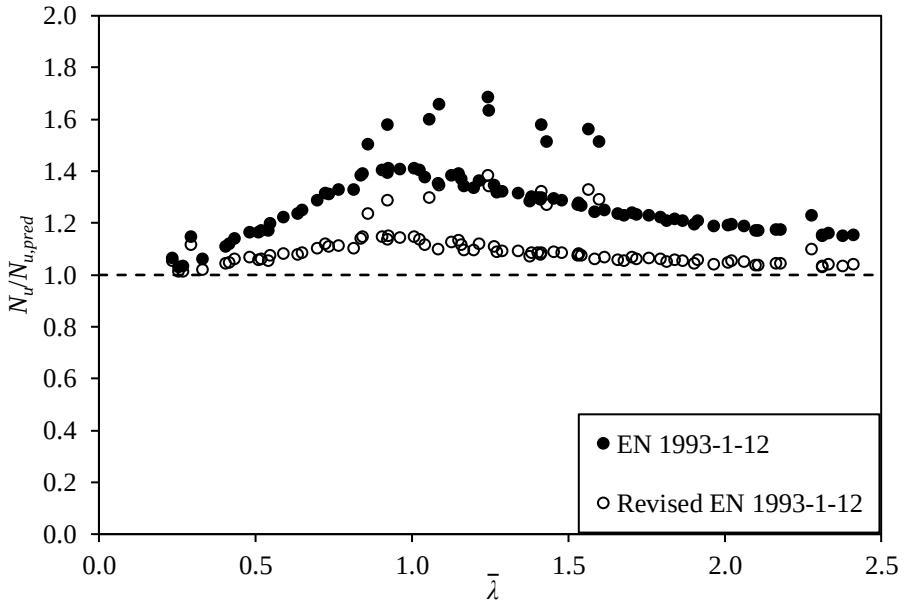

Figure 4.14: Comparisons of test and numerical failure loads with flexural buckling resistance predictions from EN 1993-1-12 (CEN, 2007) and revised EN 1993-1-12 design approach.

4.4.3 ANSI/AISC 360-16 (AISC)

The American specification ANSI/AISC 360-16 (AISC, 2016) covers the design of steel structures with nominal material yield stresses up to 690 MPa. For a non-slender element compression member failing by flexural buckling, the design resistance $N_{u,AISC}$ is calculated as the product of the critical stress F_{cr} and the gross area of the cross-section A, as given by Equation (4.8), where the critical stress F_{cr} is dependent on the member non-dimensional slenderness $\bar{\lambda}$ and can be calculated from Equation (4.9).

$$N_{u,AISC} = F_{cr} A \tag{4.8}$$

$$F_{cr} = \begin{cases} 0.658^{\bar{\lambda}^2} f_y & \text{for} \quad \bar{\lambda} \leq 1.5 \\ \dfrac{0.877}{\bar{\lambda}^2} f_y & \text{for} \quad \bar{\lambda} > 1.5 \end{cases} \tag{4.9}$$

Graphical and quantitative assessments of the applicability of the AISC design buckling curve (as defined by Equation (4.9)) to S960 ultra-high strength steel welded I-section columns were performed through comparisons against the test and numerical failure loads. The AISC design buckling curve, as plotted in Figure 4.13, was generally shown to well capture the test and numerical data points over the whole considered range of member non-dimensional slenderness, though a small disparity existed for member non-dimensional slendernesses ranging from 0.6 to 1.0. This is also evident in Figure 4.15, where the ratios of the test and numerical failure loads to the AISC design flexural buckling resistances $N_u/N_{u,AISC}$ are plotted against the member non-dimensional slendernesses $\overline{\lambda}$. The quantitative assessment results are reported in Table 4.5, where the mean ratio of $N_u/N_{u,AISC}$ is equal to 1.10, with the corresponding COV of 0.07. Overall, the AISC design buckling curve was generally found to yield a high degree of accuracy and consistency when applied to S960 ultra-high strength steel welded I-section columns failing by minor-axis flexural buckling.

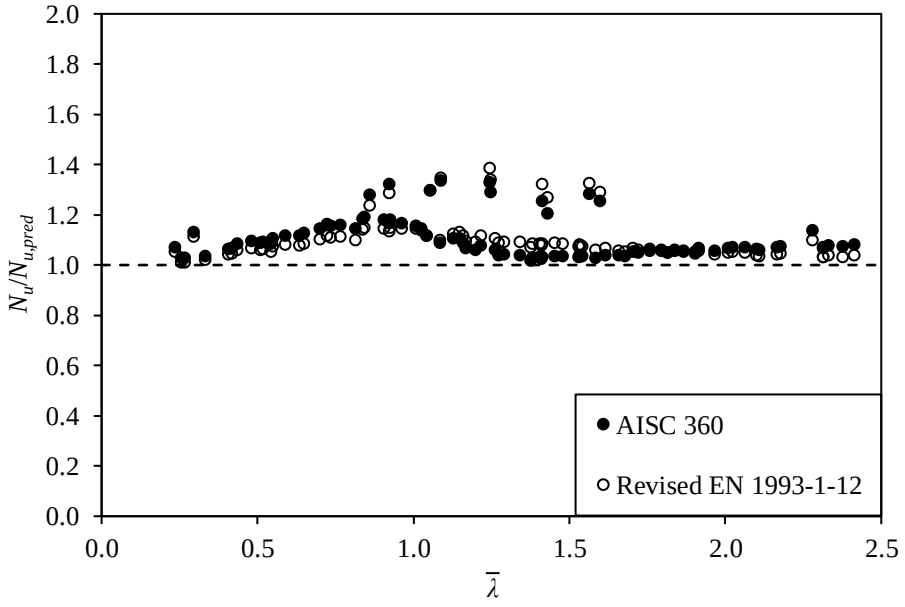

Figure 4.15: Comparisons of test and numerical failure loads with flexural buckling resistance predictions from ANSI/AISC 360-16 (AISC, 2016) and revised EN 1993-1-12 design approach.

4.4.4 AS 4100 (AS)

The Australian standard AS 4100 (AS, 2016) is applicable to steel structures with nominal material yield stresses less than or equal to 690 MPa. For a column member with uniform cross-section profile throughout the member length, the design compression resistance $N_{u,AS}$ is calculated as the member slenderness reduction factor α_c multiplied by the cross-section yield load Af_y – see Equation (4.10), where the member slenderness reduction factor α_c is determined from Equation (4.11),

$$N_{u,AS} = \alpha_c A f_y \tag{4.10}$$

$$\alpha_c = \xi\left[1-\sqrt{1-\left[\frac{90}{\xi\left(\lambda_n+\alpha_a\alpha_b\right)}\right]^2}\right] \le 1 \tag{4.11}$$

where λ_n is the modified member slenderness and given by Equation (4.12), α_a is the compression member factor and calculated from Equation (4.13), α_b is the member section constant and equal to 0.5 for welded I-sections fabricated from hot-rolled plates, and ξ is a buckling parameter, as determined from Equation (4.14), where η is the compression member imperfection factor and can be calculated from Equation (4.15).

$$\lambda_n = \sqrt{\frac{\pi^2 E}{250}}\bar{\lambda} \tag{4.12}$$

$$\alpha_a = \frac{2100\left(\lambda_n - 13.5\right)}{\lambda_n{}^2 - 15.3\lambda_n + 2050} \tag{4.13}$$

$$\xi = \frac{\left(\frac{\lambda_n+\alpha_a\alpha_b}{90}\right)^2 + 1 + \eta}{2\left(\frac{\lambda_n+\alpha_a\alpha_b}{90}\right)^2} \tag{4.14}$$

$$\eta = 0.00326\left(\lambda_n + \alpha_a\alpha_b - 13.5\right) \ge 0 \tag{4.15}$$

The AS design resistances for S960 ultra-high strength steel welded I-section columns failing by minor-axis flexural buckling were evaluated through comparisons against the test and numerical failure loads. The mean test and numerical to AS predicted failure load ratio $N_u/N_{u,AS}$ and the corresponding COV, as reported in Table 4.5, are equal to 1.27 and 0.11, respectively, indicating that the AS design flexural buckling resistances are unduly conservative and only slightly more accurate than their EC3 counterparts. The conservatism of the AS design flexural buckling resistances is also evident in Figure 4.16, where the test and numerical to AS predicted failure load ratios $N_u/N_{u,AS}$ are plotted against the member non-dimensional slendernesses $\bar{\lambda}$. The AS design buckling curve, as defined by Equations (4.11)–(4.15), is plotted in Figure 4.13, and shown to lie considerably below the test and numerical data points, indicating a low level of accuracy.

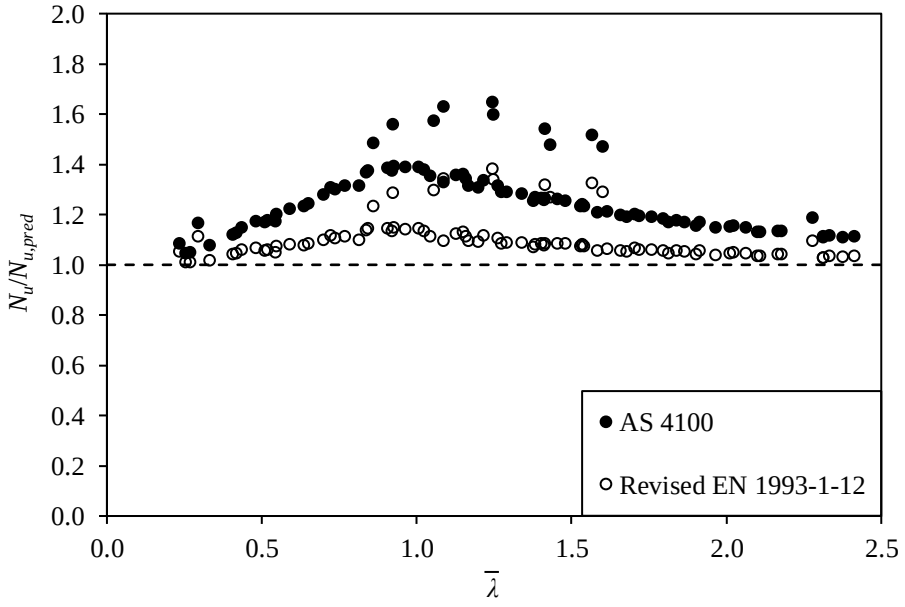

Figure 4.16: Comparisons of test and numerical failure loads with flexural buckling resistance predictions from AS 4100 (AS, 2016) and revised EN 1993-1-12 design approach.

4.4.5 Revised EC3 design approach

Given that the current EN 1993-1-12 (CEN, 2007) results in rather conservative resistance predictions for S960 ultra-high strength steel welded I-section columns failing by minor-axis flexural buckling, revised EN 1993-1-12 design rules are developed in this part. It was proposed that the EC3 design buckling curve 'a', as defined by Equations (4.6) and (4.7) with the imperfection factor α=0.21, be adopted in replacement of the currently used EC3 design buckling curve 'c' for S960 ultra-high strength steel welded I-section columns failing by minor-axis flexural buckling. The proposed EC3 design buckling curve 'a', as plotted in Figure 4.13, exhibits excellent agreement with the experimental and numerical data points over the whole considered range of member non-dimensional slenderness, in comparison with the original EC3 design buckling curve 'c', which lies considerably below the experimental and numerical data points. The flexural buckling resistances predicted from the proposed EC3 design buckling curve 'a' were graphically compared with the test and numerical failure loads, with the results shown in Figure 4.14. Quantitative evaluation of the accuracy of the proposed EC3 design buckling curve 'a' was also conducted, with the mean test and numerical to predicted failure load ratio $N_u/N_{u,pr}$ equal to 1.09 and the corresponding COV equal to 0.07 – see Table 4.5. Both the graphical and quantitative evaluations indicated that the proposed EC3 design buckling curve 'a' yields substantially more accurate and consistent resistance predictions for S960 ultra-high strength steel welded I-section columns failing by minor-axis flexural buckling than the original EC3 design buckling curve 'c'.

4.5 Concluding remarks

A comprehensive testing and numerical modelling programme has been conducted to investigate the structural behaviour and resistances of S960 ultra-high strength steel

welded I-section columns failing by minor-axis flexural buckling. A testing programme was firstly conducted on two S960 ultra-high strength steel welded I-sections, and included initial global and local geometric imperfection measurements and ten pin-ended column tests. A numerical modelling programme was then carried out; FE models were initially developed to simulate the test structural responses and afterwards employed to perform parametric studies to generate further numerical data over a wide range of cross-section dimensions and member effective lengths. The obtained test and numerical results were employed to assess the applicability of the relevant design rules for S700 (or S690) high strength steel welded I-section columns failing by minor-axis flexural buckling, as set out in EN 1993-1-12 (CEN, 2007), ANSI/AISC 360-16 (AISC, 2016) and AS 4100 (AS, 2016), to their S960 ultra-high strength steel counterparts. The results of the graphical and quantitative assessments revealed that (i) both EN 1993-1-12 (CEN, 2007) and AS 4100 (AS, 2016) yield a high degree of conservatism in the prediction of minor-axis flexural buckling resistances for S960 ultra-high strength steel welded I-section columns, and (ii) ANSI/AISC 360-16 (AISC, 2016) results in overall accurate and consistent flexural buckling resistance predictions, though the predicted resistances are marginally conservative for those relatively short S960 ultra-high strength steel welded I-section columns with member non-dimensional slendernesses from 0.6 to 1.0. Finally, the EC3 design buckling curve ‘a’ was proposed to replace the currently used EC3 design buckling curve ‘c’ in the design of S960 ultra-high strength steel welded I-section columns failing by flexural buckling about the minor principal axis, and shown to result in a much higher degree of design accuracy and consistency.

CHAPTER 5

LOCAL–FLEXURAL INTERACTIVE BUCKLING OF S960 ULTRA-HIGH STRENGTH STEEL SLENDER WELDED I-SECTION COLUMNS

5.1 Introduction

Chapter 4 reports the flexural buckling behaviour of S960 ultra-high strength steel non-slender welded I-section columns, while this chapter reports the extensive experimental and numerical investigation of the local–flexural interactive buckling behaviour and resistances of S960 ultra-high strength steel slender welded I-section columns. The local–flexural buckling interaction refers to the member global buckling combined with the plate element buckling and no existing research focuses on S960 ultra-high strength steel welded I-section columns failing by this buckling mode. The experimental investigation was thus conducted, including initial geometric imperfection measurements and ten pin-ended column tests. The experimental investigation was accompanied by a numerical modelling study, where finite element models were firstly developed and validated against the test results, and then employed to perform parametric studies to generate further numerical data. As mentioned before, the existing codes in Europe, America and Australia only cover the design of steel structures with material grades up to S700 (or S690), and design of S960 ultra-high strength steel slender welded I-section columns is therefore out of their application scopes. The obtained test and numerical data were adopted to assess the applicability of the relevant codified buckling curves and design rules for S700 (or S690) high strength steel slender welded I-section columns failing by local–flexural buckling to their S960 ultra-high strength steel counterparts. The assessment

results have been reported in Su et al. (2021e), with a revised design approach proposed.

5.2 Testing

5.2.1 General

The experimental investigation was firstly conducted to investigate the local– flexural buckling behaviour and resistances of S960 ultra-high strength steel slender welded I-section columns. Two different I-sections – I-120×120×6 and I-150×75×6 – were fabricated from 6 mm thick S960 ultra-high strength steel sheets through robotic gas metal arc welding (GMAW), and adopted in the experimental investigation. The detailed fabrication process and the properties of the utilised electrode and the S960 ultra-high strength steel plates are same as those described in Chapter 4. Both of the two adopted I-sections are classified as Class 4, based on the slenderness limits set out in EN 1993-1-12 (CEN, 2007) and categorised as slender cross-sections, according to the limiting width-to-thickness ratios given in ANSI/AISC 360-16 (AISC, 2016) and yield slenderness limits set out in AS 4100 (AS, 2016). For each S960 ultra-high strength steel slender welded I-section, five column specimens with different member lengths were prepared, leading to a total of ten column specimens examined in the experimental investigation. The key geometric dimensions of the ten S960 ultra-high strength steel slender welded I-section column specimens are reported in Table 5.1, where L is the member length, h is outer section height, b_f is the flange width and t is the wall thickness – see Figure 4.1, where the notations of the cross-section geometric parameters for welded I-sections are shown. The identifier of each column specimen comprises the cross-section identifier, with 'I1' and 'I2' respectively signifying the welded I-sections I-120×120×6 and I-150×75×6, a letter '*L*' (indicating length) and a number (differentiating the column specimens

with the same cross-section size but different member lengths). Overall, the experimental investigation included initial global and local geometric imperfection measurements and pin-ended column tests.

Table 5.1: Measured geometric properties of S960 ultra-high strength steel slender welded I-section column specimens.

Cross-section	Specimen ID	L (mm)	L_e (mm)	b_f (mm)	h (mm)	t (mm)	ω_0 (mm)	ω_g (mm)
I-120×120×6	I1-L1	509	619	119.74	119.68	5.98	0.12	0.29
	I1-L2	660	770	119.77	119.43	5.98	0.12	0.43
	I1-L3	827	937	119.72	119.78	6.00	0.12	0.60
	I1-L4	978	1088	119.54	119.72	5.98	0.12	0.72
	I1-L5	1159	1269	119.67	119.86	6.01	0.12	0.82
I-150×75×6	I2-L1	402	512	74.53	150.25	6.03	0.09	0.25
	I2-L2	549	659	74.57	150.23	6.04	0.09	0.37
	I2-L3	667	777	74.33	150.11	6.01	0.09	0.51
	I2-L4	768	878	74.42	150.02	6.02	0.09	0.62
	I2-L5	899	1009	74.68	149.97	5.99	0.09	0.77

5.2.2 Initial geometric imperfection measurements and pin-ended column tests

The structural behaviour and resistances of thin-walled steel members can be influenced by the existence of initial local and global geometric imperfections, which are thus measured before testing. The test setup for initial global geometric imperfection measurements is the same as that described in Chapter 4, while the initial local geometric imperfection measurements on the column specimens were taken as those measured from the corresponding stub column specimens with the same cross-section dimensions, as presented in Chapter 3.

The local–flexural buckling behaviour and resistances of S960 ultra-high strength steel slender welded I-section columns were investigated through pin-ended column

tests. The test setup and experimental procedures are same as those adopted in Chapter 4. Note that Equation (4.2) is also applied herein to calculate the overall global geometric imperfection magnitude ($e_0+\omega_g$), with the largest derived ($e_0+\omega_g$) of all the tested specimens being 1/1135, as reported in Table 5.2.

All the S960 ultra-high strength steel slender welded I-section column specimens were found to exhibit local–flexural interactive buckling upon testing; the typical failure modes of the I-120×120×6 column specimens are shown in Figures 5.7 and 5.8. The load–mid-height lateral deflection curves are displayed in Figures 5.1 and 5.2 for the I-120×120×6 and I-150×75×6 column specimens, respectively, while Table 5.2 reports the key test results, including the overall global geometric imperfection magnitude (ω_g+e_0), the normalised overall global geometric imperfection magnitude (ω_g+e_0)/L_e, the failure load N_u and the mid-height lateral deflection at the failure load Δ_u.

The progression of local buckling and global buckling was monitored based on the load–mid-length strain histories. The measured load–mid-length strain histories for typical test specimens I1-L1 and I2-L5 are depicted in Figure 5.3(a) and (b). It is evident that the load–strain histories for the test specimen I1-L1 in Figure 5.3(a) exhibit reversal points, indicating the occurrence of sudden local deformation (i.e. local buckling). However, the load–strain histories for the test specimen I2-L5 in Figure 5.3(b) do not have reversal points, indicating that global buckling occurs before local buckling, i.e. the local–global interactive buckling is triggered by global buckling. The buckling progression observed in the column tests is also consistent with the relative values of the elastic critical local and global buckling stresses, as tabulated in Table 5.2. Regarding the test specimen I1-L1, the minimum of the elastic critical local buckling stresses of flange and web (denoted as $\sigma_{cr,f}$ and $\sigma_{cr,w}$, respectively) is lower than the elastic critical global buckling stress (denoted as $\sigma_{cr,g}$),

revealing that local buckling is more critical. For the test specimen I2-L5, the elastic critical global buckling stress is lower than the minimum of the elastic critical local buckling stresses of flange and web, revealing that global buckling is more critical.

Table 5.2: Key experimental results for S960 ultra-high strength steel slender welded I-section column specimens.

Cross-section	Specimen ID	ω_g+e_0 (mm)	$(\omega_g+e_0)/L_e$	N_u (kN)	Δ_u (mm)	Minimum of $\sigma_{cr,w}$ and $\sigma_{cr,f}$ (MPa)	$\sigma_{cr,g}$ (MPa)	Failure mode driven by
I-120×120×6	I1-L1	0.42	1/1476	1926.6	1.9	878.0	4325.7	Local buckling
	I1-L2	0.53	1/1452	1842.6	3.1	878.5	2802.9	Local buckling
	I1-L3	0.71	1/1324	1755.6	5.1	884.5	1881.4	Local buckling
	I1-L4	0.83	1/1313	1648.5	5.3	880.6	1395.0	Local buckling
	I1-L5	0.94	1/1351	1563.6	8.7	888.4	1029.7	Local buckling
I-150×75×6	I2-L1	0.36	1/1416	1509.7	5.2	1412.1	1875.9	Local buckling
	I2-L2	0.49	1/1347	1334.8	4.5	1417.2	1121.7	Global buckling
	I2-L3	0.63	1/1238	1131.1	5.5	1401.9	796.5	Global buckling
	I2-L4	0.74	1/1189	935.0	15.1	1407.0	629.8	Global buckling
	I2-L5	0.89	1/1135	786.1	10.7	1391.8	480.7	Global buckling

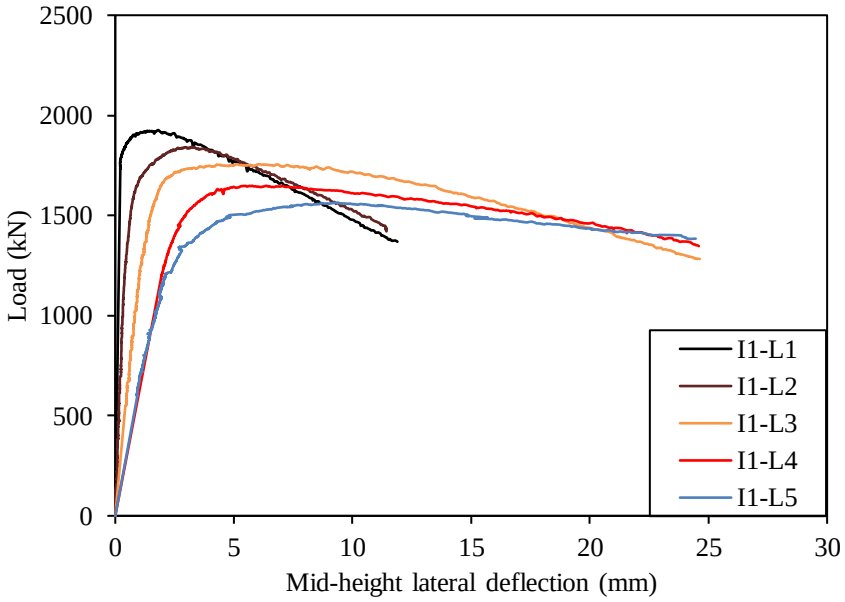

Figure 5.1: Load–mid-height lateral deflection curves for I-120×120×6 column specimens.

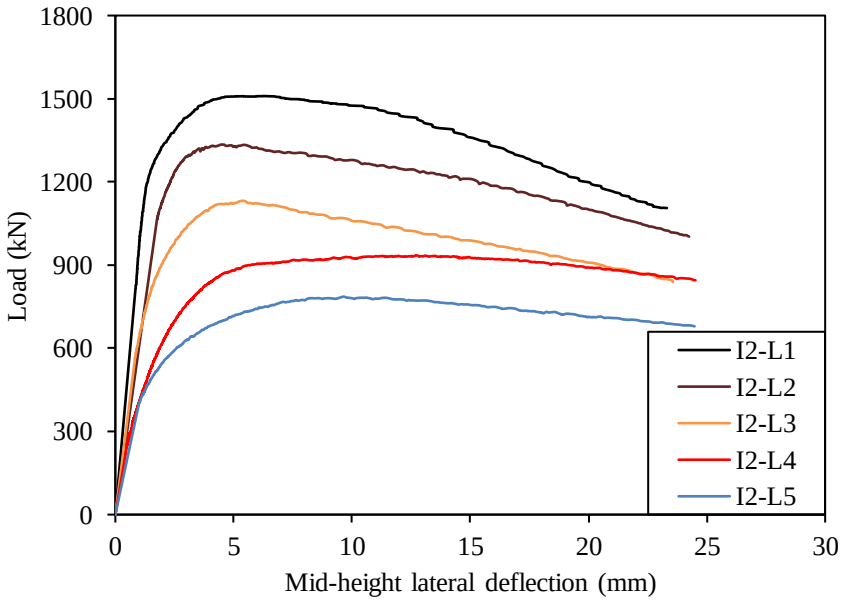

Figure 5.2: Load–mid-height lateral deflection curves for I-150×75×6 column specimens.

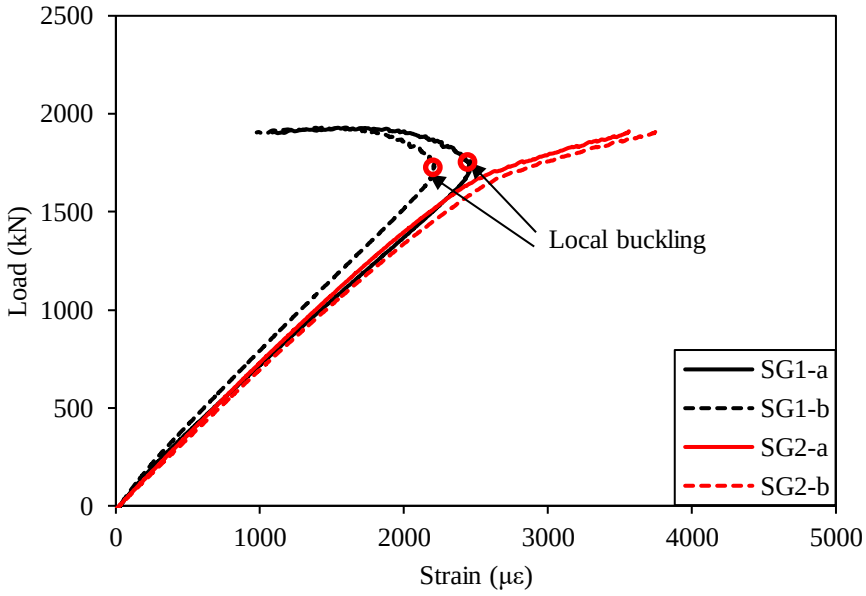

(a) I1-L1

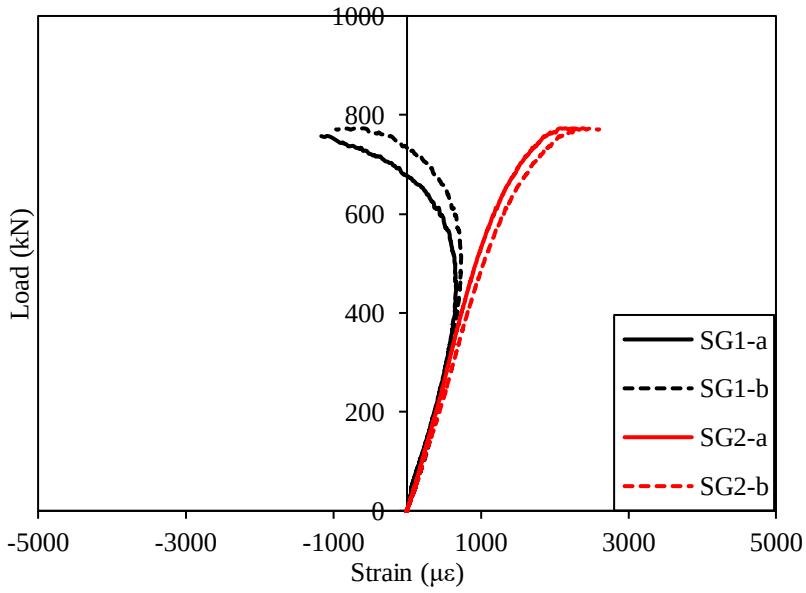

(b) I2-L5

Figure 5.3: Load–mid-height strain curves for typical column specimens.

5.3 Numerical modelling

5.3.1 General

Following the experimental investigation, a numerical modelling programme was performed using the nonlinear finite element (FE) software ABAQUS (2014). FE models were firstly developed and validated against the test data. Upon validation, the FE models were employed to perform parametric studies to generate further numerical data over a wide range of cross-section dimensions and member effective lengths.

5.3.2 Development of FE models

FE models were developed according to the measured cross-section dimensions and member effective lengths, as reported in Table 5.1. The four-node shell element S4R (ABAQUS, 2014) was also employed in the present numerical modelling study. A mesh sensitive study was conducted to seek suitable element sizes that allowed for accurate incorporation of membrane residual stresses into the S960 ultra-high strength steel slender welded I-section column FE models and also led to adequate computational accuracy and efficiency; a series of element sizes ranging from 0.5t to 5t were examined in the mesh sensitive study, and an element size equal to the wall thickness t was finally selected. Regarding the material modelling of grade S960 ultra-high strength steel, the same plastic material model with isotropic hardening, as detailed in Chapter 4, was adopted.

For each S960 ultra-high strength steel slender welded I-section column FE model, the membrane residual stresses, as predicted from the predictive model presented in Chapter 3, were incorporated by the 'Predefined Field' command (ABAQUS, 2014).

Figure 5.4 depicts the membrane residual stress pattern and amplitudes incorporated into the FE model for a typical column specimen I1-L5. For boundary conditions, each end section of the column FE model was coupled to a concentric reference point, with one reference point allowed to translate in the member longitudinal direction and rotate about the cross-section minor principal axis and the other reference point allowed to rotate about the same axis, in order to achieve the pin-ended boundary conditions Regarding the incorporation of initial global and local geometric imperfections into each FE model, an elastic eigenvalue buckling analysis (ABAQUS, 2014) was conducted to obtain the lowest global and local buckling mode shapes, which were adopted as the corresponding initial global and local geometric imperfection patterns (Yuan et al., 2015; Ma et al., 2017; Buchanan et al., 2018; Sun et al., 2020). The measured global and local imperfection magnitude combination of (e_0+ω_g) and ω_0 as well as an additional (generalized) combination of L_e/1000 and t/100 were utilized to factor the derived imperfection patterns. Finally, the modified Riks method (ABAQUS, 2014) was utilised to derive the numerical failure loads, load–mid-height lateral deflection curves and failure modes.

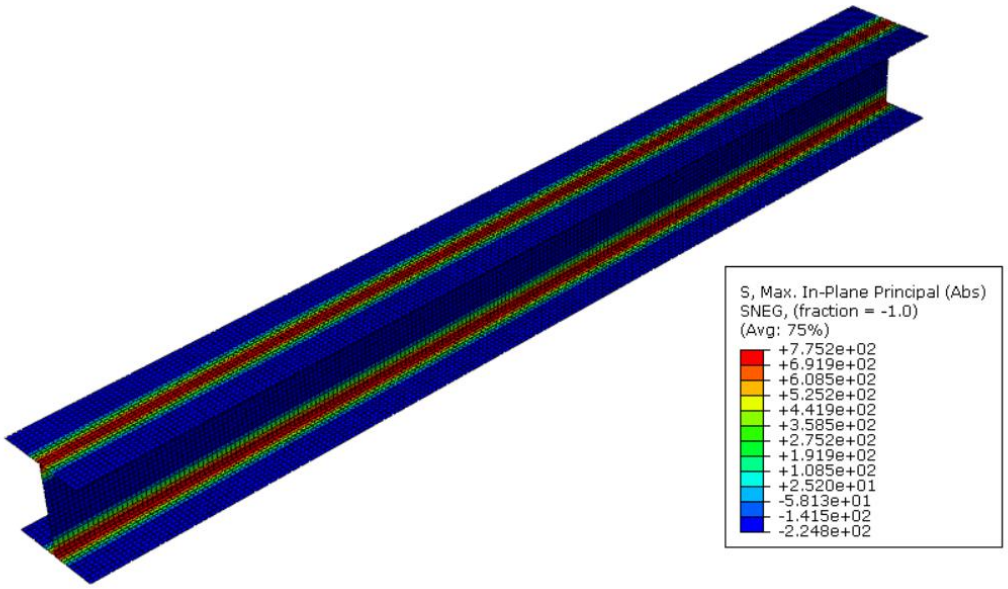

Figure 5.1: Typical membrane residual stress pattern and amplitudes (in MPa) in modelled S960 ultra-high strength steel slender welded I-section column I1-L5 (Positive values indicate tensile residual stresses while negative values indicate compressive residual stresses).

5.3.3 Validation of FE models

Validation of the developed S960 ultra-high strength steel slender welded I-section column FE models was conducted through comparisons of the numerically derived results with their experimental counterparts. Table 5.3 reports the numerical to test failure load ratios for the ten S960 ultra-high strength steel slender welded I-section column specimens, indicating that (i) both initial local and global geometric imperfections can influence the failure loads of S960 ultra-high strength steel slender welded I-section columns and (ii) the accurate and consistent failure load predictions were obtained for the considered initial geometric imperfection combinations. Comparisons between the test and numerical load–mid-height lateral deflection curves for typical S960 ultra-high strength steel slender welded I-section column specimens I1-L3 and I1-L5 are depicted in Figures 5.5 and 5.6, respectively, where the test load–mid-height lateral deflection histories are well captured by their numerical counterparts. The test and numerical failure modes for aforementioned column specimens are displayed in Figures 5.7 and 5.8, respectively, exhibiting excellent agreement. Overall, the developed FE models are capable of simulating the test responses of the S960 ultra-high strength steel slender welded I-section column specimens failing by local–flexural buckling, and therefore deemed to be validated.

Table 5.3: Comparisons of FE failure loads with test failure loads for different global and local geometric imperfection magnitude combinations.

Specimen ID	FE N_u / Test N_u	
	$(e_0+\omega_g)+\omega_0$	$L_e/1000+t/100$
I1-L1	1.013	1.001
I1-L2	0.973	0.962
I1-L3	0.987	0.974
I1-L4	0.984	0.971
I1-L5	1.014	0.999
I2-L1	0.986	0.973
I2-L2	0.974	0.961
I2-L3	1.040	1.024
I2-L4	1.033	1.018
I2-L5	1.030	1.021
Mean	1.003	0.990
COV	0.025	0.025

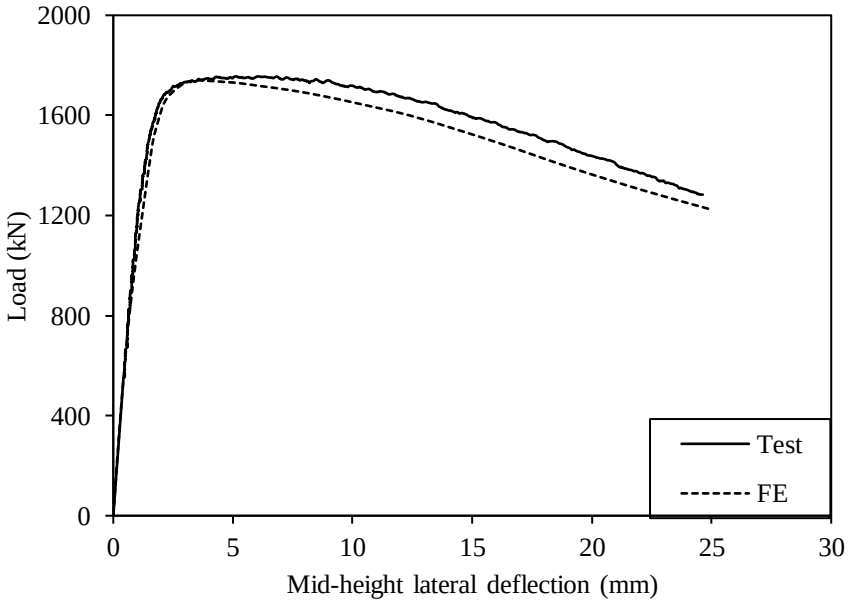

Figure 5.2: Test and numerical load–mid-height lateral deflection curves for S960 ultra-high strength steel slender welded I-section column specimen I1-L3.

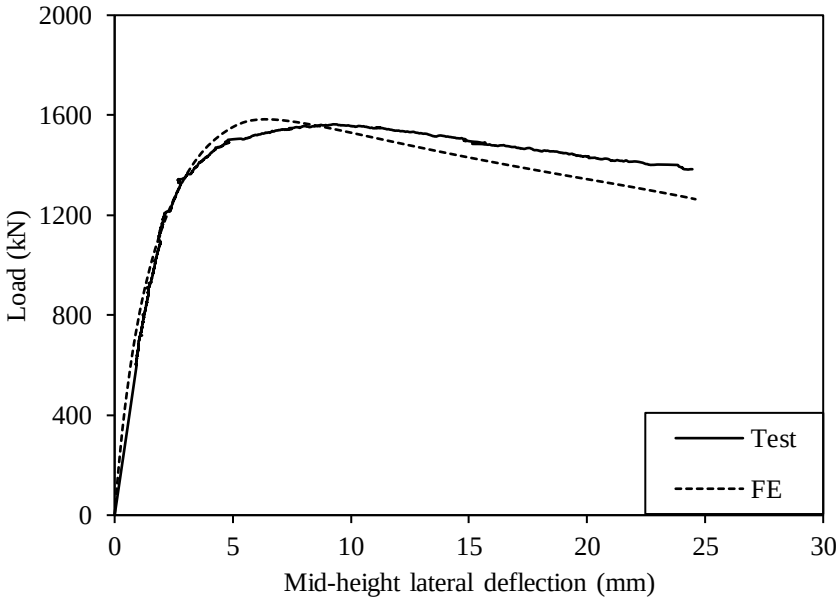

Figure 5.3: Test and numerical load–mid-height lateral deflection curves for S960 ultra-high strength steel slender welded I-section column specimen I1-L5.

Figure 5.4: Test and numerical failure modes for S960 ultra-high strength steel slender welded I-section column specimen I1-L3.

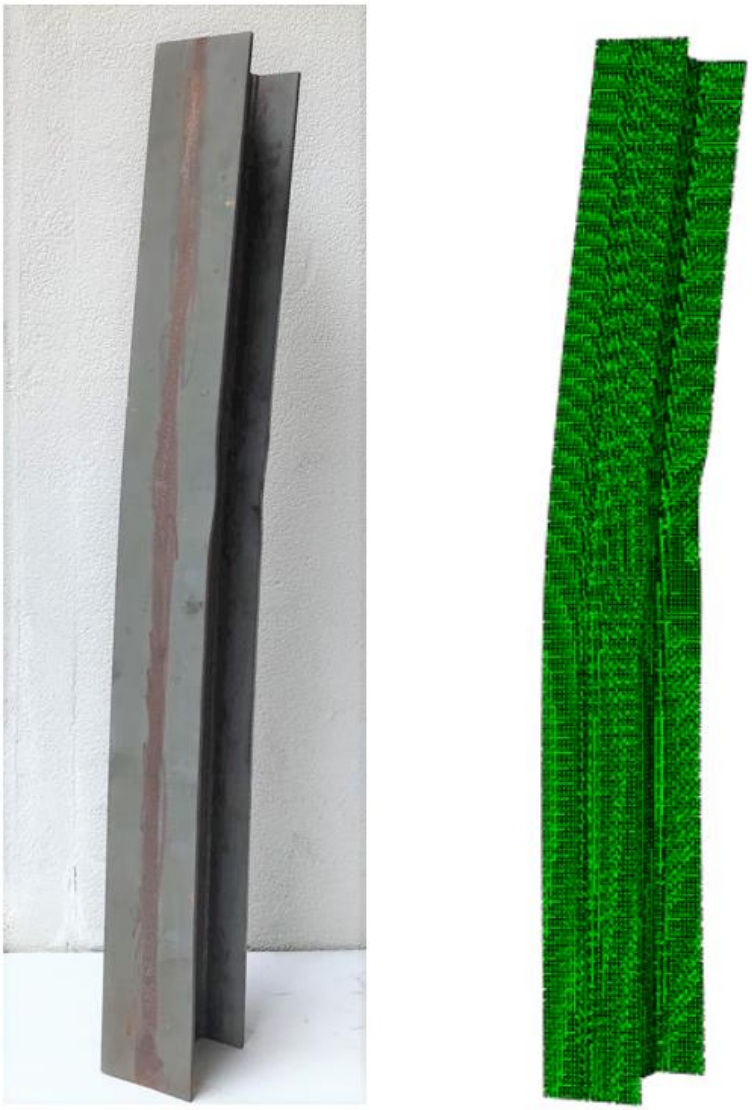

Figure 5.5: Test and numerical failure modes for S960 ultra-high strength steel slender welded I-section column specimen I1-L5.

5.3.4 Parametric studies

The validated FE models were adopted to perform parametric studies to generate further numerical data over a wide range of cross-section dimensions and member effective lengths. The same modelling procedures and techniques as those described in Section 5.3.2 were employed in the present parametric studies. Regarding the modelled cross-section dimensions, the outer heights of the modelled I-sections were

selected as 100 mm and 200 mm, with the flange widths varied between 100 mm and 150 mm in correspondence to the cross-section with the outer height of 200 mm, and flange widths of 75 mm, 87.5 mm and 100 mm selected for cross-section of the outer height of 100 mm, leading to the cross-section aspect ratios from 1.0 to 2.0 being considered. The web and flange thicknesses for each modelled I-section were set to be equal and ranged from 4 mm to 8 mm. All the modelled S960 ultra-high strength steel welded I-sections are classified as Class 4 based on EN 1993-1-12 (CEN, 2007), and also fell in the category of slender cross-sections, as specified in ANSI/AISC 360-16 (AISC, 2016) and AS 4100 (AS, 2016). The effective lengths of the modelled columns were ranged from 290 mm to 2510 mm, leading to different levels of interaction between local and flexural buckling being studied. The global and local geometric imperfection magnitude combination of $L_e/1000$ and $t/100$ was shown to result in accurate predictions of the test failure loads in Chapter 5.3.3, and thus also adopted in the present parametric studies. Overall, a total of 82 numerical data on S960 ultra-high strength steel slender welded I-section columns failing local–flexural buckling have been generated.

5.4 Assessment of current design standards and development of new design approach

5.4.1 General

As mentioned in the previous chapters, the current EN 1993-1-12 (CEN, 2007), ANSI/AISC 360-16 (AISC, 2016) and AS 4100 (AS, 2016) only cover the design of steel structures with nominal material yield stresses less than or equal to 700 MPa (or 690 MPa), and thus current design standards cannot be directly used for the examined S960 ultra-high strength steel slender welded I-section columns. In this section, the

applicability of the codified design rules for S700 (or S690) high strength steel slender welded I-section columns to S960 ultra-high strength steel counterparts was assessed through comparisons of the test and numerical failure loads N_u with the interactive buckling resistance predictions $N_{u,pred}$. The revised design approach based on the European code was also proposed.

5.4.2 EN 1993-1-12 (EC3)

The European code EN 1993-1-12 (CEN, 2007) adopts the buckling curves for the design of column members susceptible to flexural buckling, and the effective width approach, derived from the Winter's plate strength curve, to consider the Class 4 sections prone to local buckling. Regarding slender section columns failing by local–flexural interactive buckling, EN 1993-1-12 (CEN, 2007) combines the use of effective width method and buckling curves to consider the interaction between local and global buckling in the design and the corresponding interactive buckling resistance $N_{u,EC3}$ is calculated from Equation (5.1), as the product of the effective cross-section compression resistance $A_{eff,EC3}f_y$ and the reduction factor χ,

$$N_{u,EC3} = \chi A_{eff,EC3} f_y \tag{5.1}$$

where the calculation method of the effective cross-section area $A_{eff,EC3}$ is same as that described in Section 3.4.3. The reduction factor χ, considering the influence of flexural buckling on the buckling resistance of the column, is determined by Equation (5.2), where $\bar{\lambda}_{EC3}$ is the EC3 member non-dimensional slenderness, as calculated Equation (5.3), and ϕ is a buckling parameter and can be calculated by Equation (5.4), where α is the imperfection factor and determined by the buckling curve; for high strength steel welded or normal strength steel I-section columns susceptible to minor-axis flexural buckling, the design buckling curve 'c' is employed, with α equal

to 0.49.

$$\chi = \frac{1}{\phi + \sqrt{\phi^2 - \bar{\lambda}_{EC3}^2}} \leq 1 \tag{5.2}$$

$$\bar{\lambda}_{EC3} = \sqrt{\frac{A_{eff,EC3} f_y L_e^{\ 2}}{\pi^2 EI}} \tag{5.3}$$

$$\phi = 0.5\left[1 + \alpha\left(\bar{\lambda}_{EC3} - 0.2\right) + \bar{\lambda}_{EC3}^2\right] \tag{5.4}$$

The applicability of the EC3 design rules for S700 high strength steel slender welded I-section columns failing by local–flexural interactive buckling to their S960 ultra-high strength steel counterparts was assessed, based on the comparisons of obtained test and numerical data with the predicted compression resistances from EC3. Figure 5.9 shows the graphical evaluation results, where the obtained experimental and numerical failure loads, normalised by $A_{eff,EC3}f_y$, are plotted against the member non-dimensional slendernesses $\bar{\lambda}_{EC3}$, and all the data points are shown to lie above the currently adopted EC3 design buckling curve 'c'. The test and numerical failure loads were also compared with EC3 predicted failure loads $N_u/N_{u,EC3}$ and displayed in Figure 5.10, where rather conservative results were observed for columns with member non-dimensional slendernesses ranging from 0.7 to 1.3. Table 5.4 reports the quantitative assessment results, where the mean test and numerical to EC3 predicted failure load ratio $N_u/N_{u,EC3}$, is equal to 1.27, with the corresponding COV of 0.07. Both the graphical and quantitative comparisons indicated that EN 1993-1-12 (CEN, 2007) yields safe but conservative compression resistance predictions for pin-ended S960 ultra-high strength steel slender welded I-section columns failing by local–flexural interactive buckling.

Table 5.4: Comparisons of test and numerical failure loads with local–flexural interactive buckling resistance predictions.

No. of test data: 10 No. of FE data: 74	$N_u/N_{u,EC3}$	$N_u/N_{u,AISC}$	$N_u/N_{u,AS}$	$N_u/N_{u,pr}$
Mean	1.27	1.08	1.34	1.08
COV	0.07	0.05	0.08	0.04

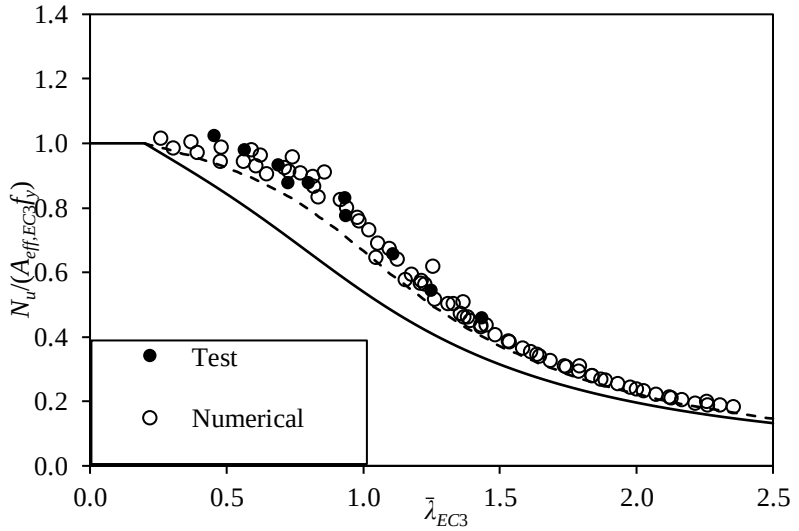

Figure 5.6: Comparisons of test and numerical failure loads with EC3 design buckling curve.

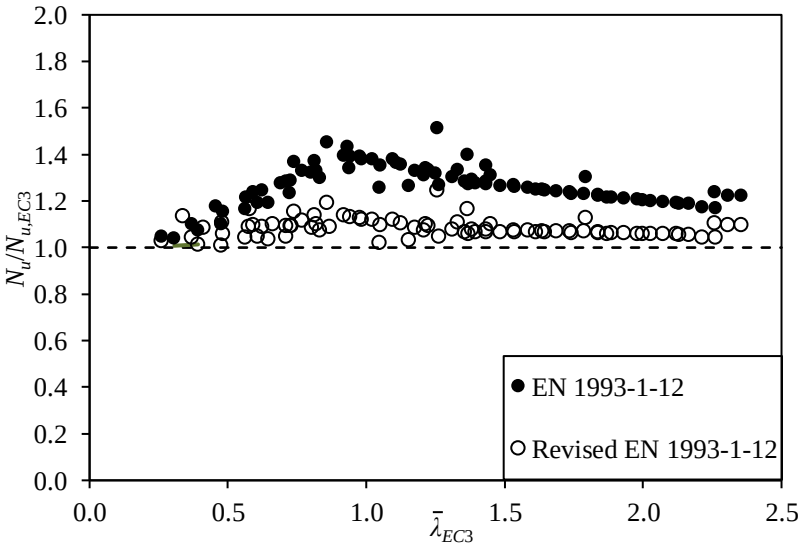

Figure 5.7: Comparisons of test and numerical failure loads with local–flexural buckling resistance predictions from EC3 and revised EC3 design approach.

5.4.3 ANSI/AISC 360-16 (AISC)

The current American specification ANSI/AISC 360-16 (AISC, 2016) provides design rules for both normal and high strength steel structures with material yield stresses up to 690 MPa. The compression resistance for a slender welded I-section column is calculated from Equation (5.5),

$$N_{u,AISC} = F_{cr} A_{eff,AISC} \tag{5.5}$$

where F_{cr} is the critical stress and can be calculated by Equation (5.6), where $\overline{\lambda}_{AISC}$ is the AISC member non-dimensional slenderness, as given by Equation (5.7). The calculation method of the effective cross-section area $A_{eff,AISC}$ is based on the AISC effective width method and detailed in Section 3.4.3.

$$F_{cr} = \begin{cases} 0.658^{\overline{\lambda}_{AISC}^2} f_y & \text{for } \overline{\lambda}_{AISC} \le 1.5 \\ \dfrac{0.877}{\overline{\lambda}_{AISC}^2} f_y & \text{for } \overline{\lambda}_{AISC} > 1.5 \end{cases} \tag{5.6}$$

$$\overline{\lambda}_{AISC} = \sqrt{\frac{A f_y L_e^{\,2}}{\pi^2 EI}} \tag{5.7}$$

Graphical and quantitative assessments of the applicability of the AISC design rules to S960 ultra-high strength steel slender welded I-section columns were performed through comparisons of the test and numerical failure loads with the compression resistance predictions of AISC 360 (AISC, 2016). The AISC design buckling curve, as plotted in Figure 5.11, was generally shown to well capture the test and numerical data points over the whole considered range of member non-dimensional slenderness, though a small disparity existed for member non-dimensional slendernesses ranging from 0.7 to 1.1. This is also evident in Figure 5.12, where the test and numerical failure loads were compared with the AISC compression resistance predictions. The quantitative assessments are also carried out, with results reported in Table 5.4, in

which the mean ratio of $N_u/N_{u,AISC}$ is equal to 1.08, with the corresponding COV of 0.05. Overall, the AISC design rules were generally found to yield an overall good level of design accuracy when used for S960 ultra-high strength steel slender welded I-section columns failing by local–flexural interactive buckling.

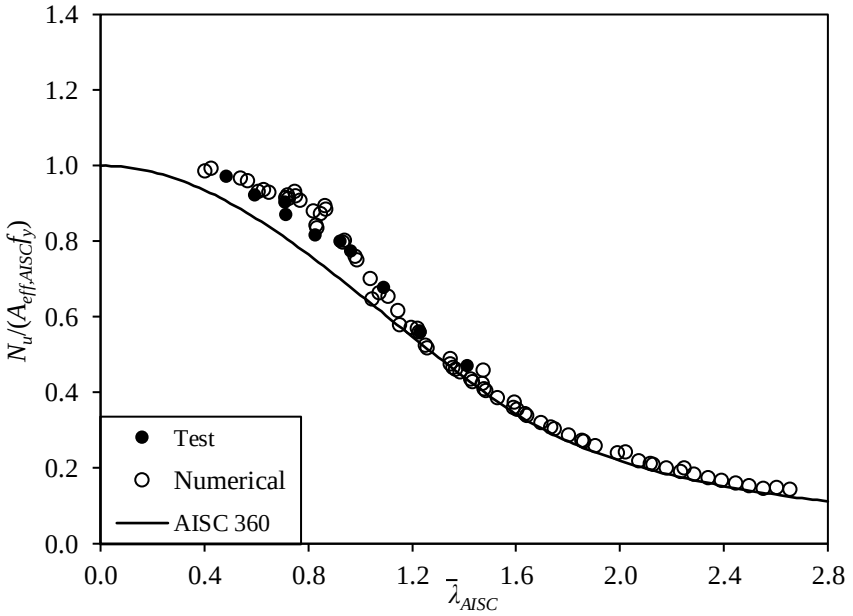

Figure 5.8: Comparisons of test and numerical failure loads with AISC design buckling curve.

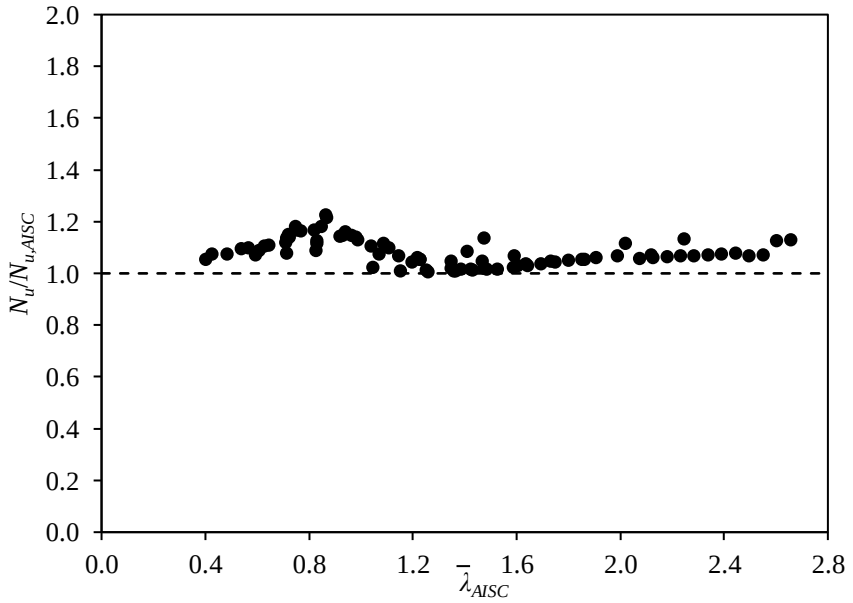

Figure 5.9: Comparisons of test and numerical failure loads with local–flexural buckling resistance predictions from ANSI/AISC 360-16 (AISC, 2016).

5.4.4 AS 4100 (AS)

The Australian standard AS 4100 (AS, 2016) prescribes the design compression resistance $N_{u,AS}$ for slender welded I-section columns failing by local–flexural interactive buckling, as the product of the reduction factor α_c multiplied by the effective cross-section compression load $A_{eff}f_y$, as given in Equation (5.8),

$$N_{u,AS} = \alpha_c A_{eff,AS} f_y \tag{5.8}$$

where the effective cross-section area of the slender I-section $A_{eff,AS}$ is calculated based on the AS effective width method, as detailed in Section 3.4.3, and the flexural buckling reduction factor α_c, as defined by the AS design buckling curve, is given by Equation (5.9), where λ_n is the modified member slenderness and can be calculated from Equation (5.10), where $\bar{\lambda}_{AS}$ is the AS member non-dimensional slenderness, as defined in Equation (5.11), α_a is the compression member factor, as given by Equation (5.12), α_b is the member section constant and equal to 0.5 for I-sections fabricated from hot-rolled sheets, and ξ is a buckling parameter and can be determined from Equation (5.13), where η is the compression member imperfection factor, as given by Equation (5.14).

$$\alpha_c = \xi\left[1-\sqrt{1-\left[\frac{90}{\xi\left(\lambda_n+\alpha_a\alpha_b\right)}\right]^2}\right] \le 1 \tag{5.9}$$

$$\lambda_n = \sqrt{\frac{\pi^2 E}{250}}\bar{\lambda}_{AS} \tag{5.10}$$

$$\bar{\lambda}_{AS} = \sqrt{\frac{A_{eff,AS} f_y L_e^{\,2}}{\pi^2 EI}} \tag{5.11}$$

$$\alpha_a = \frac{2100\left(\lambda_n - 13.5\right)}{\lambda_n^2 - 15.3\lambda_n + 2050} \tag{5.12}$$

$$\xi = \frac{\left(\frac{\lambda_n + \alpha_a \alpha_b}{90}\right)^2 + 1 + \eta}{2\left(\frac{\lambda_n + \alpha_a \alpha_b}{90}\right)^2} \tag{5.13}$$

$$\eta = 0.00326\left(\lambda_n + \alpha_a \alpha_b - 13.5\right) \geq 0 \tag{5.14}$$

The applicability of the AS design rules for high strength steel slender welded I-section columns failing by local–flexural buckling to S960 ultra-high strength steel counterparts was assessed based on the test and numerical failure loads. The mean test and numerical to AS predicted failure load ratio $N_u/N_{u,AS}$ and the corresponding COV, as reported in Table 5.4, are equal to 1.34 and 0.08, respectively, indicating a high level of design conservatism. This conservatism is also evident in Figures 5.13 and 5.14. Overall, the compression resistances of S960 ultra-high strength steel slender welded I-section columns are unduly estimated by AS 4100 (AS, 2016).

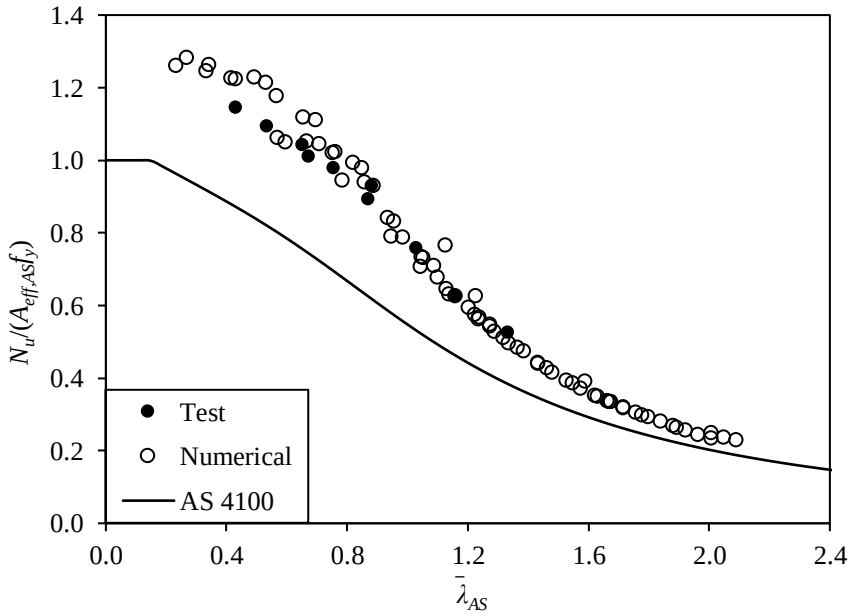

Figure 5.10: Comparisons of test and numerical failure loads with AS design buckling curve.

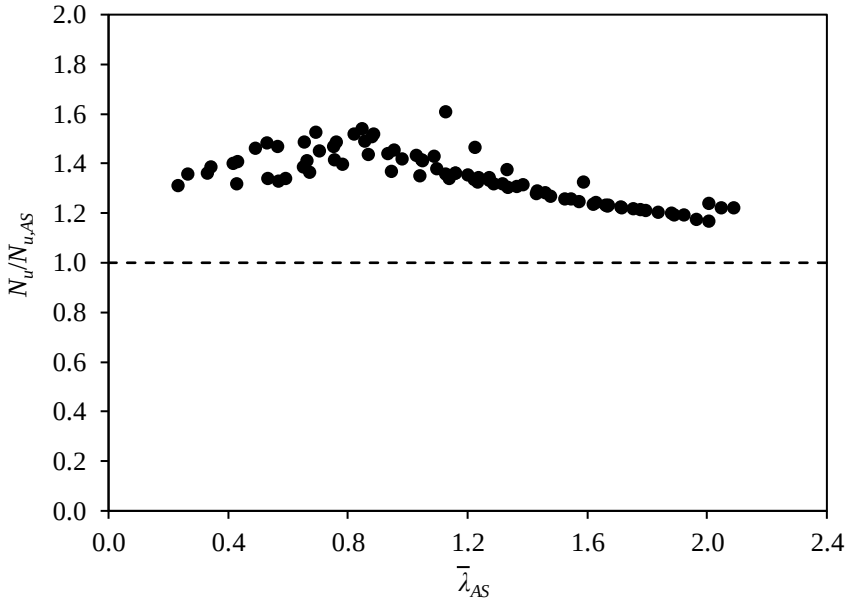

Figure 5.11: Comparisons of test and numerical failure loads with local–flexural buckling resistance predictions from AS 4100 (AS, 2016).

5.4.5 New design proposal

As discussed before, the conservatism of the Eurocode design rules can be attributed to adoption of the conservative buckling curve 'c'. From Chapter 4, it can be concluded that the buckling curve 'a' with α equal to 0.21 leads to better design accuracy for S960 ultra-high strength steel non-slender welded I-section columns prone to global buckling. Therefore, a revised Eurocode design approach is proposed herein by utilizing the original Eurocode effective width approach combined with the buckling curve 'a'. Comparisons of the buckling curves with the normalized numerical and test ultimate loads (by $A_{eff,EC3}f_y$) are presented in Figure 5.9, evidencing that the buckling curve 'a' can well capture the derived data points. The graphical assessment of the resistance predictions from the revised Eurocode design approach $N_{u,pr}$ is also displayed in Figure 5.10, whilst the quantitative assessment results are summarized in Table 5.4, with the mean test and numerical to predicted ultimate load ratio $N_u/N_{u,pr}$ equal to 1.08 and the COV of 0.04. It can therefore be concluded that the revised Eurocode design approach can lead to more accurate and consistent

interactive buckling resistances than the original Eurocode design approach when used for S960 ultra-high strength steel slender welded I-section columns.

5.5 Concluding remarks

An extensive experimental and numerical investigation has been conducted to study the local–flexural interactive buckling behaviour and resistances of S960 ultra-high strength steel slender welded I-section columns. The experimental investigation was firstly conducted on two slender I-sections, and included initial global and local geometric imperfection measurements and ten pin-ended column tests. A numerical study was then carried out; FE models were initially developed and afterwards employed to perform parametric studies to generate further numerical data over a wide range of cross-section dimensions and member effective lengths. The obtained test and numerical results were adopted to assess the applicability of the relevant design rules for S700 (or S690) high strength steel slender welded I-section columns failing by local–flexural interactive buckling, as set out in EN 1993-1-12 (CEN, 2007), ANSI/AISC 360-16 (AISC, 2016) and AS 4100 (AS, 2016), to their S960 ultra-high strength steel counterparts. The results of the graphical and quantitative assessments revealed that both EN 1993-1-12 (CEN, 2007) and AS 4100 (AS, 2016) yield a high degree of conservatism for predicting local–flexural interactive buckling resistances for S960 ultra-high strength steel slender welded I-section columns, while ANSI/AISC 360-16 (AISC, 2016) results in overall accurate and consistent resistance predictions, though the predicted resistances are marginally conservative for the S960 ultra-high strength steel slender welded I-section columns with member non-dimensional slendernesses from 0.7 to 1.1. Finally, a revised design approach (i.e. the EC3 design buckling curve ‘a’ combined with the EC3 effective width expressions) was proposed, and shown to result in a much higher level of design accuracy and consistency for S960 ultra-high strength steel slender welded I-section columns failing by local–flexural interactive buckling.

CHAPTER 6

LOCAL BUCKLING OF S960 ULTRA-HIGH STRENGTH STEEL WELDED I-SECTION STUB COLUMNS UNDER COMBINED LOADING

6.1 Introduction

The previous chapters respectively investigated the local buckling, flexural buckling and flexural–local interactive buckling behaviour of S960 ultra-high strength steel welded I-sections under isolated loading (i.e. axial compression), while the local stability and cross-section resistances of S960 ultra-high strength steel welded I-section stub columns under combined loading were studied in this chapter, through the experimental and numerical investigations. An experimental programme, adopting two welded I-sections – I-120×120×6 and I-150×75×6, was firstly conducted, including ten minor-axis and ten major-axis eccentric compression tests as well as initial local geometric imperfection measurements. A numerical modelling programme was then performed, where finite element models were firstly developed and validated against the test results and then employed to perform parametric studies to generate further numerical data over a wide range of cross-section dimensions and loading combinations. On the basis of the test and numerical data, the applicability of the design interaction curves for S700 (or S690) high strength steel welded I-sections under minor-axis and major-axis combined loading, as set out in the European code, American specification and Australian standard, to their S960 ultra-high strength steel counterparts was evaluated. The evaluation results for S960 ultra-high strength steel welded I-section stub columns under minor-axis combined loading

and major-axis combined loading have respectively been reported in Su et al. (2021c) and Su et al. (2021d).

6.2 Testing

6.2.1 General

Given that there have been no tests on S960 ultra-high strength steel welded I-sections under combined loading, an experimental programme was firstly carried out to generate a data pool. The experimental programme employed two I-sections: I-120×120×6 and I-150×75×6, both of which were fabricated the same batch of 6 mm thick S960 ultra-high strength steel plates by robotic gas metal arc welding. The chemical compositions, nominal material properties of grade S960 ultra-high strength steel and used electrode for welding were described in Chapter 3. The cross-section labelling system starts with a letter 'I' (indicating an I-section), followed by the nominal section size in millimetres (outer section depth h × flange width b_f × wall thickness t – see Figures 6.1 and 6.2). Both of the two adopted I-sections were classified as slender cross-sections according to the slenderness limits in EN 1993-1-12 (CEN, 2007), ANSI/AISC 360-16 (AISC, 2016) and AS 4100 (AS, 2016). For each I-section, five stub column specimens with the same nominal length L were prepared and tested under minor-axis combined loading and another five were tested under major-axis combined loading; it is worth noting that the nominal specimen length was set to be equal to three times the mean outer cross-section dimensions (Ziemian, 2010), which is deemed short enough to avoid flexural buckling, but still long enough to contain a representative pattern of local geometric imperfections and membrane residual stresses. Tables 6.1 and 6.2 respectively report the key measured geometric dimensions of the stub column specimens under minor-axis and major-axis combined loading. The specimen ID consists of a letter – 'A' (or 'C') and 'B' (or 'D')

signifying I-120×120×6 and I-150×75×6, respectively) and a number (for differentiating the specimens with the same nominal geometric dimensions but different initial loading eccentricities about minor principal axis or major principal axis). The overall experimental programme included initial local geometric imperfection measurements, ten minor-axis eccentric compression tests and ten major-axis eccentric compression tests.

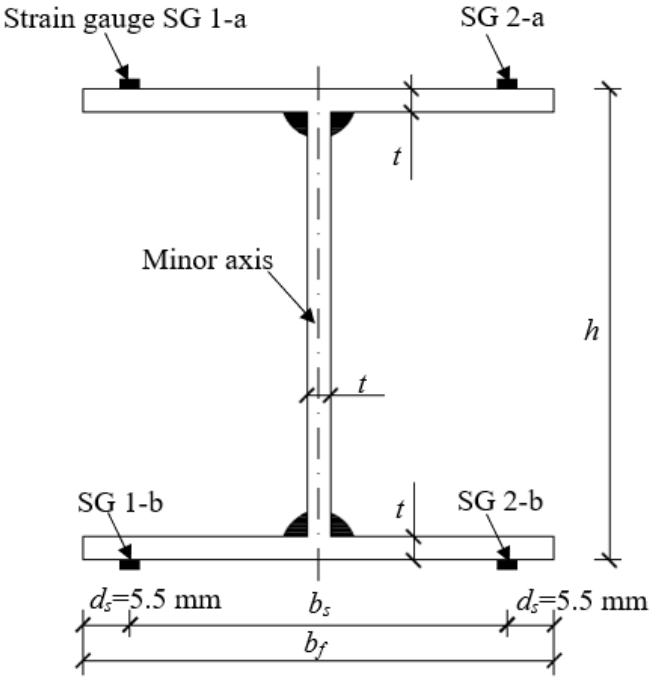

Figure 6.1: Notations of welded I-section and locations of strain gauges for minor-axis combined loading.

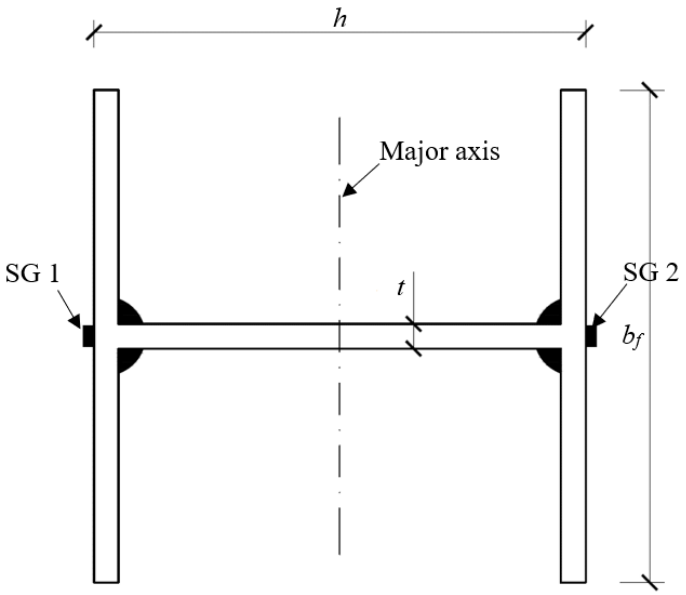

Figure 6.2: Notations of welded I-section and locations of strain gauges for major-axis combined loading.

Table 6.1: Measured geometric dimensions and initial local geometric imperfections of S960 ultra-high strength steel welded I-section stub column specimens under minor-axis combined loading.

Cross-section	Specimen ID	L (mm)	h (mm)	b_f (mm)	t (mm)	ω_0 (mm)
I-120×120×6	A1	359	119.36	119.24	5.98	0.07
	A2	360	119.28	119.27	5.98	0.06
	A3	359	119.89	119.92	6.03	0.06
	A4	358	119.64	119.52	5.99	0.09
	A5	360	119.86	119.67	6.06	0.11
I-150×75×6	B1	320	150.25	74.93	6.03	0.07
	B2	319	150.20	74.73	6.04	0.09
	B3	319	150.01	74.68	6.01	0.09
	B4	318	150.12	74.49	6.02	0.08
	B5	320	149.52	74.42	5.99	0.07

Table 6.2: Measured geometric dimensions and initial local geometric imperfections of S960 ultra-high strength steel welded I-section stub column specimens under major-axis combined loading.

Cross-section	Specimen ID	L (mm)	h (mm)	b_f (mm)	t (mm)	ω_0 (mm)
I-120×120×6	C1	359	119.45	119.52	5.98	0.07
	C2	361	119.32	119.47	5.97	0.08
	C3	358	119.52	119.98	6.04	0.07
	C4	359	119.79	119.74	5.98	0.06
	C5	360	119.94	119.28	6.06	0.06
I-150×75×6	D1	319	150.15	74.96	6.04	0.07
	D2	321	150.08	74.48	6.04	0.07
	D3	319	149.96	74.62	6.02	0.06
	D4	319	150.18	74.67	6.02	0.07
	D5	320	149.76	74.54	5.99	0.07

6.2.2 Initial local geometric imperfection measurements and eccentric compression tests

The structural behaviour and resistances of metallic thin-walled section components are affected by their initial geometric imperfections. The initial local geometric imperfections of the S960 ultra-high strength steel welded I-section stub column specimens were thus measured, with the method and setup same as that utilised in Chapter 3. The initial local geometric imperfection magnitude of the stub column specimen ω_0, is reported in Table 6.2, with the measured initial local geometric imperfection distributions for a typical column specimen are depicted in Figure 6.3.

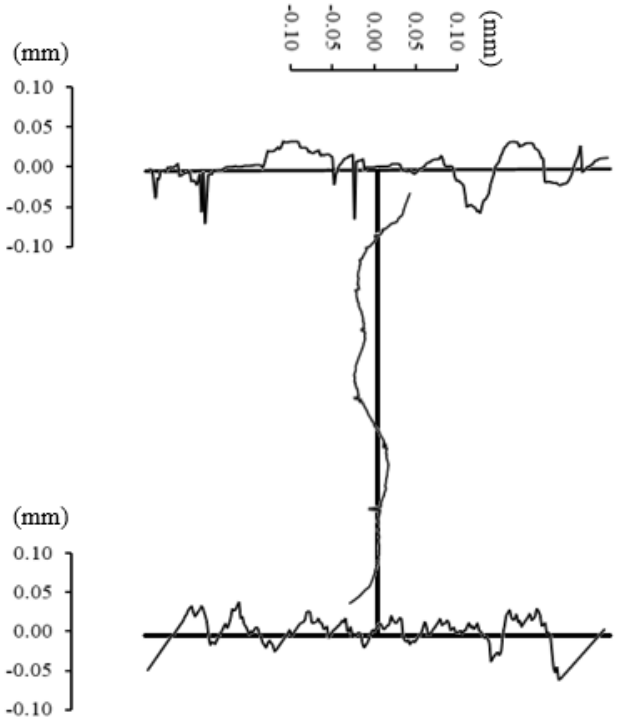

Figure 6.3: Measured initial local geometrical imperfection distributions for specimen A1.

Eccentric compression tests were conducted on twenty S960 ultra-high strength steel welded I-section stub column specimens, with ten for major-axis and ten for minor-axis combined loading, to investigate their cross-section behaviour and resistances under combined compression and bending moment. The initial loading eccentricities were varied from 15 mm to 100 mm, resulting in a range of combinations of compression load and bending moment being considered. An INSTRON 5000 kN servo-hydraulic testing machine was employed to conduct all the eccentric compression tests at a loading rate of 0.3 mm/min. Each end of the testing machine was equipped with a knife-edge device, offering pin-ended boundary conditions to the specimen ends. The knife-edge device, as shown in Figure 6.4, consists of a pit plate with a semi-circular groove and a wedge plate with a knife-edge wedge. Prior to testing, each stub column specimen welded with 15 mm thick end plates was placed

between the top and bottom wedge plates, and their relative position was carefully adjusted by means of a laser and two spirit levels, to ensure the appropriate member alignment and pre-specified initial loading eccentricity. Upon completion of the member alignment and position adjustment, the specimen was anchored by bolting the end plates to the wedge plates.

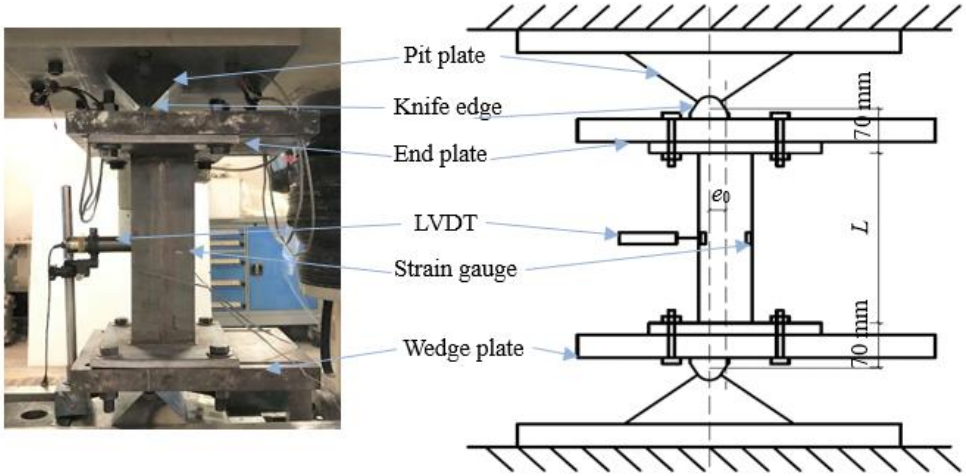

(a) Minor-axis combined loading.

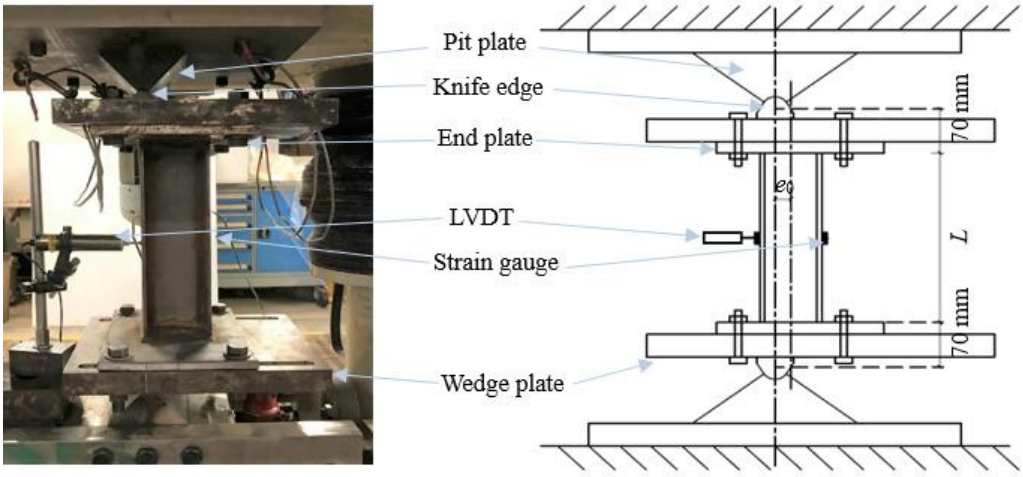

(b) Major-axis combined loading.

Figure 6.4: Eccentric compression test setups.

The instrumentation used for the minor-axis eccentric compression tests is depicted in Figure 6.4(a), including one LVDT attached to the mid-height of the specimen to measure the lateral deflection about the minor principal axis and two pairs of strain gauges affixed to the two flanges at mid-height (with the detailed locations shown in Figure 6.1) to measure the longitudinal strains at these locations. A similar setup was used for the major-axis eccentric compression tests, as shown in Figure 6.4(b), but with one LVDT attached to the mid-height of the flange and two pairs of strain gauges attached to the flanges at mid-height – see Figure 6.2. The readings from the LVDT and strain gauges were adopted to determine the actual initial loading eccentricity e_0 of each eccentrically loaded stub column specimen, according to Equation (6.1) (Zhao et al., 2015; Sun et al., 2021), where N is the applied eccentric compression load, I is the second moment of area about the minor principal axis, ε_{max}–ε_{min} is the difference of the longitudinal strains measured by the two pairs of strain gauges, D is the distance between the two pairs of strain gauges ($D=b_s$ for the combined loading tests about the minor principal axis – see Figure 6.1, while $D=h$ for the combined loading tests about the major principal axis – see Figure 6.2) and Δ is the mid-height lateral deflection recorded by the LVDT. Note that Equation (6.1) was derived by assuming that the structural behaviour was close to linear elastic, and it was thus recommended that no more than 15% of the predicted failure loads be used in the calculation of the actual initial loading eccentricity e_0 (Zhao et al., 2015; Sun et al., 2021).

$$e_0 = \frac{EI\left(\varepsilon_{max} - \varepsilon_{min}\right)}{ND} - \Delta \tag{6.1}$$

The load–deflection curves measured for the two series of S960 ultra-high strength steel welded I-section stub column specimens under minor-axis and major-axis compression tests are shown in Figures 6.5 and 6.6, respectively, while the key obtained test results are reported in Tables 6.3 and 6.4, including the actual initial

loading eccentricity e_0, the failure load N_u, the mid-height lateral deflection at the failure load Δ_u and the failure moment $M_u=N_u(e_0+\Delta_u)$ at the specimen mid-height. Upon testing, all the ten eccentrically loaded S960 ultra-high strength steel welded I-section stub column specimen were observed to fail by local buckling, with the deformed failure modes for S960 ultra-high strength steel welded I-section stub columns under minor-axis eccentric compression and major-axis eccentric compression displayed in Figures 6.7 and 6.8, respectively.

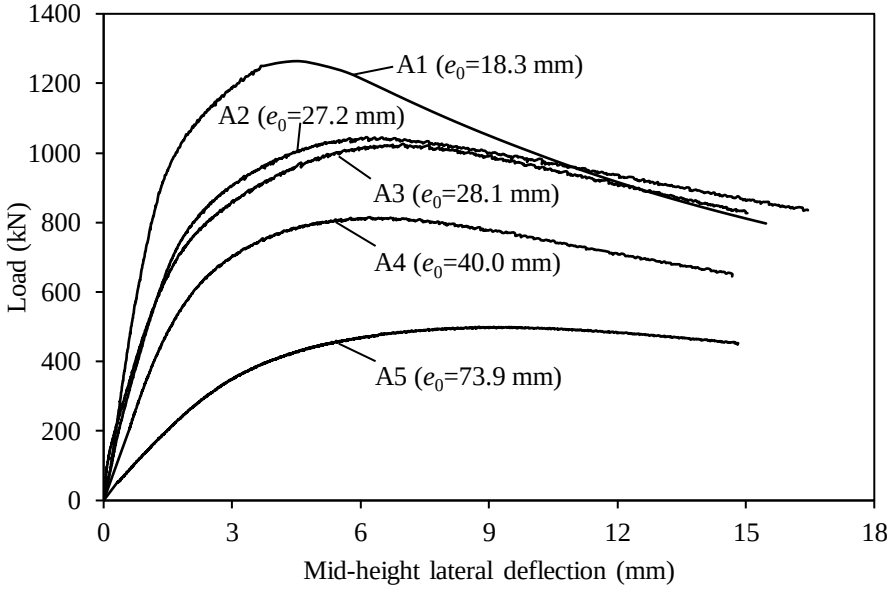

(a) I-120×120×6 specimens.

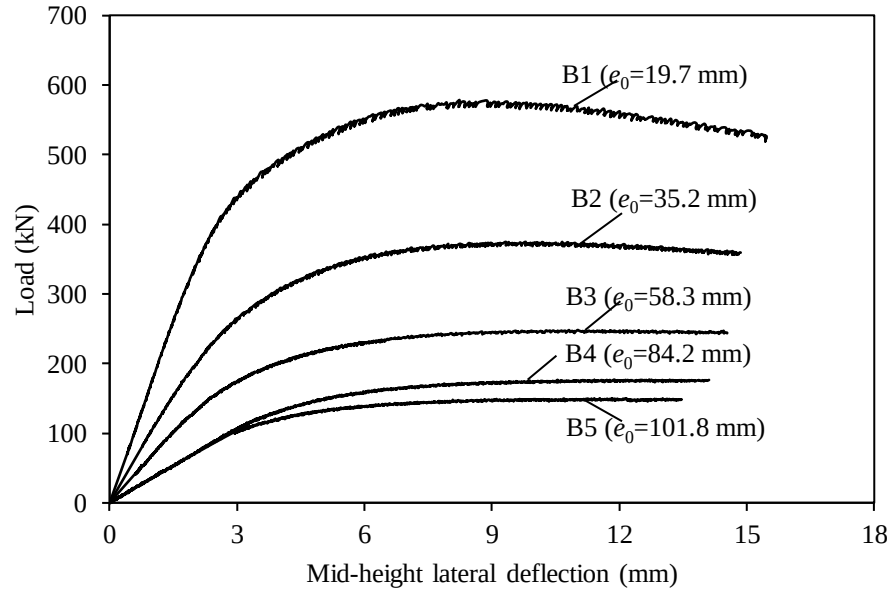

(b) I-150×75×6 specimens.

Figure 6.5: Load–lateral deflection curves for minor-axis compression tests on S960 ultra-high strength steel welded I-section stub column specimens.

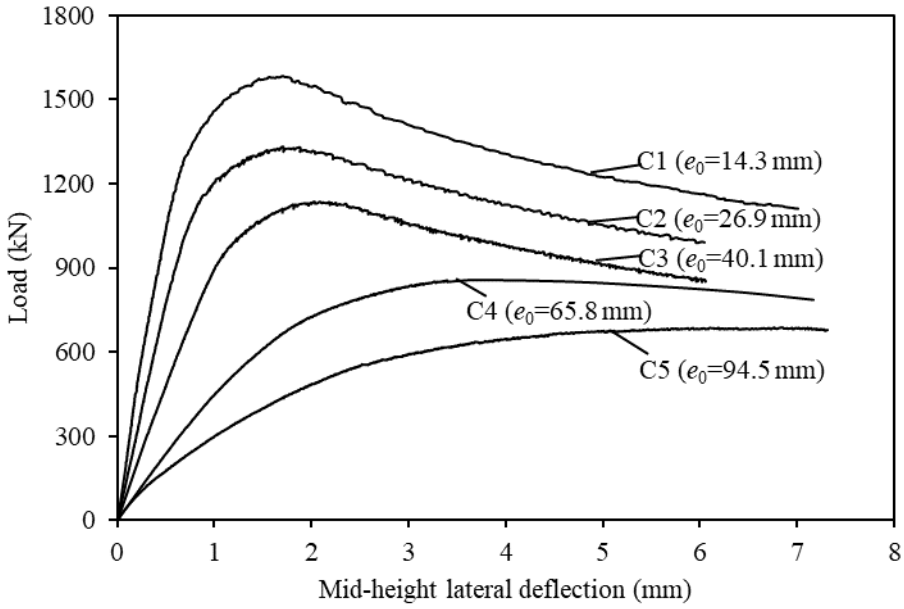

(a) I-120×120×6 specimens.

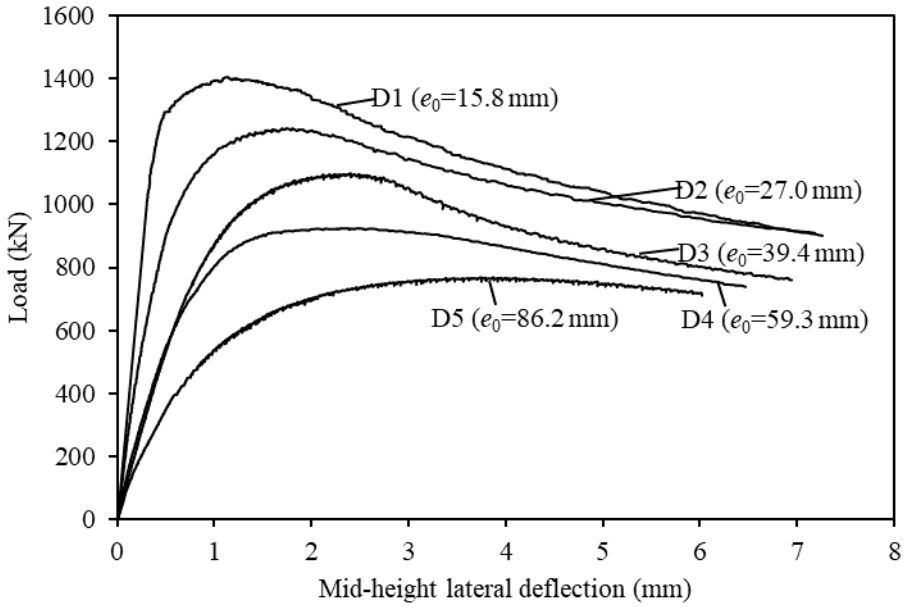

(b) I-150×75×6 specimens.

Figure 6.6: Load–lateral deflection curves for major-axis compression tests on S960 ultra-high strength steel welded I-section stub column specimens.

Table 6.3: Key minor-axis eccentric compression test results.

Cross-section	Specimen ID	e_0 (mm)	N_u (kN)	Δ_u (mm)	M_u (kNm)
I-120×120×6	A1	18.3	1263.5	4.7	29.1
	A2	27.2	1045.0	6.1	34.8
	A3	28.1	1026.1	7.0	36.0
	A4	40.0	815.1	6.2	37.7
	A5	73.9	499.6	9.1	41.5
I-150×75×6	B1	19.7	578.4	8.2	16.2
	B2	35.2	374.6	10.7	17.2
	B3	58.3	248.1	11.0	17.2
	B4	84.2	177.2	15.6	17.7
	B5	101.8	150.2	12.5	17.2

Table 6.4: Key test results for major-axis eccentric compression tests.

Cross-section	Specimen ID	e_0 (mm)	N_u (kN)	Δ_u (mm)	M_u (kNm)
I-120×120×6	C1	14.3	1586.4	1.7	25.4
	C2	26.9	1331.1	1.7	38.1
	C3	40.1	1137.6	2.0	47.9
	C4	65.8	855.7	3.7	59.5
	C5	94.5	689.0	6.8	69.8
I-150×75×6	D1	15.8	1404.0	1.1	23.8
	D2	27.0	1243.3	1.7	35.7
	D3	39.4	1097.7	2.4	45.9
	D4	59.3	923.7	2.3	56.9
	D5	86.2	768.2	3.7	69.1

(a) I-120×120×6 specimens (from left to right: A1, A2, A3, A4 and A5).

(b) I-150×75×6 specimens (from left to right: B1, B2, B3, B4 and B5).

Figure 6.7: Failure modes of S960 ultra-high strength steel welded I-section stub column specimens under minor-axis eccentric compression.

(a) Typical I-120×120×6 specimens (from left to right: C1, C3 and C5)

(b) Typical I-150×75×6 specimens (from left to right: D1, D3 and D5)

Figure 6.8: Failure modes of S960 ultra-high strength steel welded I-section stub column specimens under major-axis eccentric compression.

6.3 Numerical modelling

6.3.1 General

In conjunction with the experimental programme, a numerical modelling programme was conducted using the nonlinear finite element (FE) software ABAQUS (2014). FE models are firstly developed, with the detailed modelling techniques and procedures described. It is accompanied by a validation study, where the developed FE models are validated against the test results. Finally, the validated FE models are used to perform parametric studies, to generate further numerical data over a wide range of cross-section dimensions and loading combinations.

6.3.2 Development of FE models

The shell element S4R (ABAQUS, 2014), with its size equal to the wall thickness t was employed herein. In terms of material modelling of S960 ultra-high strength steel, incorporation of membrane residual stresses and inclusion of initial geometric imperfections, the procedures and techniques were same as those detailed in Section 4.3.2. Four imperfection magnitudes, including the measured value ω_0 and three generalised values – $t/100$, $t/30$ and $t/10$, were adopted to factor the derived distribution pattern, enabling the influence of imperfections on the structural behaviour of S960 ultra-high strength steel welded I-sections under combined loading to be investigated.

The pin-ended boundary conditions used in the tests were carefully modelled. Specifically, for each FE model, its top end section was coupled to a reference point, which was allowed to translate in the longitudinal direction and rotate about the axis of combined loading, while its bottom end section was also coupled to a reference

point, which was only allowed to rotate about the same axis. Each of the two reference points was eccentrically located to the axis of combined loading at a distance equal to e_0 and also offset longitudinally from the end section by 70 mm – the distance from the rotation centre of the knife-edge device to the end of the specimen in the tests (see Figure 6.4). Finally, static Riks analyses (ABAQUS, 2014), considering material and geometric nonlinearities, were conducted on the developed FE models, to obtain the numerical failure loads, load–deflection curves and failure modes.

6.3.3 Validation of FE models

The accuracy of the developed FE models was assessed by comparing the obtained numerical results against their experimental counterparts. Tables 6.5 and 6.6 respectively report the numerical to test failure load ratios for S960 ultra-high strength steel welded I-section stub column specimens under minor-axis and major-axis combined loading, with the results indicating that (i) the test failure loads are generally well predicted for all the four considered initial local geometric imperfection magnitudes and (ii) the best agreement is achieved when the initial local geometric imperfection magnitude is taken as $t/100$. The test and numerical load–deflection curves for two typical groups of specimens A4, B1 and C2, D2 are displayed in Figures 6.9 and 6.10, respectively, where the test curves are accurately replicated by their numerical counterparts. Comparisons between the test and numerical failure modes are presented in Figures 6.11 and 6.12, showing excellent agreement. In summary, the developed FE models can accurately simulate the test structural responses of S960 ultra-high strength steel welded I-sections under combined compression and bending moment, and were thus deemed to be validated.

Table 6.5: Comparisons between test and numerical failure loads for different initial local geometric imperfection magnitudes of S960 ultra-high strength steel welded I-sections under minor-axis combined loading.

Cross-section	Specimen ID	FE N_u / Test N_u			
		ω_0	t/100	t/30	t/10
I-120×120×6	A1	0.994	0.998	0.964	0.931
	A2	0.997	0.997	0.963	0.928
	A3	0.996	0.996	0.964	0.928
	A4	0.987	0.996	0.964	0.925
	A5	0.986	0.998	0.975	0.940
I-150×75×6	B1	1.000	1.000	1.000	0.999
	B2	0.999	1.000	0.999	0.997
	B3	0.990	0.990	0.990	0.988
	B4	1.004	1.004	1.004	1.001
	B5	1.000	1.000	1.000	0.997
	Mean	0.996	0.998	0.982	0.963
	COV	0.006	0.004	0.018	0.036

Table 6.6: Comparisons between test and numerical failure loads for different initial local geometric imperfection magnitudes of S960 ultra-high strength steel welded I-sections under major-axis combined loading.

Cross-section	Specimen ID	FE N_u / Test N_u			
		ω_0	t/100	t/30	t/10
I-120×120×6	C1	0.996	1.001	0.984	0.951
	C2	0.989	0.989	0.974	0.942
	C3	0.979	0.979	0.964	0.934
	C4	1.003	1.005	0.989	0.959
	C5	0.987	0.997	0.980	0.951
I-150×75×6	D1	0.999	1.000	0.995	0.957
	D2	0.991	0.995	0.979	0.945
	D3	0.991	0.998	0.978	0.942
	D4	0.996	1.002	0.979	0.943
	D5	0.993	0.996	0.972	0.933
	Mean	0.992	0.996	0.979	0.946
	COV	0.007	0.008	0.009	0.009

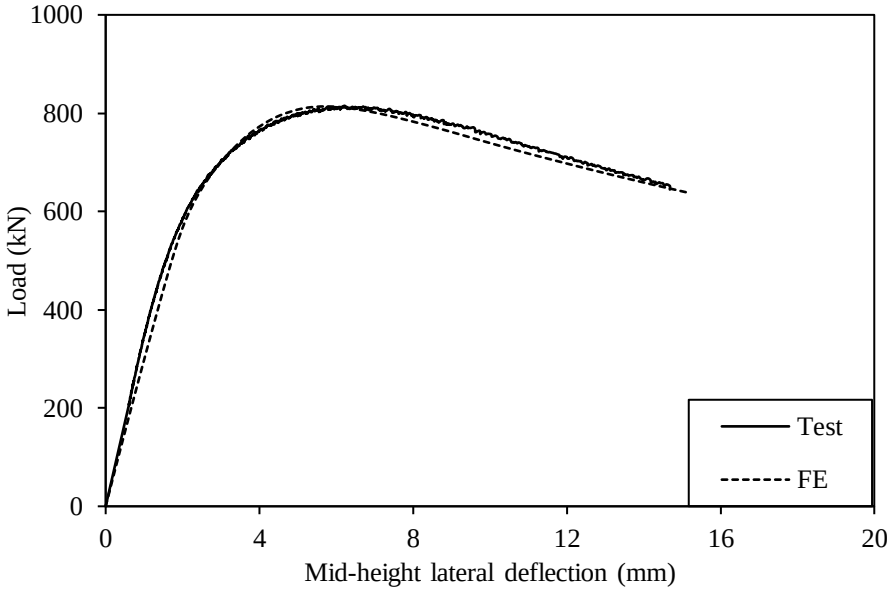

(a) Specimen A4

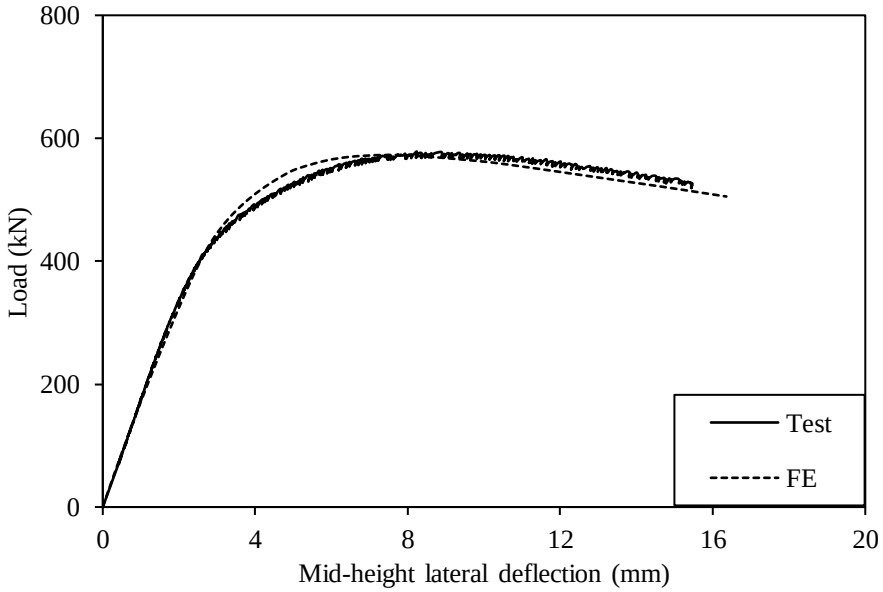

(b) Specimen B1

Figure 6.9: Test and numerical load–lateral deflection curves of S960 ultra-high strength steel welded I-sections under minor-axis combined loading.

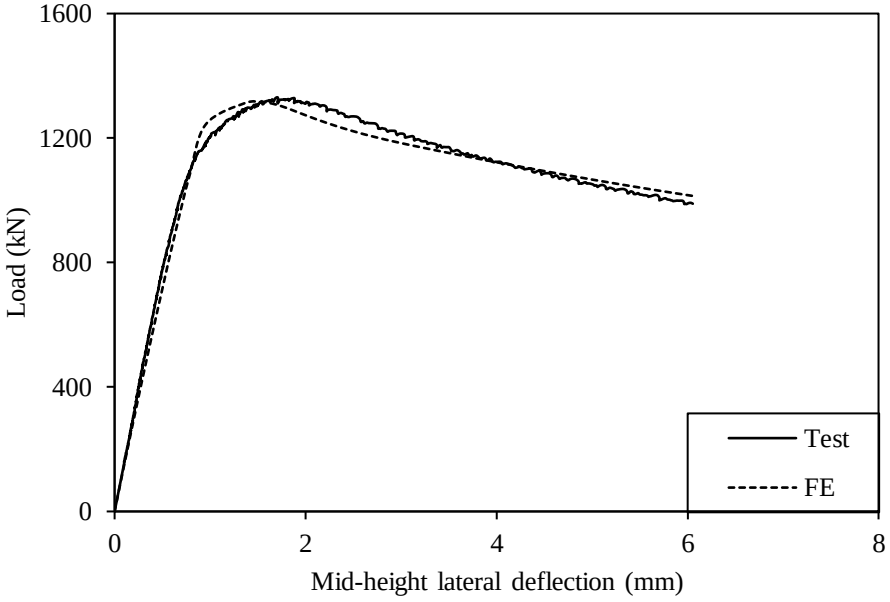

(a) Specimen C2.

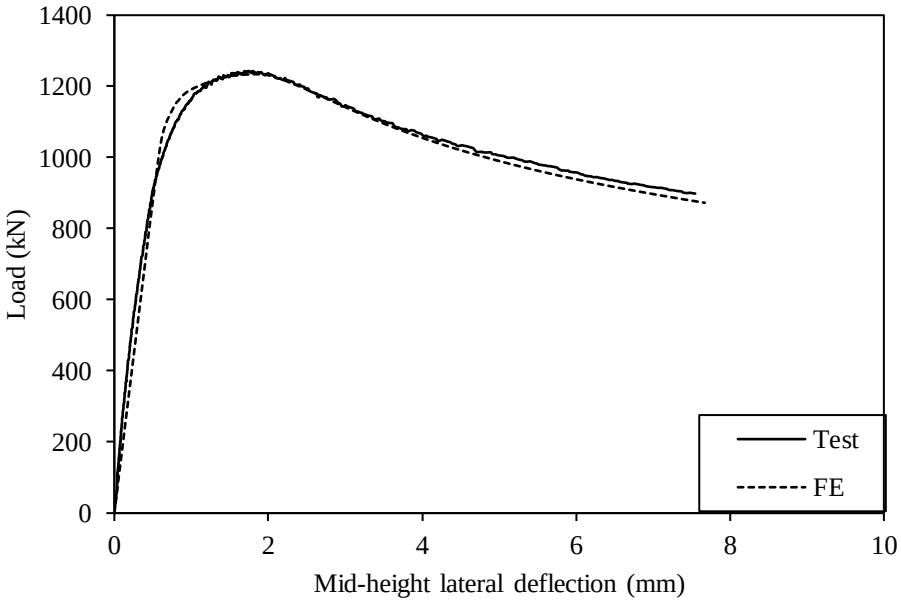

(b) Specimen D2.

Figure 6.10: Test and numerical load–lateral deflection curves of S960 ultra-high strength steel welded I-sections under major-axis combined loading.

(a) Specimen A4

(b) Specimen B1

Figure 6.11: Test and numerical failure modes for specimens under minor-axis combined loading.

(a) Specimen C2.

(b) Specimen D2

Figure 6.12: Test and numerical failure modes for specimens under major-axis combined loading.

6.3.4 Parametric studies

The developed FE models were employed to conduct parametric studies to expand the test data pool over a wider range of cross-section dimensions and loading combinations. The modelling assumptions, procedures and techniques used herein were the same as those described in Section 6.3.2, but with the initial local geometric imperfection magnitude now fixed as $t/100$. In terms of the modelled dimensions, the outer section depth was taken as 200 mm, while the flange widths ranging from 200 mm to 100 mm were selected, with the wall thicknesses varied from 4 mm to 10 mm, leading to a broad range of cross-section aspect ratios and dimensions being considered. Note that all the modelled I-sections were classified as slender sections, according to the slenderness limits given in EN 1993-1-12 (CEN, 2007), ANSI/AISC 360-16 (AISC, 2016) and AS 4100 (AS, 2016). The length of each FE model was set to be equal to three times its mean outer cross-section dimensions (Ziemian, 2010). Moreover, the initial loading eccentricities were varied from 0.5 mm to 1200 mm, resulting in a wide spectrum of loading combinations being accounted for. A total of 115 numerical data on S960 ultra-high strength steel welded I-sections under minor-axis combined loading and 120 numerical data on major-axis combined loading were generated through the present parametric studies, with the detailed geometric dimensions listed in Table 6.7.

Table 6.7: Cross-section dimensions and loading eccentricities of modelled S960 ultra-high strength steel welded I-sections in parametric studies.

(a) Minor-axis combined loading

h (mm)	b_f (mm)	t (mm)	Eccentricity (mm)
200	200	8	1, 2, 5, 12, 18, 25, 40, 60, 95, 110, 160, 240, 400, 600, 800
	200	6.5	1, 3, 6, 11, 14, 18, 24, 30, 40, 50, 70, 90, 120, 160, 240, 280, 330, 500, 630, 800
	160	6	1, 2, 3, 5, 7, 8, 11, 14, 22, 27, 30, 34, 49, 62, 100, 150, 200, 260, 400, 800
	140	6	1, 2, 4, 5, 6, 8, 12, 17, 25, 35, 48, 64, 75, 90, 110, 130, 240, 250, 400, 800
	120	5.5	1, 2, 5, 8, 11, 15, 19, 24, 29, 30, 37, 39, 45, 60, 75, 90, 120, 200, 500, 700
	100	5	2, 3, 5, 8, 12, 14, 17, 24, 32, 40, 49, 65, 82, 100, 120, 150, 210, 300, 450, 800

(b) Major-axis combined loading

h (mm)	b_f (mm)	t (mm)	Eccentricity (mm)
200	200	10.0	3, 15, 25, 37, 70, 100, 130, 200, 550, 1000
	190	9.5	8, 20, 31, 50, 85, 115, 165, 300, 450, 800
	180	9.0	4, 13, 27, 46, 70, 112, 170, 240, 480, 770
	170	8.5	6, 24, 42, 61, 99, 120, 149, 170, 260, 360
	160	8.0	0.5, 7, 19, 40, 77, 105, 140, 180, 250, 350
	150	7.5	1, 13, 30, 55, 70, 85, 109, 200, 240, 600
	140	7.0	4, 12, 22, 45, 55, 77, 95, 240, 370, 900
	130	6.5	6, 11, 30, 55, 80, 140, 200, 480, 630, 1200

120	6.0	10, 60, 73, 120, 140, 150, 165, 180, 270, 530
110	5.5	7, 17, 24, 49, 62, 98, 220, 290, 370, 400
100	4.5	2, 8, 12, 22, 42, 55, 86, 105, 144, 188
100	4.0	2, 25, 37, 70, 100, 130, 200, 260, 500, 1000

6.4 Evaluation of current design standards

6.4.1 General

The current EN 1993-1-12 (CEN, 2007), ANSI/AISC 360-16 (AISC, 2016) and AS 4100 (AS, 2016) only cover the design of steel structures with nominal material yield stresses less than or equal to 700 MPa (or 690 MPa), and thus none of the design standards can be directly used for the studied S960 ultra-high strength steel welded I-sections under combined loading. In this section, the applicability of the codified design interaction curves for S700 (or S690) high strength steel welded I-sections under combined loading to their S960 ultra-high strength steel counterparts was evaluated by comparing the test and numerical failure loads N_u against the unfactored design failure loads $N_{u,pred}$. Tables 6.8 and 6.9 report the mean test and numerical to predicted failure load ratios of $N_u/N_{u,pred}$ and the corresponding coefficients of variation (COV) for each codified design interaction curve, while the graphical evaluation results for S960 ultra-high strength steel welded I-sections under combined loading are shown in Figures 6.13–6.18.

6.4.2 EN 1993-1-12 (EC3)

The European code EN 1993-1-12 (CEN, 2007) was developed for high strength steel structures with material grades greater than S460 up to S700. It provides no specific

design rules for cross-sections under combined loading but directly adopts the relevant design rules given in EN 1993-1-1 (CEN, 2005). A linear interaction curve is used for the design of Class 4 welded I-sections under combined compression and bending moment, as given by Equation (6.2), where $N_{u,pred}$ is the design failure load and $M_{u,pred}=N_{u,pred}(e_0+\Delta_u)$ is the design failure moment about the axis of combined loading, while $N_{eff,EC3}=A_{eff,EC3}f_y$ is the EC3 effective cross-section compression capacity and $M_{eff,EC3}=W_{eff,EC3}f_y$ is the EC3 effective cross-section bending capacity about the rotation axis, where $A_{eff,EC3}$ is the effective cross-section area and $W_{eff,EC3}$ is the effective section modulus about the rotation axis. The values of $A_{eff,EC3}$ and $W_{eff,EC3}$ can be determined based on the EC3 effective width method (CEN, 2006), which considers the loss of effectiveness due to local buckling through reduction in plate element widths. The effective cross-section area $A_{eff,EC3}$ is equal to the summation of the effective area of each constituent plate element, which is calculated as the effective plate element width $c_{eff,EC3}$ multiplied by the wall thickness t. The expression for the effective plate element width $c_{eff,EC3}$ is given by Equation (6.3), where c is the flat plate element width, ψ is the stress ratio and equal to unity for pure compression, and $\overline{\lambda}_p$ is the plate element slenderness, as defined by Equation (6.4), where k_σ is the buckling parameter and equal to 4.0 and 0.43 for internal and outstand plate elements, respectively (CEN, 2006). Equations (6.3) and (6.4) are also used to calculate the effective section modulus $W_{eff,EC3}$, but with different values of k_σ and ψ, which are now dependent on the plate element type and the stress distribution within the plate element and can be determined according to Tables 4.1 and 4.2 of EN 1993-1-5 (CEN, 2006). Note that the calculation of $M_{eff,EC3}$ involves cumbersome iterations, owing to the shift of effective neutral axis.

$$\frac{N_{u,pred}}{N_{eff,EC3}}+\frac{M_{u,pred}}{M_{eff,EC3}}\le 1 \tag{6.2}$$

$$c_{eff,EC3}=\begin{cases} c\left(\dfrac{1}{\overline{\lambda}_p}-\dfrac{0.188}{\overline{\lambda}_p^{\,2}}\right)\le c & \text{for outstand plate elements} \\ c\left(\dfrac{1}{\overline{\lambda}_p}-\dfrac{0.055(3+\psi)}{\overline{\lambda}_p^{\,2}}\right)\le c & \text{for internal plate elements} \end{cases} \tag{6.3}$$

$$\overline{\lambda}_p=\frac{c/t}{28.4\sqrt{235/f_y}\sqrt{k_\sigma}} \tag{6.4}$$

The applicability of the EC3 design interaction curve to S960 ultra-high strength steel slender welded I-sections under combined compression and minor-axis bending moment was evaluated based on the test and numerical data, with Figure 6.13 depicting the graphical evaluation results, where the test and numerical failure moments and loads, normalised by the effective cross-section bending and compression capacities, are compared with the EC3 design interaction curve. It can be found that the EC3 design interaction curve lies well below the normalised test and FE data points, indicating excessive conservatism and scatter. This is also evident in Table 6.7, where the mean test and numerical to EC3 predicted failure load ratio $N_u/N_{u,pred}$ is equal to 1.65 with the corresponding COV of 0.13. It is worth noting that EN 1993-1-12 (CEN, 2007) leads to accurate effective cross-section compression capacities $N_{eff,EC3}$ when used for S960 ultra-high strength steel slender welded I-sections (Su et al., 2021b), i.e. the compression end point of the EC3 design interaction curve is accurate, as can also be seen from Figure 6.13. This indicates that the inaccuracy of the EC3 design interaction curve can be mainly attributed to the conservative bending end point (i.e. the minor-axis effective cross-section bending capacity $M_{eff,z,EC3}$).

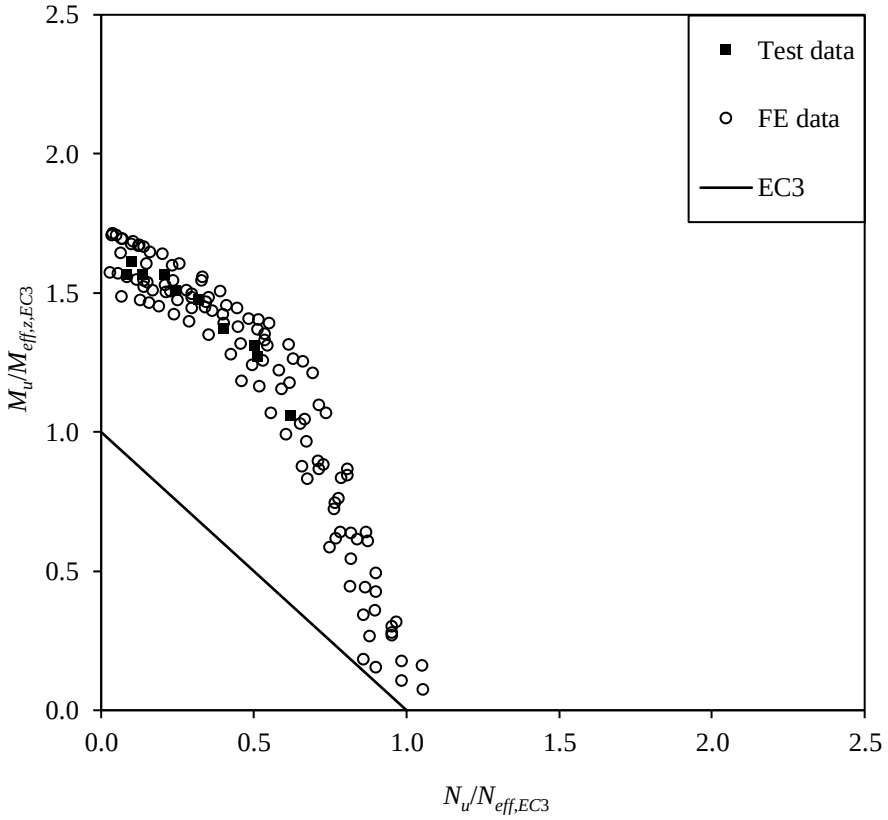

Figure 6.13: Comparisons of test and FE data with EC3 design interaction curve for minor-axis combined loading.

Table 6.8: Comparisons of test and numerical failure loads with EC3, AISC and AS predicted failure loads for S960 ultra-high strength steel welded I-sections under minor-axis combined loading.

Design code	No. of test data	No. of FE data	$N_u/N_{u,pred}$	
			Mean	COV
EN 1993-1-12	10	115	1.65	0.13
AISC 360	10	115	1.62	0.14
AS 4100	10	115	1.80	0.16

Regarding the applicability of the EC3 design interaction curve to S960 ultra-high strength steel welded I-sections under major-axis combined loading, the predicted failure loads and moments from EN 1993-1-12 (CEN, 2007) were compared with the derived test and numerical data. Figure 6.14 displays the graphical assessment results,

where the test and numerical failure loads and moments were respectively normalised by the EC3 effective cross-section compression and major-axis bending resistances, and compared with the EC3 linear interaction curve; the EC3 interaction curve is found to lie well above the normalised FE and test data points, revealing design conservatism. This can also be seen from the quantitative assessment results, as reported in Table 6.9, where the mean test and FE to EC3 predicted failure load ratio $N_u/N_{u,pred}$ equal to 1.31. As EN 1993-1-12 (CEN, 2007) leads to accurate effective cross-section compression capacities $N_{eff,EC3}$ when used for S960 ultra-high strength steel slender welded I-sections (Su et al., 2021b), as described above, the design conservatism can be mainly attributed to the conservative bending end point (i.e. the major-axis effective cross-section bending capacity $M_{eff,y,EC3}$).

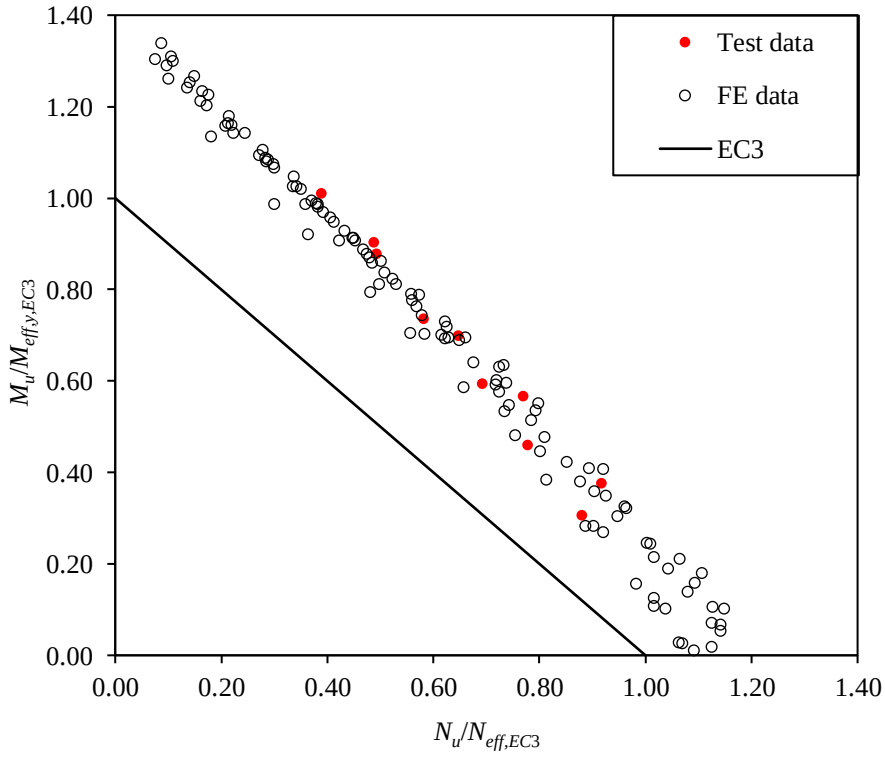

Figure 6.14: Comparisons of test and FE data with EC3 design interaction curve for major-axis combined loading.

Table 6.9: Comparisons of test and numerical failure loads with EC3, AISC and AS predicted failure loads for S960 ultra-high strength steel welded I-sections under major-axis combined loading.

Design code	No. of test data	No. of FE data	$N_u/N_{u,pred}$	
			Mean	COV
EN 1993-1-12	10	120	1.31	0.057
AISC 360	10	120	1.19	0.046
AS 4100	10	120	1.19	0.050

6.4.3 ANSI/AISC 360-16 (AISC)

The American specification ANSI/AISC 360-16 (AISC, 2016) provides design rules for steel components with material yield stresses up to 690 MPa. Regarding the design of slender welded I-sections under combined compression and bending moment, a bi-linear interaction curve is adopted, as given by Equation (6.5), where $N_{eff,AISC}=A_{eff,AISC}f_y$ is the AISC effective cross-section compression capacity and $M_{eff,ASIC}$ is the AISC effective cross-section bending capacity about the axis of combined loading. The AISC effective cross-section area $A_{eff,AISC}$ is now determined based on the AISC effective width method, with the effective plate element width $c_{eff,AISC}$ calculated from Equation (6.6), where $\bar{\lambda}_{r,out}$ and $\bar{\lambda}_{r,int}$ are the AISC limiting width-to-thickness ratios for non-compact/slender outstand and internal plate elements in pure compression, respectively, which can be determined according to Table B4.1a in ANSI/AISC 360-16 (AISC, 2016). The AISC effective cross-section bending capacity about the minor principal axis $M_{eff,z,AISC}$ *is* calculated by Equation (6.7), where $M_{el,z}$ is the corresponding cross-section elastic moment capacity, while $M_{eff,y,AISC}$ is the AISC effective cross-section bending resistance about the major axis, which can be calculated by (i) Equation (6.8) for slender I-sections with slender flanges, and (ii) Equations (6.9) and (6.10) for slender welded I-sections with slender webs but compact/noncompact flanges, where $W_{el,y}$ is the major-axis elastic section modulus, and k_c is equal to $4/[(h\text{-}2t)/t]^{0.5}$, but should be greater than 0.35 and less than

0.76. It is worthy of mentioning that λ_{pf} and λ_{rf} given in Equation (6.10) respectively denote the limiting slendernesses for compact/non-compact and non-compact/slender flanges under major-axis bending, which can be determined based on Table B4.1b in AISC 360 (AISC, 2016).

$$\begin{cases} \dfrac{N_{u,pred}}{N_{eff,AISC}} + \dfrac{8}{9}\dfrac{M_{u,pred}}{M_{eff,AISC}} \le 1 & \text{for } \dfrac{N_{u,pred}}{N_{eff,AISC}} \ge 0.2 \\ \dfrac{N_{u,pred}}{2N_{eff,AISC}} + \dfrac{M_{u,pred}}{M_{eff,AISC}} \le 1 & \text{for } \dfrac{N_{u,pred}}{N_{eff,AISC}} < 0.2 \end{cases} \tag{6.5}$$

$$c_{eff,AISC} = \begin{cases} c\left(\dfrac{1.49\bar{\lambda}_{r,out}}{c/t} - \dfrac{0.49\bar{\lambda}_{r,out}^2}{(c/t)^2}\right) \le c & \text{for outstand plate elements} \\ c\left(\dfrac{1.31\bar{\lambda}_{r,\text{int}}}{c/t} - \dfrac{0.31\bar{\lambda}_{r,\text{int}}^2}{(c/t)^2}\right) \le c & \text{for internal plate elements} \end{cases} \tag{6.6}$$

$$M_{eff,z,AISC} = M_{el,z}\frac{0.69}{\left[b_f \Big/ \left(2t\sqrt{E/f_y}\right)\right]^2} \tag{6.7}$$

$$M_{eff,y,AISC} = \frac{0.9Ek_cW_{el,y}}{(b/2t)^2} \tag{6.8}$$

$$M_{eff,y,AISC} = W_{el,y}f_y\left(1 - \frac{(h-2t)/b}{1200+300(h-2t)/b}\right)\left(\frac{h-2t}{t} - 5.7\sqrt{\frac{E}{f_y}}\right) \le W_{el,y}f_y \tag{6.9}$$

$$M_{eff,y,AISC} = W_{el,y}f_y\left(1 - 0.3\left(\frac{b/2t - \lambda_{pf}}{\lambda_{rf} - \lambda_{pf}}\right)\right) \tag{6.10}$$

The AISC predicted failure loads were compared with the test and numerical failure loads, to assess the applicability of the AISC design interaction curve to S960 ultra-high strength steel slender welded I-sections under minor-axis combined loading. Table 6.7 reports the mean test and numerical to AISC predicted failure load ratio $N_u/N_{u,pred}$ and the corresponding COV, which are equal to 1.62 and 0.14, respectively, revealing a high degree of conservatism and scatter, as can also be seen from Figure 6.15, where the normalised test and numerical data points lie far above the AISC

design interaction curve. In view of that the AISC effective cross-section compression capacities $N_{eff,AISC}$ (i.e. the compression end point) are accurate for S960 ultra-high strength steel slender welded I-sections (Su et al., 2021b), the inaccuracy of the AISC design interaction curve is mainly owing to the conservative bending end point – $M_{eff,z,AISC}$. It is also worth noting that ANSI/AISC 360-16 (AISC, 2016) offers improved design accuracy than EN 1993-1-12 (CEN, 2007), due to the more accurate bi-linear shape of the interaction curve.

The applicability of the AISC design interaction curve to S960 ultra-high strength steel slender welded I-sections under major-axis combined loading was also assessed, based on the obtained test and numerical data. Both the quantitative and graphical assessments were carried out, with the results summarised in Table 6.9 and Figure 6.16, respectively. It is evident from Table 6.9 that AISC leads to accurate and consistent resistance predictions for S960 ultra-high strength steel welded I-sections under major-axis combined loading, with the mean test and FE to AISC predicted failure load ratio being 1.19 and the corresponding COV equal to 0.046. This can also be observed from the graphical evaluation in Figure 6.16, where the AISC bi-linear interaction curve displays a good representation of the normalised test and FE data points. Compared with its EC3 counterpart, the AISC interaction curve yields less scattered and more accurate failure load predictions, owing to the adoption of more accurate bi-linear interaction curves and bending end point.

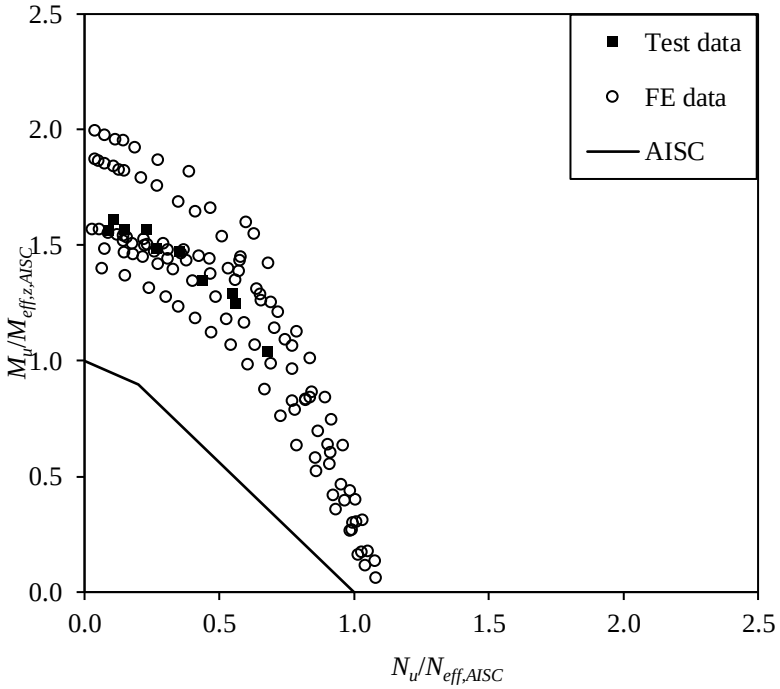

Figure 6.15: Comparisons of test and FE data with AISC design interaction curve for minor-axis combined loading.

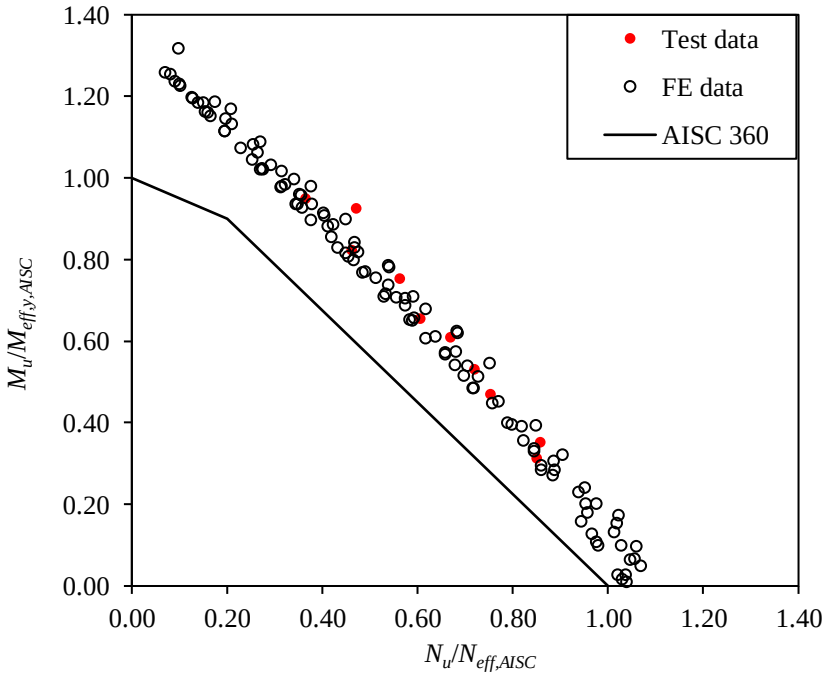

Figure 6.16: Comparisons of test and FE data with AISC design interaction curve for major-axis combined loading.

6.4.4 AS 4100 (AS)

The Australian standard AS 4100 (AS, 2016) is applicable to steel members with material yield stresses up to 690 MPa. AS 4100 (AS, 2016) adopts a linear interaction curve for the design of slender welded I-sections under combined loading, as defined by Equation (6.11), where $N_{eff,AS}=A_{eff,AS}f_y$ is the AS effective cross-section compression capacity and $M_{eff,AS}$ is the AS effective cross-section bending capacity about the axis of combined loading. Note that the AS linear interaction formula (Equation (6.11)) is the same as its EC3 counterpart (Equation 6.2)), with the only difference lying in the calculation of the effective cross-section compression and bending capacities. Specifically, the AS effective cross-section area $A_{eff,AS}$ is now calculated based on the AS effective width method, with the effective plate element width $c_{eff,AS}$ given by Equation (6.12). The effective cross-section bending capacity about the minor principal axis $M_{eff,z,AS}$ can be determined by Equation (6.13), while effective cross-section bending capacity about the major principal axis $M_{eff,y,AS}$ is determined utilizing Equation (6.14), where λ_{sy} is the AS yield slenderness limit for flanges and λ_s is the AS section slenderness and is determined according to Clause 5.2.2 of AS 4100 (AS, 2016).

$$\frac{N_{u,pred}}{N_{eff,AS}}+\frac{M_{u,pred}}{M_{eff,AS}}\le 1 \tag{6.11}$$

$$c_{eff,AS}=\begin{cases} c\left[\dfrac{14}{c\Big/\left(t\sqrt{250/f_y}\right)}\right]\le c & \text{for outstand plate elements} \\ c\left[\dfrac{35}{c\Big/\left(t\sqrt{250/f_y}\right)}\right]\le c & \text{for internal plate elements} \end{cases} \tag{6.12}$$

$$M_{eff,z,AS}=\left(\frac{\lambda_{sy}}{\lambda_s}\right)^2 M_{el,z} \tag{6.13}$$

$$M_{eff,y,AS}=\frac{\lambda_{sy}}{\lambda_s}W_{el,y}f_y \tag{6.14}$$

The failure loads for S960 ultra-high strength steel slender welded I-sections under minor-axis combined loading, as predicted from the AS design interaction curve, were graphically and quantitatively evaluated against the corresponding test and numerical failure loads, with the results shown in Figure 6.17 and Table 6.7. It can be found that AS 4100 (AS, 2016) results in the lowest degree of design accuracy and consistency among the three considered design standards.

The AS design interaction formulation was also graphically and quantitatively assessed for its applicability to S960 ultra-high strength steel slender welded I-sections under major-axis combined loading, based on the test and FE data, as shown in Figure 6.18 and Table 6.9. Both the quantitative and graphical assessment results indicated that the AS interaction formulation (AS, 2016) is capable of well predicting the failure loads for S960 ultra-high strength steel slender welded I-sections under major-axis combined loading.

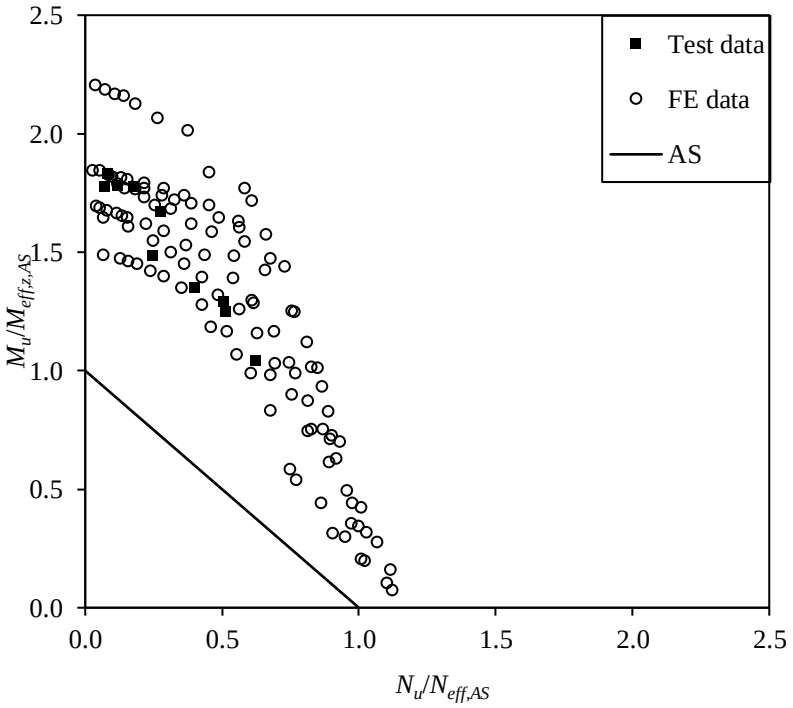

Figure 6.17: Comparisons of test and FE data with AS design interaction curve for minor-axis combined loading.

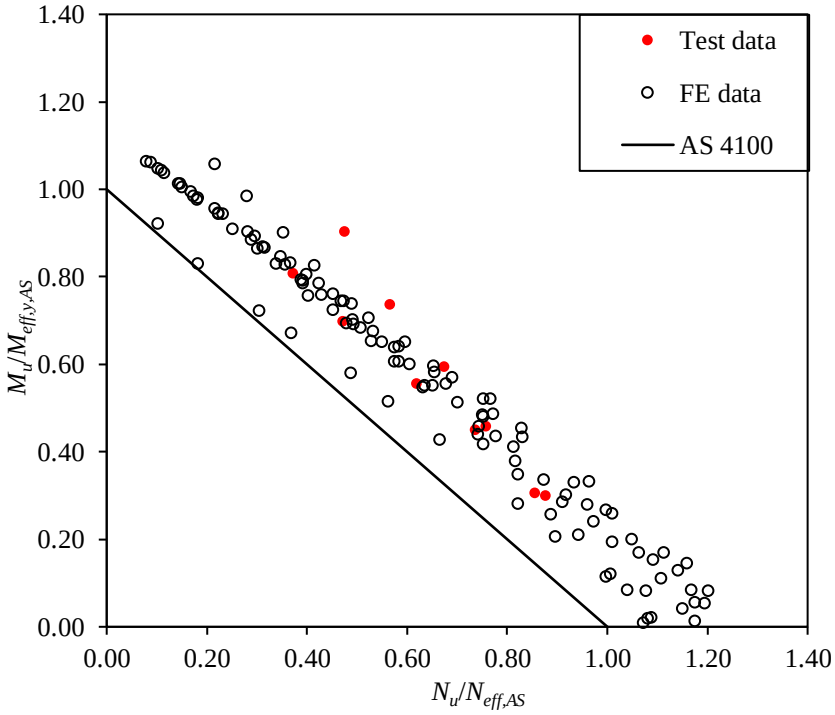

Figure 6.18: Comparisons of test and FE data with AS design interaction curve for major-axis combined loading.

6.5 Concluding remarks

A comprehensive experimental and numerical modelling programme has been conducted to investigate the cross-section behaviour and resistances of S960 ultra-high strength steel welded I-sections under combined compression and bending moment. The experimental programme included ten minor-axis eccentric compression tests, ten major-axis eccentric compression tests and initial local geometric imperfection measurements on S960 ultra-high strength steel slender welded I-section stub column specimens. This was followed by a numerical modelling programme, where FE models were firstly developed and validated against the test results and then used to perform parametric studies to generate further numerical data over a wide range of cross-section dimensions and loading combinations. The test and numerical data were used to evaluate the applicability of the design interaction curves for S700 (or S690) high strength steel slender welded I-

sections under combined loading, as set out in EN 1993-1-12 (CEN, 2007), ANSI/AISC 360-16 (AISC, 2016) and AS 4100 (AS, 2016), to their S960 ultra-high strength steel counterparts. The evaluation results generally indicated that (i) all the three codified design interaction curves lead to unduly conservative and scattered failure load predictions for minor-axis combined loading, mainly due to the conservative bending end points (i.e. the minor-axis effective cross-section bending capacities) and (ii) EN 1993-1-12 (CEN, 2007) yields safe but conservative cross-section resistances for S960 ultra-high strength steel welded I-sections under major-axis combined loading, while the design interaction curves in ANSI/AISC 360-16 (AISC, 2016) and AS 4100 (AS, 2016) lead to more accurate and consistent predictions of failure loads, compared to their EC3 counterpart, with the highest design accuracy and consistency provided by ANSI/AISC 360-16 (AISC, 2016), due principally to the adoption of a bi-linear interaction curve anchored to a more accurate bending end point.

CHAPTER 7

BUCKLING OF S960 ULTRA-HIGH STRENGTH STEEL WELDED I-SECTION BEAM-COLUMNS

7.1 Introduction

This chapter reports experimental and numerical investigations of the buckling behaviour and resistances of S960 ultra-high strength steel welded I-section beam-columns. A testing programme was firstly conducted, comprising initial geometric imperfection measurements and minor-axis eccentric compression tests on eight S960 ultra-high strength steel welded I-section beam-column specimens. The key test results, together with the test setups and procedures, were fully reported. Following the testing programme, a numerical modelling programme was carried out, where finite element models were developed and validated against the test results, and then utilised to perform parametric studies to generate additional numerical data over an extensive range of cross-section sizes, member lengths and loading combinations. On the basis of the obtained test and numerical results, the applicability of the design interaction expressions for S690 (or S700) high strength steel welded I-section beam-columns, set out in the European, American and Australian codes, to S960 ultra-high strength steel counterparts were evaluated. The evaluation results and key findings of this research have been reported in Su et al. (2020f).

7.2 Testing

7.2.1 General

Given that there have been no experimental results on S960 ultra-high strength steel welded I-section beam-columns, a testing programme was firstly carried out to establish a test data bank. The testing programme adopted two welded I-section sizes: I-150×75×6 and I-120×120×6, which are both categorised as Class 4 cross-sections, based on EN 1993-1-12 (CEN, 2007), and are also classified as slender cross-sections, in accordance with ANSI/AISC 360-16 (AISC, 2016) and AS 4100 (AS, 2016). Eight beam-column specimens were prepared, all of which were fabricated by robotic GMAW from 6 mm thick S960 ultra-high strength steel plates. The material properties and chemical compositions of S960 ultra-high strength steel, the used electrode and membrane residual stresses of the studied I-sections were detailed in Chapter 3. The adopted I-section labelling system is same as those described in the previous chapters, consisting of the cross-section identifier (i.e. cross-section height h × flange width b_f × material thickness t) – see Figure 6.1, with 'A' and 'B' respectively denoting I-150×75×6 and I-120×120×6, and a number to distinguish different initial loading eccentricities for geometrically identical beam-column specimens. The section ID and experimentally measured geometric properties of all the examined beam-columns are reported in Table 7.1. The overall testing programme included initial geometric imperfection measurements and eight beam-column tests about the minor principal axis.

Table 7.1：Key geometric properties of S960 ultra-high strength steel welded I-section beam-column specimens.

Cross-section	Specimen ID	L (mm)	L_e (mm)	b_f (mm)	h (mm)	t (mm)	ω_0 (mm)	ω_g (mm)
I-150×75×6	A1	551	691	74.93	150.25	6.03	0.07	0.31
	A2	550	690	74.73	150.20	6.04	0.09	0.37
	A3	550	690	74.68	150.01	6.01	0.09	0.30
	A4	551	691	74.49	150.12	6.02	0.07	0.29
I-120×20×6	B1	661	801	119.24	119.36	5.98	0.07	0.45
	B2	660	800	119.27	119.28	5.98	0.06	0.43
	B3	662	802	119.92	119.89	6.03	0.06	0.40
	B4	659	799	119.52	119.64	5.99	0.09	0.43

7.2.2 Beam-column tests

Minor-axis eccentric compression tests were conducted to investigate the buckling behaviour and resistances of S960 ultra-high strength steel welded I-section beam-columns. For each adopted I-section size, four geometrically identical beam-column specimens were tested with different initial loading eccentricities ranging from 20 mm to 100 mm being applied. It is worth noting that the initial geometric imperfection measurements adopted the same test setup and procedures as those described in Section 5.2.2. An INSTRON 5000 kN testing machine was used to test all the beam-column specimens at a constant loading rate of 0.2 mm/min. The knife-edge assemblies at both ends of the machine, as shown in Figure 7.1, were employed to offer pin-ended boundary conditions. Prior to testing, position adjustment of each specimen (welded with end plates) was made, based on spirit levels and lasers, to achieve the pre-specified eccentricity. Note that the distance between the specimen end and the rotation centre of the knife-edge device was equal to 70 mm – see Figure 7.1; the member effective lengths of the beam-column specimens are thus calculated as L_e=L+140 mm, as given in Table 7.1.

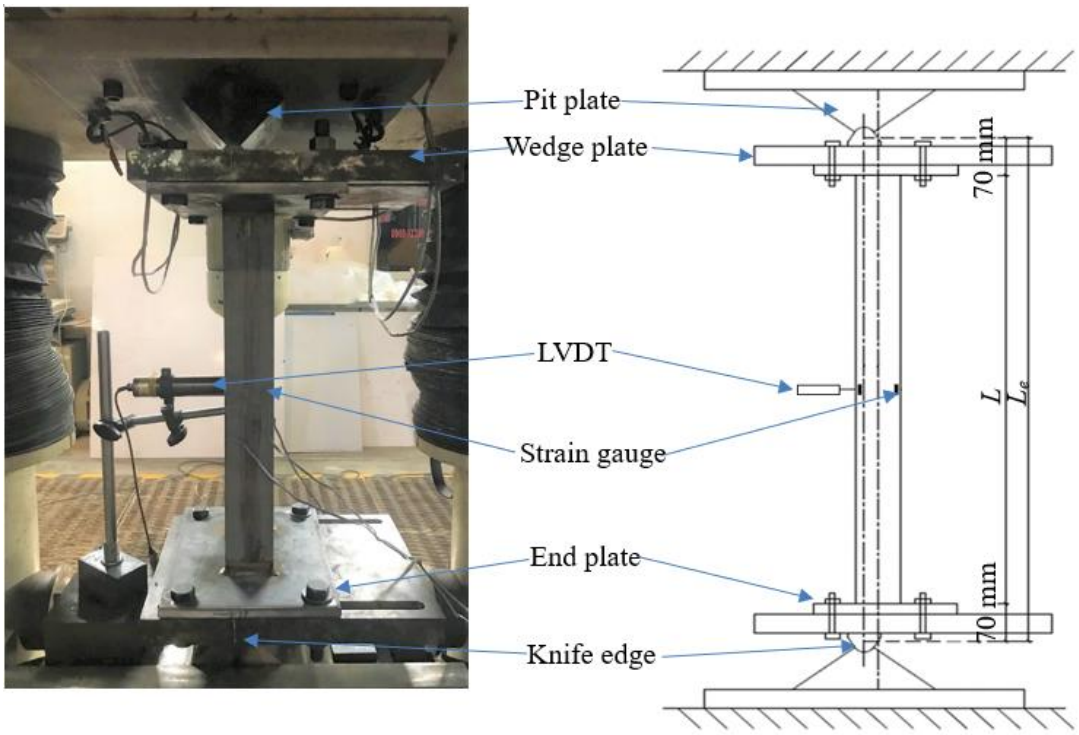

Figure 7.1: Beam-column test setup

Figure 7.1 depicts the test setup for the eccentric compression tests on S960 ultra-high strength steel welded I-section beam-columns, including (i) one LVDT, placed longitudinally at specimen mid-height, to record the lateral deflections about the minor principal axis, and (ii) two pairs of strain gauges, attached to the outstand flanges at mid-height, with the detailed locations depicted in Figure 6.1, to record the longitudinal strains at the corresponding positions. The readings recorded from the LVDT and strain gauges were used to calculate the actual initial loading eccentricity e_0 of each beam-column specimen, based on Equation (6.1). Figures 7.2 and 7.3 display the failure modes of the tested I-150×75×6 and I-120×120×6 beam-column specimens; all of them exhibited flexural buckling coupled with in-plane bending deformation. The obtained load–mid-height lateral deflection curves for the two series of S960 ultra-high strength steel welded I-section beam-column specimens are shown in Figures 7.4 and 7.5, while the measured key test results are presented in Table 7.2, including the failure load N_u, the mid-height lateral deflection

corresponding to the failure load Δ_u, the actual initial loading eccentricity e_0, and the first-order elastic ($M_{u,1st,el}$), second-order elastic ($M_{u,2nd,el}$) and second-order inelastic ($M_{u,2nd,inel}$) failure bending moments at the specimen mid-height, as calculated from Equations (7.2)–(7.4), respectively. Note that N_{cr} is the Euler buckling strength about the minor principal axis and can be derived by Equation (7.5).

$$M_{u,1st,el} = N_u \left(e_0 + \omega_g \right) \tag{7.2}$$

$$M_{u,2nd,el} = \frac{M_{u,1st,el}}{\left(1 - N_u / N_{cr}\right)} \tag{7.3}$$

$$M_{u,2nd,inel} = N_u \left(e_0 + \omega_g + \Delta_u \right) \tag{7.4}$$

$$N_{cr} = \frac{\pi^2 E I_z}{L_e^{\,2}} \tag{7.5}$$

Table 7.2: Key test results for S960 ultra-high strength steel welded I-section beam-column specimens.

Cross-section	Specimen ID	e_0 (mm)	N_u (kN)	Δ_u (mm)	$M_{u,1st,el}$ (kNm)	$M_{u,2nd,el}$ (kNm)	$M_{u,2nd,inel}$ (kNm)
I-150×75×6	A1	21.5	452.6	15.6	9.9	13.2	16.9
	A2	29.4	393.1	15.1	11.7	15.0	17.7
	A3	40.0	299.9	16.2	12.1	14.5	16.9
	A4	88.1	156.2	18.9	13.8	15.1	16.7
I-120×120×6	B1	20.0	978.7	12.7	20.0	24.4	32.5
	B2	31.6	789.4	13.7	25.3	29.6	36.1
	B3	60.0	563.3	15.4	34.0	38.0	42.7
	B4	99.8	348.7	15.2	35.0	37.3	40.2

Figure 7.2: Failure modes of I-150×75×6 beam-column specimens.

Figure 7.3： Failure modes of I-120×120×6 beam-column specimens.

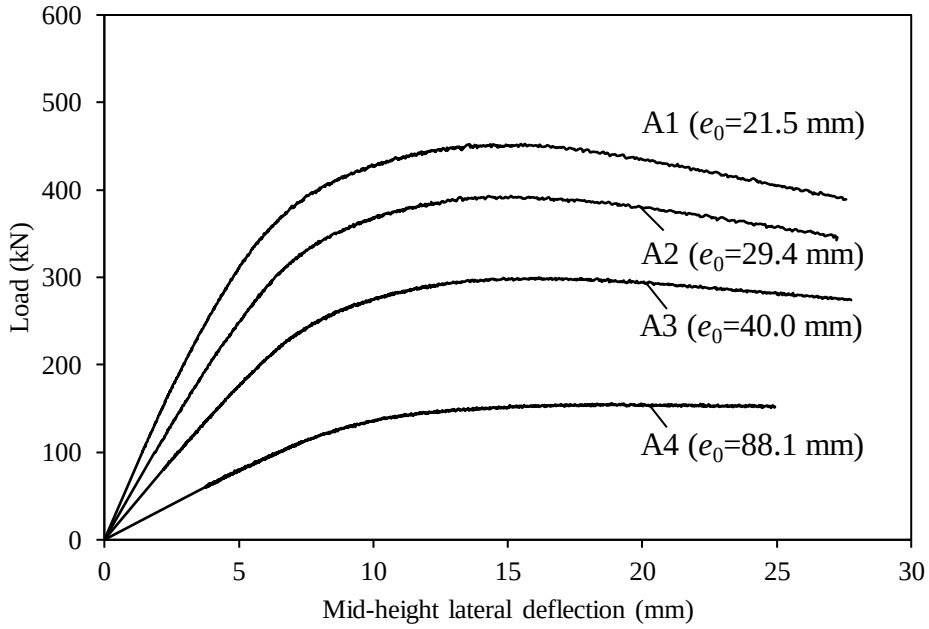

Figure 7.4: Load–mid-height lateral deflection curves for I-150×75×6 beam-column specimens.

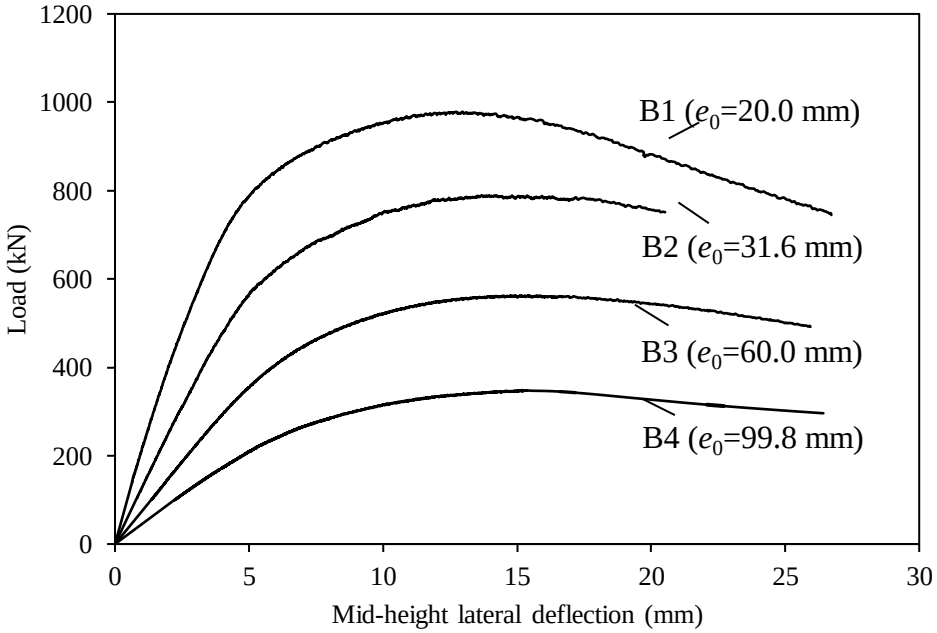

Figure 7.5: Load–mid-height lateral deflection curves for I-120×120×6 beam-column specimens.

7.3 Numerical modelling

7.3.1 General

In parallel with the testing programme, a numerical modelling programme was conducted, using the nonlinear finite element software ABAQUS (2014). FE models were firstly developed and validated against the test results, and then employed to perform parametric studies to generate further numerical data over a wide range of cross-section dimensions, member lengths and loading combinations.

7.3.2 Development of FE models

S960 ultra-high strength steel slender welded I-section beam-column FE models were developed based on the measured cross-section geometric dimensions and member effective length, employing the same modelling assumptions, procedures and techniques as those described in Section 6.3.2. Regarding the boundary conditions, the top end section was coupled to one reference point, with longitudinal translation and rotation about the minor principal axis allowed, while the bottom end section was coupled to the other reference point, with only rotation about the minor axis allowed. Both of the top and bottom reference points were located eccentrically to the minor principal axis, with the eccentricities given as the corresponding actual initial loading eccentricity e_0, as listed in Table 7.2, and each of them was longitudinally offset by 70 mm from the end sections. For the incorporation of initial geometric imperfections, two sets of global and local imperfection magnitude combinations, including (i) the measured magnitude combination – ω_g+ω_0 and (ii) a generalised magnitude combination – L_e/1000+t/100, were employed to scale the obtained initial geometric imperfection distribution patterns. Finally, the developed FE model was solved by the geometrically and materially nonlinear modified Riks method (ABAQUS, 2014), to

derive the numerical failure loads, load–mid-height lateral deflection curves and failure modes.

7.3.3 Validation of FE models

The accuracy of the developed FE models was evaluated based on the comparisons of the numerical results with the test data. The numerical to test failure load ratios for all the S960 ultra-high strength steel slender welded I-section beam-column specimens are presented in Table 7.3, and the results indicated that (i) the numerical failure loads are influenced by the initial geometric imperfection magnitudes and (ii) the test failure loads were well predicted when the generalised imperfection magnitude combination (i.e. $t/100+L_e/1000$) was incorporated into the beam-column FE models. Comparisons between the experimental and numerical failure modes for two typical beam-column specimens A2 and B3 are respectively displayed in Figures 7.6 and 7.7, indicating excellent agreement. The FE load–mid-height lateral deflection curves were also shown to well capture their experimental counterparts for the aforementioned specimens, as shown in Figures 7.8 and 7.9. Overall, it can be concluded that the developed FE models are capable of simulating the tests responses of S960 ultra-high strength steel welded I-section beam-columns and therefore deemed to be validated.

Figure 7.6: Test and numerical failure modes for S960 ultra-high strength steel slender welded I-section beam-column specimen A2.

Figure 7.7: Test and numerical failure modes for S960 ultra-high strength steel slender welded I-section beam-column specimen B3.

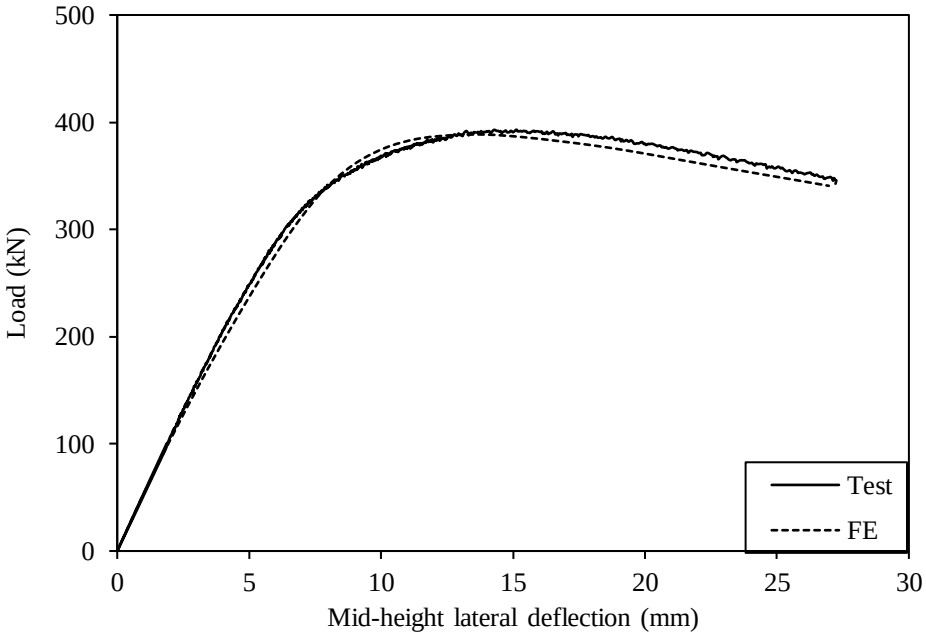

Figure 7.8: Test and numerical load–mid-height lateral deflection curves for S960 ultra-high strength steel slender welded I-section beam-column specimen A2.

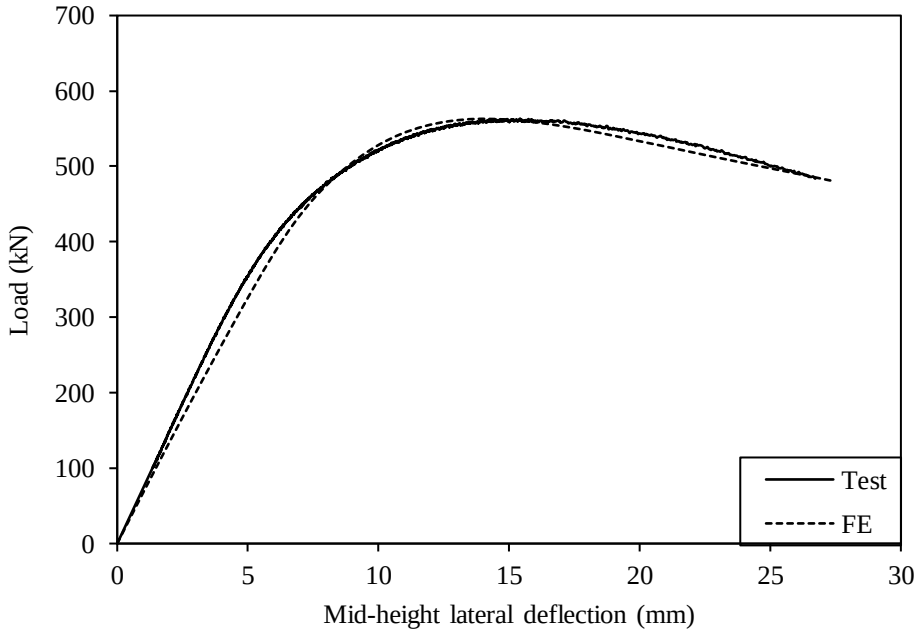

Figure 7.9: Test and numerical load–mid-height lateral deflection curves for S960 ultra-high strength steel slender welded I-section beam-column specimen B3.

Table 7.3: Comparison between test and numerical failure loads for measured and generalised initial global and local imperfection combinations.

Cross-section	Specimen ID	FE N_u / Test N_u	
		$\omega_g+\omega_0$	$L_e/1000+t/100$
I-150×75×6	A1	1.05	1.03
	A2	0.99	0.97
	A3	0.99	0.97
	A4	1.05	1.02
I-120×120×6	B1	1.04	1.01
	B2	0.97	0.94
	B3	1.02	1.00
	B4	0.99	0.97
	Mean	1.01	0.99
	COV	0.03	0.03

7.3.4 Parametric studies

The developed FE models were employed to perform parametric studies to generate further numerical data over a broad range of cross-section dimensions, member effective lengths and loading combinations. The modelled I-sections were categorised as slender (or Class 4) sections based on EN 1993-1-12 (CEN, 2007), ANSI/AISC 360-16 (AISC, 2015) and AS 4100 (AS, 2016). Specifically, the flange widths were varied from 75 mm to 200 mm, with the plate thicknesses ranging from 3 mm to 10 mm, resulting in a range of cross-section aspect ratios and dimensions being considered. The member effective lengths of the modelled I-sections fell between 700 mm and 2340 mm, leading to a wide spectrum of member non-dimensional slendernesses being considered. Moreover, the initial loading eccentricities (to the minor axis) of the FE models were varied from 0.1 mm to 600 mm, resulting in an extensive range of loading combinations being considered. The generalised initial global and local geometric imperfection magnitude combination – $L_e/1000$ and $t/100$ was adopted herein. In total, 176 numerical data on S960 ultra-high strength steel slender welded I-section beam-columns were generated through the

parametric studies.

7.4 Assessment of current design standards

7.4.1 General

In this section, the obtained experimental and numerical results were firstly discussed and then used to evaluate the applicability of the design interaction formulae for S690 (or S700) slender welded I-section beam-columns, as given in EN 1993-1-12 (CEN, 2007), ANSI/AISC 360-16 (AISC, 2016) and AS 4100 (AS, 2016), to S960 ultra-high strength steel counterparts. The graphical and quantitative evaluation results for the three considered design standards, with an angle parameter $\theta=\tan^{-1}[(N_{u,pred}/N_R)/(M_{u,pred}/M_R)]$ introduced to reflect the combination of compression and bending moment, as also graphically defined in Figure 7.10, where $N_{u,pred}$ is the design failure load and $M_{u,pred}= N_{u,pred}e_0$ is the design failure moment, while N_R and M_R are the corresponding column flexural buckling resistance and cross-section bending moment resistance. It is worth noting that All partial safety factors are taken as unity in the design analyses, leading to the unfactored design ultimate loads being discussed.

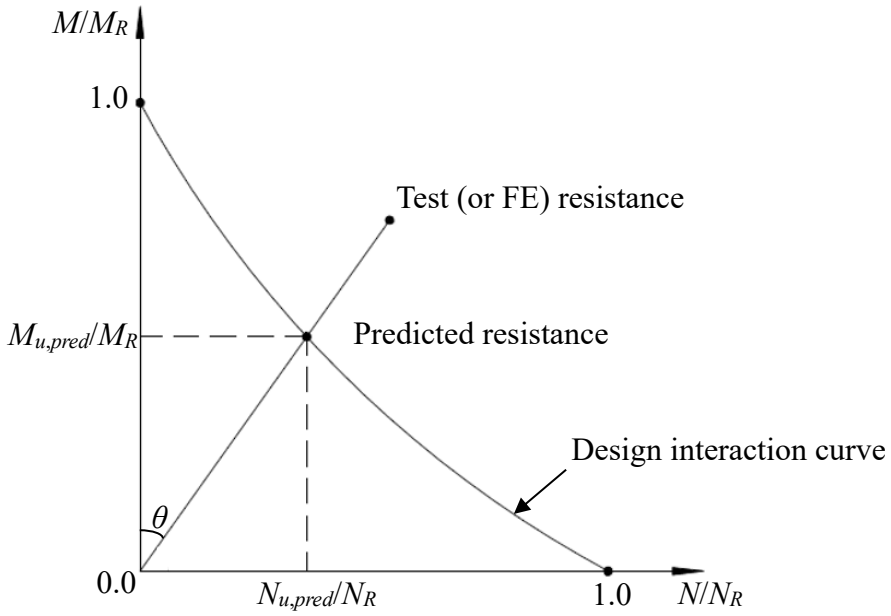

Figure 7.10: Definition of θ.

7.4.2 EN 1993-1-12 (EC3)

EN 1993-1-12 (CEN, 2007) employs the same format of design interaction formulae for S690 high strength steel slender welded I-section beam-columns as those adopted in EN 1993-1-1 (CEN, 2005) for their normal strength steel counterparts. For S690 high strength steel slender welded I-section beam-columns subjected to minor-axis combined loading, the EC3 design interaction expression is given by Equation (7.6), where N_b is the column flexural buckling strength, as given by Equations (5.1)–(5.4), $M_{eff,z,EC3}$ is the minor-axis effective bending resistance and cumbersome iterations were involved in its derivation, owing to the shift of effective neutral axis in each round of calculation, and k_z is the interaction factor, given by Equation (7.7), where C_{mz} is the equivalent uniform moment factor and calculated as unity from Table B.3 in EN 1993-1-1 (CEN, 2005), and λ_z is the member non-dimensional slenderness about the minor principal axis and determined based on Equation (7.8), where A_{eff} is the effective cross-section area and can be determined by the effective width method.

$$\frac{N_{u,pred}}{N_b} + k_z \left(\frac{M_{u,pred}}{M_{eff.z,EC3}} \right) \leq 1 \tag{7.6}$$

$$k_z = C_{mz} \left(1 + 0.6\lambda_z \frac{N_{u,pred}}{N_b} \right) \leq C_{mz} \left(1 + 0.6 \frac{N_{u,pred}}{N_b} \right) \tag{7.7}$$

$$\lambda_z = \sqrt{\frac{A_{eff} f_y}{N_{cr}}} \tag{7.8}$$

The suitability of the EC3 interaction curve to S960 UHSS slender welded I-section beam-columns was assessed against the obtained test and FE data. Figure 7.11 presents the graphical assessments, in which the test and FE to design ultimate load ratios $N_u/N_{u,pred}$ are plotted with reference to θ. The graphical assessment results revealed that the EC3 interaction curve yields conservative, though consistent, predictions of ultimate load for S960 UHSS slender welded I-section beam-columns. This is also evident in the quantitative assessments given in Table 7.4, in which the mean test and FE to design ultimate load ratio is 1.43 and the corresponding COV is 0.08. The conservatism of the ultimate load predictions is attributed to the conservative end points of the EC3 interaction design curve (i.e. minor-axis effective moment resistance and column buckling resistance), while the consistency of the ultimate load predictions generally demonstrates that the interaction curve shape, defined by the interaction factor, is appropriate.

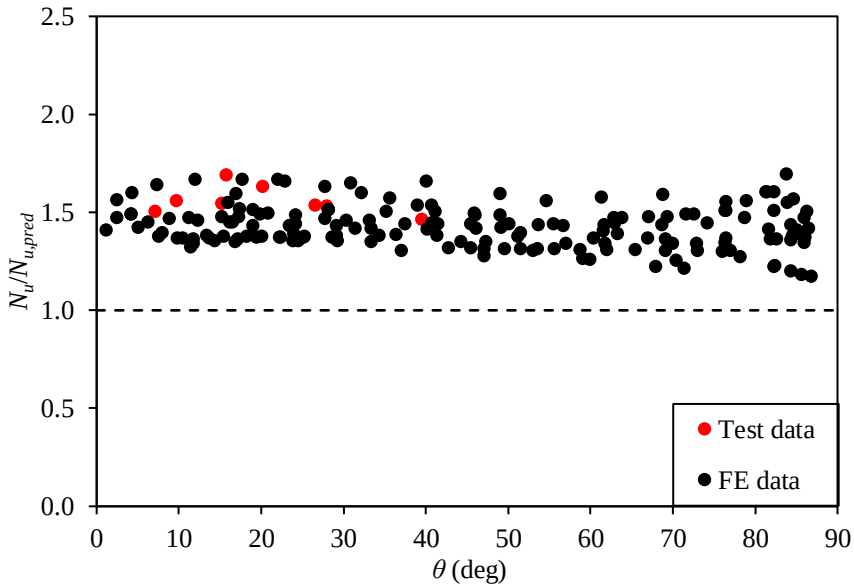

Figure 7.11: Comparisons of test and numerical failure loads with EC3 predicted failure loads.

Table 7.4: Comparisons of FE and test failure loads with AS, AISC and EC3 failure load predictions.

Design code	Cross-section category	No. of test data	No. of FE data	$N_u/N_{u,pred}$	
				Mean	COV
EN 1993-1-12	Class 4 section	8	176	1.43	0.08
AS 4100	Slender section	8	176	1.61	0.10
AISC 360	Slender section	8	176	1.36	0.08
New proposal	Slender section	8	176	1.28	0.09

7.4.3 AS 4100 (AS)

The current AS 4100 (AS, 2016) covers the design formulations and provisions for high strength steel structures with the material grades up to S690. The design interaction expression given by Equation (7.9), is employed for S690 high strength steel slender welded I-section beam-columns subjected to minor-axis combined

loading, where N_c is the minor-axis column buckling strength, as determined in Section 5.4.4, $M_{eff,z,AS}$ is the minor-axis effective moment resistance and can be derived by Equation (7.10), in which $M_{el,z}$ is the minor-axis elastic moment resistance, λ_{sy} is the AS yield slenderness limit for flanges and λ_s is the AS section slenderness, as determined based on Clause 5.2.2 of AS 4100 (AS, 2016), and δ_b=1/(1-$N_{u,pred}$/N_{cr}) is a moment amplification factor for taking into consideration the second-order effect.

$$\frac{N_{u,pred}}{N_c} + \delta_b \frac{M_{u,pred}}{M_{eff,z,AS}} \leq 1 \tag{7.9}$$

$$M_{eff,z,AS} = \left(\frac{\lambda_{sy}}{\lambda_s}\right)^2 M_{el,z} \tag{7.10}$$

The design ultimate loads determined from the AS interaction curve were evaluated against the test and numerical ultimate loads, with the quantitative evaluation results, including the mean ratio of N_u/$N_{u,pred}$ of 1.61 and the COV of 0.10, reported in Table 7.4. In parallel with quantitative evaluation, graphical evaluation was also conducted, as presented in Figure 7.12. It can be concluded that the Australian Standard yields even more conservative predictions of ultimate load for S960 UHSS slender welded I-section beam-columns subjected to minor-axis combined loading than the European code. In view of the fact that the COVs determined from both codified interaction curves do not have large difference (i.e. the influence of curve shape is not significant), the higher conservatism of the AS interaction curve is due to the more conservative end points.

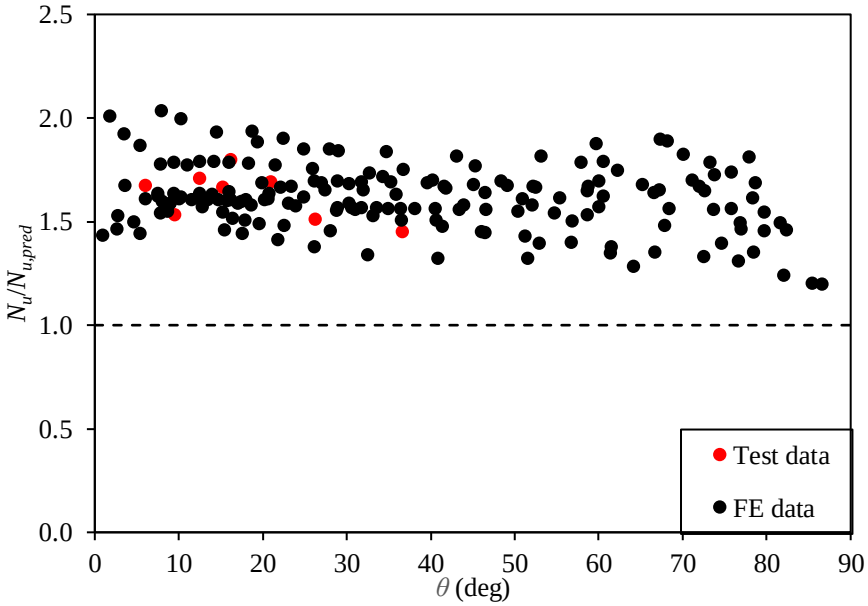

Figure 7.12: Comparisons of test and numerical failure loads with AS predicted failure loads.

7.4.4 ANSI/AISC 360-16 (AISC)

The applicability of the existing design rules in AISC 360 (AISC, 2016) to S960 ultra-high strength steel slender welded I-section beam-columns subjected to minor-axis combined loading is evaluated in this part. Specifically, the design interaction formulation is adopted, as defined by Equation (7.11), where P_s is the column buckling strength and can be calculated according to Clause 5.7 of AISC 360 (AISC, 2016), $M_{eff,z,AISC}$ is the AISC cross-section minor-axis effective moment resistance and determined by Equation (7.12), and α=1/(1-$N_{u,pred}/N_{cr}$) is the amplification factor to consider the second-order effect.

$$\begin{cases} \dfrac{N_{u,pred}}{P_s}+\dfrac{8}{9}\dfrac{\alpha M_{u,pred}}{M_{eff,z,AISC}}\le 1 & \text{for } \dfrac{N_{u,pred}}{P_s}\ge 0.2 \\ \dfrac{N_{u,pred}}{2P_s}+\dfrac{\alpha M_{u,pred}}{M_{eff,z,AISC}}\le 1 & \text{for } \dfrac{N_{u,pred}}{P_s}< 0.2 \end{cases} \tag{7.11}$$

$$M_{eff,z,AISC} = M_{el,z} \frac{0.69}{\left[b_f \Big/ \left(2t\sqrt{E / f_y}\right)\right]^2} \tag{7.12}$$

The applicability of AS design interaction expressions to S960 ultra-high strength steel slender welded I-section beam-columns subjected to minor-axis combined loading is assessed based on the comparisons of the predicted ultimate loads by AISC with the test and numerical failure loads. The mean test and numerical to AISC design ultimate load ratio $N_u/N_{u,pred}$ is 1.36 and the corresponding COV is 0.08, as tabulated in Table 7.4. A graphical evaluation was also performed, as shown in Figure 7.13. Both the quantitative and graphical assessments revealed that the AISC interaction curve yields consistent, though conservative, predictions of ultimate load for S960 UHSS slender welded I-section beam-columns subjected to minor-axis combined loading. Moreover, the predictions from the AISC interaction curve are less conservative than those from the EC3 and AS interaction curves. This can be attribute to the more accurate end points and shape of the AISC interaction curve.

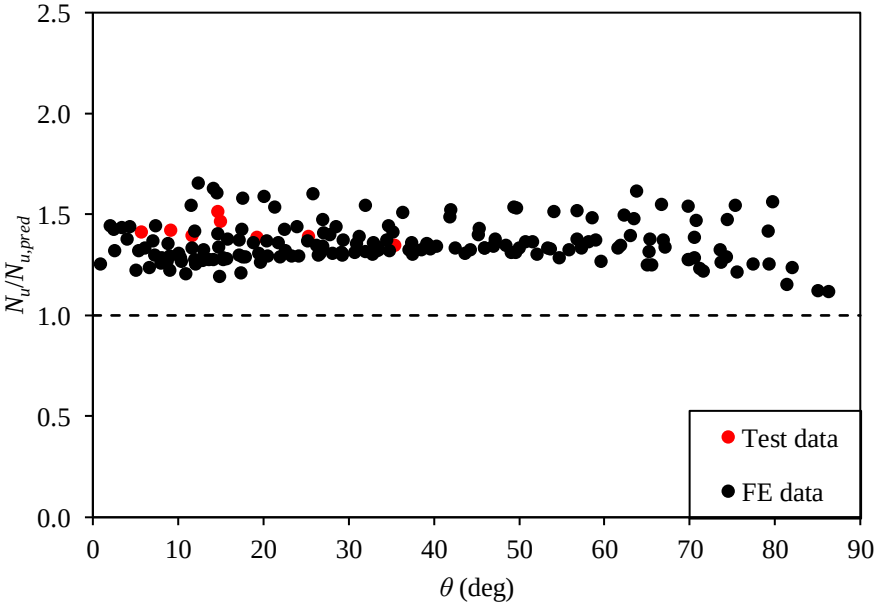

Figure 7.13: Comparisons of test and numerical failure loads with AISC predicted failure loads.

7.4.5 Improved design approach

The above design analysis results revealed that the codified interaction curves generally yield consistent but conservative predictions of ultimate load for S960 UHSS slender welded I-section beam-columns subjected to minor-axis combined loading. The accuracy of interaction curve is dependent on the shape (defined by the interaction/amplification factor) and end points (i.e. column buckling strength and minor-axis bending resistance). The predicted ultimate loads are generally consistent, as tabulated in Table 7.4, their shapes are thus considered appropriate. The conservatism of the codified interaction curves therefore results from the inaccurate end points. An improved design approach is therefore prompted, based on the EC3 interaction curve but with more accurate end points, with the design formulation expressed in Equation (7.13). The new compression end point N_{prop} is calculated by the buckling curve 'a' (with the imperfection factor of 0.21), which has been demonstrated to be accurate in predicting column buckling strengths, as detailed in Chapter 4. The direct strength method (DSM), is adopted to calculate the new bending end point M_{DSM}, as given by Equation (7.14), where $\lambda_c = \sqrt{f_y / f_{cr}}$ is the overall cross-section slenderness, in which f_{cr} is the cross-sectional critical buckling stress in bending and derived utilizing the finite strip software CUFSM.

$$\frac{N_{u,pred}}{N_{prop}} + k_z \frac{M_{u,pred}}{M_{DSM}} \leq 1 \tag{7.13}$$

$$\frac{M_{DSM}}{M_{el,z}} = \begin{cases} 1 & \text{for } \lambda_c \leq 0.776 \\ (1-\frac{0.15}{\lambda_c^{0.8}})\frac{1}{\lambda_c^{0.8}} & \text{for } \lambda_c > 0.776 \end{cases} \tag{7.14}$$

The ultimate load predictions for S960 UHSS slender welded I-section beam-columns subjected to minor-axis combined loading, as determined by the new interaction curve, were assessed against the numerical and test results. The evaluation

results, as shown in Figure 7.14 and Table 7.4, revealed that the new interaction curve yields more accurate predictions of ultimate load than the aforementioned codified interaction curves, with the mean $N_u/N_{u,pred}$ ratio of 1.28.

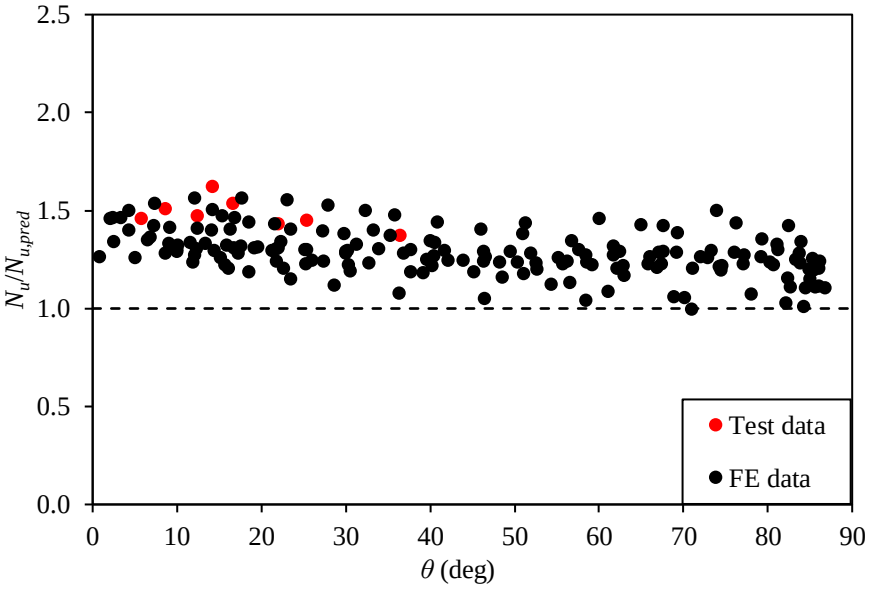

Figure 7.14: Comparisons of test and numerical failure loads with predicted failure loads from new design approach.

7.5 Concluding remarks

The buckling behaviour and resistances of S960 ultra-high strength steel slender welded I-section beam-columns have been investigated through a testing and numerical modelling programme. The testing programme included initial geometric imperfection measurements and minor-axis eccentric compression tests on eight beam-columns. Following the testing programme, a numerical modelling programme was conducted, in which the developed FE models were validated against the test results and adopted to perform the parametric study to generate further numerical data over a broad range of cross-section dimensions, member lengths and loading combinations. Then, the obtained experimental and numerical results were adopted

to evaluate the applicability of the codified design interaction provisions for S690 (or S700) high strength steel welded I-section beam-columns to their S960 ultra-high strength steel counterparts. It was revealed that all codified interaction curves yield conservative, though consistent, predictions of ultimate load, due to the conservative compression and bending end points. Lastly, a new design proposal, adopting the shape of the EC3 interaction curve but with more accurate compression end point (calculated from the buckling curve 'a') and bending end point (calculated from the DSM), has been devised, offering improved design accuracy.

CHAPTER 8

CONCLUSIONS AND SUGGESTIONS FOR FUTURE RESEARCH WORK

8.1 Conclusions

In this chapter, the key research findings of the research work, as detailed in previous chapters, are summarised, while more detailed concluding remarks are provided at the end of each chapter. The suggestions for future research follow thereafter.

Ultra-high strength steel grade S960, with the nominal yield stress of 960 MPa, has been gaining popularity in the automotive industries in the past decade, due to its superior strength-to-weight ratio. However, its actual use is restricted by the absence of the experimental data on ultra-high strength steel components and lack of the efficient design provisions. This thus prompted the current study on S960 ultra-high strength steel welded I-section components under different loading cases, with the aim of establishing the experimental data pool and devising the relating accurate design approaches.

The membrane residual stresses and local stability of S960 ultra-high strength steel welded I-section stub columns have been experimentally and numerically investigated in Chapter 3 (Su et al., 2021b). The pioneer data bank on S960 ultra-high strength steel welded I-sections has been established; on the basis of the measured data, a new predictive model that can well predict the membrane residual stress distributions and amplitudes in S960 ultra-high strength steel welded I-sections has been proposed. The applicability of the relevant codified slenderness limits and local

buckling design rules provided in EN 1993-1-12 (CEN, 2007), ANSI/AISC 360-16 (AISC, 2016) and AS 4100 (AS, 2016) to S960 ultra-high strength steel welded I-section stub columns has been assessed. The codified slenderness limits were found to be applicable to S960 ultra-high strength steel welded I-sections, and the codified local buckling design rules were shown to yield accurate and consistent cross-section resistance predictions.

In Chapters 4 and 5, experimental and numerical investigations of the member instability of S960 ultra-high strength steel welded I-section columns have been conducted (Su et al., 2021a, 2021e). The testing programme includes (i) ten pin-ended column tests on S960 ultra-high strength steel non-slender welded I-section columns failing by flexural buckling and (ii) ten pin-ended column tests on S960 ultra-high strength steel slender welded I-section columns susceptible to local–flexural interactive buckling, which are the world's first set of such tests. On the basis of the obtained test and numerical data, the applicability of the codified buckling curves, as given in EN 1993-1-12 (CEN, 2007), ANSI/AISC 360-16 (AISC, 2016) and AS 4100 (AS, 2016), for S690 or S700 high strength steel non-slender welded I-section columns failing by flexural buckling was assessed, with their design conservatism indicated. A new buckling curve based on the European code was proposed, leading to a higher level of design accuracy and consistency over the original Eurocode design buckling curve. The codified design provisions were also found to yield conservative resistance predictions for S960 ultra-high strength steel slender welded I-section columns susceptible to local–flexural interactive buckling. A new design approach was thus developed through the use of the newly proposed buckling curve combined with the EC3 effective width method, and it was shown to yield more accurate interactive buckling resistances than the codified design rules. These research findings and newly proposed design approaches can serve as a basis for future revisions of EN 1993-1-12 (CEN, 2007), ANSI/AISC 360-16 (AISC, 2016)

and AS 4100 (AS, 2016).

Chapter 6 investigates the local buckling behaviour and resistances of S960 high strength steel welded I-sections under combined compression and bending moment, which have been studied for the first time throughout the world (Su et al., 2021c, 2021d). This chapter reports the experimental and numerical investigations on S960 ultra-high strength steel welded I-section stub columns subjected to major-axis and minor-axis combined loading. On the basis of the obtained test and numerical data, the applicability of the codified design interaction curves and design provisions, as given in EN 1993-1-12 (CEN, 2007), AS 4100 (AS, 2016) and ANSI/AISC 360-16 (AISC, 2016), to S960 ultra-high strength steel welded I-sections under combined loading has been evaluated. The evaluation results revealed that all the three codified design interaction curves lead to unduly conservative and scattered failure load predictions for minor-axis and major-axis combined loading, mainly due to the adoption of the conservative end points.

In Chapter 7, the experimental and numerical investigations of the buckling behaviour and resistances of S960 ultra-high strength steel welded I-section beam-columns were investigated (Su et al., 2021f). A testing programme, including eight ultra-high strength steel welded I-section beam-column tests, has been conducted, followed by a numerical modelling programme. The test and numerical data have been adopted to examine the applicability of the design interaction curves and rules for S690 high strength steel welded I-section beam-columns, as given in EN 1993-1-12 (CEN, 2007), ANSI/AISC 360-16 (AISC, 2016) and AS 4100 (AS, 2016), to their S960 ultra-high strength steel counterparts. It was concluded that all codified interaction curves yield conservative, though consistent, predictions of ultimate load, due to the conservative bending and compression end points. Lastly, a new design proposal, adopting the shape of the EC3 interaction curve but with more accurate

compression end point (calculated from the buckling curve ‘a’) and bending end point (calculated from the DSM), has been devised, offering improved design accuracy.

To summarise, the thorough experimental and numerical investigations of the local, flexural and local–flexural buckling behaviour of S960 ultra-high strength steel welded I-section structural components under various types of loading (i.e. pure compression and combined compression and bending) have been conducted for the first time around the world and presented in this thesis. The codified design rules for each loading type of S690 (or S700) high strength steel welded I-section structural components have been fully discussed, with their applicability to S960 ultra-high strength steel counterparts assessed. Moreover, new design approaches for S960 ultra-high strength steel welded I-section columns have been proposed and shown to offer higher design accuracy and consistency. These research findings and new design methods will serve as a basis for future revisions of international design standards for S960 ultra-high strength steel structures.

8.2 Suggestions for future research

Based on the research work conducted in this thesis, suggestions for future research on S960 ultra-high strength steel welded I-section members are provided herein. Firstly, investigations into the behaviour and load-carrying capacities of S960 ultra-high strength steel welded I-section components under other loading types beyond those reported in the present thesis are required, for example, the shear buckling behaviour of S960 ultra-high strength steel welded I-section plate girders under shear force and the buckling behaviour of S960 ultra-high strength steel welded I-section beam-columns under moment gradients.

The global instability of S960 ultra-high strength steel welded I-section columns and beam-columns is influenced by the boundary conditions. In this thesis, pin-ended boundary conditions were applied onto both ends of each column or beam-column specimen. Future research could be conducted to investigate the global buckling behaviour of S960 ultra-high strength steel welded I-section columns and beam-columns with other boundary conditions, e.g., pinned-fixed and fixed-fixed end restraints.

While this thesis investigates the structural performance of S960 ultra-high strength steel welded I-sections, future research is required to cover other cross-section profiles, including closed tubular sections, T-sections, channel and angle sections. For non-doubly symmetric sections, torsional-related buckling would be triggered and special design attention should then be given to torsional buckling and flexural-torsional buckling in the future research.

Research into S960 ultra-high strength steel composite structures also remains unexplored. Further research could be extended to investigate the structural behaviour of composite components with concrete encasing S960 ultra-high strength steel I-section members, with the influence of the concrete on the structural response to be studied.

Finally, the structural performance of S960 ultra-high strength steel welded I-section components in fire (i.e. at elevated temperatures) and after exposure to fire (i.e. after exposure to elevated temperatures) requires investigations. Testing and numerical modelling can be performed to investigate their in-fire and post-fire behaviour and resistances under various types of loading, followed by the development of efficient design rules.

REFERENCES

ABAQUS. (2014) "ABAQUS/Standard User's Manual Volumes I-III and ABAQUS CAE Manual", Version 6.14, Hibbitt, Karlsson & Sorensen, Inc., Pawtucket, USA.

AISC. (2016) "ANSI/AISC 360-16: Specification for Structural Steel Buildings", American Institute of Steel Constructions (AISC), Chicago, Illinois, USA.

AISC. (1994) "Metric load and resistance factor design specification for structural steel buildings", American Institute of Steel Constructions (AISC), Chicago, Illinois, USA.

AS. (2016) "AS 4100-1998: Australian Standard – Steel Structures", The Committee BD-001, Steel Structures, Sydney, Australia.

Ban, H. and Shi, G. (2018) "A Review of Research on High-Strength Steel Structures", Proceedings of the Institurion of Civil Engineers – Structures and Buildings, Vol. 171, No. 8, pp. 625-641.

Ban, H., Shi, G., Shi, Y. and Wang, Y. (2012) "Overall Buckling Behavior of 460 MPa High Strength Steel Columns: Experimental Investigation and Design Method", Journal of Constructional Steel Research, Vol. 74, pp. 140-150.

Ban, H., Shi, G., Shi, Y. and Bradford, M.A. (2013) "Experimental Investigation of the Overall Buckling Behaviour of 960 MPa High Strength Steel Columns", Journal of Constructional Steel Research, Vol. 88, pp. 256-266.

Beg, D. and Hladnik, L. (1996) "Slenderness Limit of Class 3 I Cross-Sections Made

of High Strength Steel", Journal of Constructional Steel Research, Vol. 38, No. 3, pp. 201-217.

Boissonnade, N., Greiner, R., Jaspart, J. P. and Lindner, J. (2006) "Rules for Member Stability in EN 1993-1-1: Background Documentation and Design Guidelines", European Convention for Constructional Steelwork (ECCS).

Boissonnade, N., Jaspart, J. P., Muzeau, J. P. and Villette, M. (2002) "Improvement of the Interaction Formulae for Beam Columns in Eurocode 3", Computers & structures, Vol. 80, No. 27, pp. 2375-2385.

Boissonnade, N., Jaspart, J. P., Muzeau, J. P. and Villette, M. (2004) "New Interaction Formulae for Beam-Columns in Eurocode 3: The French–Belgian Approach", Journal of Constructional Steel Research, Vol. 60, pp. 421-431.

BSK. (2003) "Swedish Regulations for Steel Structures, BSK 99", Swedish National Board of Housing, Building and Planning (Boverket), Sweden.

Bu, Y. and Gardner, L. (2018) "Local Stability of Laser-Welded Stainless Steel I-Sections in Bending", Journal of Constructional Steel Research, Vol. 148, pp. 49-64.

Buchanan, C., Real, E. and Gardner, L. (2018) "Testing, Simulation and Design of Cold-Formed Stainless Steel CHS Columns", Thin-Walled Structures, Vol. 130, pp. 297-312.

CEN. (2005) "Eurocode 3 – Design of Steel Structures – Part 1-1: General rules and rules for buildings", European Standards Committee (CEN), Brussels, Belgium.

CEN. (2006) "Eurocode 3 – Design of Steel Structures – Part 1-5: Plated Structural

Elements", European Standards Committee (CEN), Brussels, Belgium.

CEN. (2007) "Eurocode 3 – Design of Steel Structures – Part 1-12: Additional Rules for the Extension of EN 1993 up to Steel Grades S700", European Standards Committee (CEN), Brussels, Belgium.

CEN. (2016) "EN ISO 6892-1: Metallic Materials – Tensile Testing – Part 1: Method of Test at Room Temperature", European Standards Committee (CEN), Brussels, Belgium.

Centre for Advanced Structural Engineering. (1990) "Compression Tests of Stainless Steel Tubular Columns", Investigation Report S770, University of Sydney, Australia.

Chen, C., Chiew, S., Zhao, M., Lee, C. and Fung, T. (2019) "Welding Effect on Tensile Strength of Grade S690Q Steel Butt Joint", Journal of Constructional Steel Research, Vol. 153, pp. 153-168.

Chen, M. and Young, B. (2020) "Beam-column tests of cold-formed steel elliptical hollow sections", Engineering Structures. Vol. 210, 109911.

ECCS. (1976) "Manual on Stability of Steel Structures", Second edition, European Convention for Constructional Steelwork (ECCS) – Committee 8 – Stability, Brussels, Belgium.

EN 10025-6. (2019) "Hot-rolled Products of Structural steels. Technical Delivery Conditions for Flat Products of High Yield Strength Structural Steels in the Quenched and Tempered Condition", European Committee for Standardization (CEN), Brussels, Belgium.

Fang, H., Chan T. and Young, B. (2018) “Material Properties and Residual Stresses of Octagonal High Strength Steel Hollow Sections”, Journal of Constructional Steel Research, Vol. 148, pp. 479-490.

Fukumoto, Y. (1998) “New Constructional Steels and Structural Stability”, Engineering Structures, Vol. 18, No. 10, pp. 786-791.

Gardner, L., Bu, Y. and Theofanous, M. (2016) “Laser-Welded Stainless Steel I-Sections: Residual Stress Measurements and Column Buckling Tests”, Engineering Structures, Vol. 127, pp. 536-548.

Gardner, L. and Nethercot, D.A. (2004a) “Experiments on Stainless Steel Hollow Sections – Part 1: Material and Cross-Sectional Behaviour”, Journal of Constructional Steel Research, Vol. 60, No. 9, pp. 1291-1318.

Gardner, L. and Nethercot, D.A. (2004b) “Numerical Modeling of Stainless Steel Structural Components – A Consistent Approach”, Journal of Structural Engineering (ASCE), Vol. 130, No. 10, pp. 1586-1601.

MOHURD (2003) “Code for design of steel structures”, Ministry of Housing and Urban-Rural Development of the People’s Republic of China, GB 50017-2003, Beijing [in Chinese].

Green, P.S., Sause, R. and Ricles, J.M. (2002) “Strength and Ductility of HPS Flexural Members”, Journal of Constructional Steel Research, Vol. 58, No. 5-8, pp. 907-941.

Greiner, R. (2001) “Background Information on the Beam-Column Interaction Formulae at Level 1”, ECCS TC8, Report No. 2001-021.

Greiner, R. and Lindner, J. (2006) “Interaction Formulae for Members Subjected to Bending and Axial Compression in EUROCODE 3 – the Method 2 Approach”, Journal of Constructional Steel Research, Vol. 62. No. 8, pp. 757-770.

IABSE. (2005) “Use and Application of High-Performance Steels for Steel Structures”, International Association for Bridge and Structural Engineering (IABSE), ETH Zürich, Switzerland.

Kim, D.K., Lee, C.H., Han, K.H., Kim, J.H., Lee, S.E. and Sim H.B. (2014) “Strength and Residual Stress Evaluation of Stub Columns Fabricated from 800 MPa High-Strength Steel”, Journal of Constructional Steel Research, Vol.102, pp. 111-120.

Kim, T.S., Lee, M.J., Oh, Y.S., Lee, K.M. and Kim D.H. (2012) “A Study on Compressive Strength of Built-up H Shaped Columns Fabricated with HSA800 High Performance Steels”, Journal of Korean Society of Steel Construction, Vol. 24, No. 6, pp. 627-636. [in Korean]

Langenberg, P. (2008) “Relation between Design Safety and Y/T Ratio in Application of Welded High Strength Structural Steels”, Proceedings of International Symposium on Applications of High Strength Steels in Mordern Constructions and Bridges – Relationship of Design Specifications, Safety and Y/T Ratio, Beijing, China, pp. 28-46.

Langenberg, P., Niessen, T. and Dahl, W. (2000) “Bruch-und Verformungsverhalten von hochfesten Staehlen mit Streckgrenzen von 690 bis 890 MPA”, Stahlbau, Vol. 69, pp. 283-291.

Le, T., Paradowska, A., Bradford, M., Liu, X. and Valipour, H. (2020) "Residual Stresses in Welded High-Strength Steel I-Beams", Journal of Constructional Steel Research, Vol. 167, 105849.

Lee, C.H., Han, K.H., Uang, C.M., Kim, D.K., Park, C.H. and Kim, J.H. (2013) "Flexural Strength and Rotation Capacity of I-Shaped Beams Fabricated from 800-MPa Steel", Journal of Structural Engieering (ASCE), Vol. 139, No. 6, pp. 1043-1058.

Li, D., Huang, Z., Uy, B., Thai, H. and Hou, C. (2019) "Slenderness Limits for Fabricated S960 Ultra-High-Strength Steel and Composite Columns", Journal of Constructional Steel Research, Vol. 159, pp. 109-121.

Li, D., Paradowska, A., Uy, B., Wang, J. and Khan, M. (2020) "Residual Stresses of Box and I-Shaped Columns Fabricated from S960 Ultra-High-Strength Steel", Journal of Constructional Steel Research, 2020, 105904.

Li, G., Wang, Y. and Chen, S. (2015) "The Art of Application of High-Strength Steel Structures for Buildings in Seismic Zones", Advanced Steel Construction, Vol. 11, No. 4, pp. 492-506.

Li, G., Yan, X. and Chen, S. (2012) "Experimental Study on Bearing Capacity of Welded H-Section Columns Using Q460 High Strength Steel under Bending and Axial Compression", Journal of Building Structures, Vol. 33, No. 12, pp. 31-37. [in Chinese]

Li, G., Lyu, H. and Zhang, C. (2017) "Post-Fire Mechanical Properties of High Strength Q690 Structural Steel", Journal of Constructional Steel Research, Vol. 132,

pp. 108-116.

Li, T., Li, G., Chan, S. and Wang, Y. (2016) “Behavior of Q690 High-Strength Steel Columns: Part 1: Experimental Investigation”, Journal of Constructional Steel Research, Vol. 123, pp. 18-30.

Li, H. and Young, B. (2018) “Residual Mechanical Properties of High Strength Steels after Exposure to Fire”, Journal of Constructional Steel Research, Vol. 148, pp. 562-571.

Lindner, J. (1997) “Design of Steel Beams and Beam Columns”, Engineering Structures, Vol. 19, No. 5, pp. 378-384.

Lindner, J. (2003) “Design of Beams and Beam Columns”, Progress in Structural Engineering and Materials, Vol. 5, No. 1, pp. 38-47.

Liu, X. and Chung, K.F. (2018) “Experimental and Numerical Investigation into Temperature Histories and Residual Stress Distributions of High Strength Steel S690 Welded H-Sections”, Engineering Structures, Vol. 165, pp. 396-411.

Ma, J., Chan, T., and Young, B. (2015) “Material properties and residual stresses of cold-formed high strength steel hollow sections”, Journal of Constructional Steel Research, Vol. 109, pp. 152-165.

Ma, T., Hu, Y., Liu, X., Li, G. and Chung, K. (2017) “Experimental Investigation into High Strength Q690 Steel Welded H-Sections under Combined Compression and Bending”, Journal of Constructional Steel Research, Vol. 138, pp. 449-462.

Ma, T., Li, G. and Chung, K. (2018a) “Numerical Investigation into High Strength

Q690 Steel Columns of Welded H-Sections under Combined Compression and Bending", Journal of Constructional Steel Research, Vol. 144, pp. 119-134.

Ma, T., Liu, X., Hu, Y., Chung, K. and Li, G. (2018b) "Structural Behaviour of Slender Columns of High Strength S690 Steel Welded H-Sections under Compression", Engineering Structures, Vol. 157, pp. 75-85.

McDermott, J.F. (1969) "Plastic Bending of A514 Steel Beams", Journal of Structural Division (ASCE), Vol. 95, No. 9, pp. 1851-1871.

Qiang, X., Bijlaard, F. and Kolstein, H., (2013) "Post-Fire Performance of Very High Strength Steel S960", Journal of Constructional Steel Research, Vol. 80, pp. 235-242.

Rasmussen, K.J.R. and Hancock, G.J. (1992) "Plate Slenderness Limits for High Strength Steel Sections", Journal of Constructional Steel Research, Vol. 23, No. 1-3, pp. 73-96.

Rasmussen, K.J.R. and Hancock, G.J. (1995) "Tests of High Strength Steel Columns", Journal of Constructional Steel Research, Vol. 34, No. 1, pp. 27-52.

Rusch, A. and Lindner, J. (2004) "Application of Level 1 Interaction Formulae to Class 4 Sections", Thin-Walled Structures, Vol. 42, No. 2, pp. 279-293.

Saliba, N. and Gardner, L. (2013) "Cross-section Stability of Lean Duplex Stainless Steel Welded I-Sections", Journal of Constructional Steel Research, Vol. 80, pp. 1-14.

Schafer, B.W. and Peköz, T. (1998) "Computational Modeling of Cold-Formed Steel: Characterizing Geometric Imperfections and Residual Stresses", Journal of

Constructional Steel Research, Vol. 47, No. 3, pp. 193-210.

Shi, G., Ban, H. and Bijlaard, F.S.K. (2012) "Tests and Numerical Study of Ultra-High Strength Steel Columns with End Restraints", Journal of Constructional Steel Research, Vol. 70, pp. 236-247.

Shi, G., Zhou, W., Bai, Y. and Lin, C. (2014) "Local Buckling of 460 MPa High Strength Steel Welded Section Stub Columns under Axial Compression", Journal of Constructional Steel Research, Vol. 100, pp. 60-70.

Shi, G., Zhou, W. and Lin, C. (2015) "Experimental Investigation on the Local Buckling Behavior of 960 MPa High Strength Steel Welded Section Stub Columns", Advances in Structural Engineering, Vol. 18, No. 3, pp. 423-437.

Shi, G., Zhu, X. and Ban, H. (2016) "Material Properties and Partial Factors for Resistance of High-Strength Steels in China", Journal of Constructional Steel Research, Vol. 121, pp. 65-79.

Su, A., Sun, Y., Liang, Y. and Zhao, O. (2020) "Material Properties and Membrane Residual Stresses of S690 High Strength Steel Welded I-sections after Exposure to Elevated Temperatures", Thin-Walled Structures, 2020, 106723.

Su, A., Liang, Y. and Zhao, O. (2021a) "Experimental and Numerical Studies of S960 Ultra-High Strength Steel Welded I-Section Columns", Thin-Walled Structures, 2021, 107166.

Su, A., Sun, Y., Liang, Y. and Zhao, O. (2021b) "Membrane Residual Stresses and Local Stability of S960 Ultra-High Strength Steel Welded I-Section Stub Columns",

Thin-Walled Structures, 2021, 107497.

Su, A., Sun, Y., Liang, Y. and Zhao, O. (2021c) "Experimental and Numerical Studies of S960 Ultra-High Strength Steel Welded I-Sections Under Combined Compression and Minor-Axis Bending", Engineering Structures, 243, 112675.

Su, A., Sun, Y., Zhao, O and Liang, Y. (2021d) "Local Buckling of S960 Ultra-High Strength Steel Welded I-Sections Subjected to Combined Compression and Major-Axis Bending", Engineering Structures, 248,113213.

Su, A., Sun, Y., Liang, Y. and Zhao, O (2021e) "Local–Flexural Interactive Buckling of S960 Ultra-High Strength Steel Slender Welded I-section Columns", Thin-Walled Structures, Under Review.

Su, A., Sun, Y., Liang, Y. and Zhao, O (2021f) "Testing, numerical modelling and design of S960 Ultra-High Strength Steel Welded I-section Beam-Columns", Thin-Walled Structures, Under Review.

Su, A., Liang, Y. and Zhao, O. (2021g) "Post-fire behaviour and resistances of S690 high strength steel welded I-section stub columns", Thin-walled Structures, 169, 108422.

Sun, Y., Liang, Y. and Zhao, O. (2019a) "Testing, Numerical Modelling and Design of S690 High Strength Steel Welded I-Section Stub Columns", Journal of Constructional Steel Research, Vol. 159, pp. 521-533.

Sun, Y., Liang, Y. and Zhao, O. (2019b) "In-Plane Bending Behaviour and Capacities of S690 High Strength Steel Welded I-Section Beams", Journal of Constructional

Steel Research, Vol. 162, 105741.

Sun, Y., Liang, Y. and Zhao, O. (2020) “Minor-Axis Flexural Buckling Behaviour and Resistances of Pin-Ended S690 High Strength Steel Welded I-Section Columns”, Thin-Walled Structures, Vol. 156, 106980.

Sun, Y., Liang, Y., Zhao, O. and Young, B. (2021a) “Experimental and numerical investigations of S690 high strength steel welded I-sections under combined compression and bending”, Journal of Structural Engineering (ASCE), Vol. 147, No. 5, 04021054.

Sun, Y., Liang, Y., Su, A. and Zhao, O. (2021b) “Local–Flexural Interactive Buckling of S690 High Strength Steel Slender Welded I-Section Columns: Testing, Modelling and Design”, Thin-Walled Structures, Vol. 166, 108064.

Taras, A. (2016) “Derivation of DSM-Type Resistance Functions for In-Plane Global Buckling of Steel Beam-Columns”, Journal of Constructional Steel Research, Vol. 125, pp. 95-113.

Tebedge, N., Alpsten, G. and Tall, L. (1973) “Residual-Stress Measurement by the Sectioning Method”, Experimental Mechanics, Vol. 13, No. 2, pp. 88-96.

Wang, F., Zhao, O., and Young B. (2019) “Flexural behaviour and strengths of press-braked S960 ultra-high strength steel channel section beams”, Engineering Structures, Vol. 200, 109735.

Wang, J., Afshan, S., Gkantou, M., Theofanous, M., Baniotopoulos, C., Gardner, L. (2016) “ Flexural behaviour of hot-finished high strength steel square and rectangular

hollow sections", Journal of Constructional Steel Research, Vol. 121 pp. 97-109.

Wang, J. and Gardner, L. (2017) "Flexural Buckling of Hot-Finished High-Strength Steel SHS and RHS Columns", Journal of Structural Engineering (ASCE), Vol. 143, No. 6, 04017028.

Wang, Y., Li, G. and Chen, S. (2012a) "Residual Stresses in Welded Flame-Cut High Strength Steel H-Sections", Journal of Constructional Steel Research, Vol. 79, pp.159-165.

Wang, Y., Li, G., Chen, S. and Sun, F. (2012b) "Experimental and Numerical Study on the Behavior of Axially Compressed High Strength Steel Columns with H-Section", Engineering Structures, Vol. 43, pp. 149-159.

Walport, F., Gardner, L., Real, E., Arrayago, I. and Nethercot, D.A. (2019) "Effects of material nonlinearity on the global analysis and stability of stainless steel frames", Journal of Constructional Steel Research, Vol. 152, pp. 173-182.

Winter, G. (1947) "Strength of Thin Steel Compression Flanges", Transactions of the American Society of Civil Engineers, Vol. 112, No. 1, pp. 527-554.

Yoo, J.H., Kim, J.W., Yang, J.G., Kang, J.W. and Lee, M.J. (2013) "Local Buckling in the Stub Columns Fabricated with HSA800 of High Performance Steel", International Journal of Steel Structures. Vol. 13, No. 3, pp. 445-458.

Yuan, H., Wang, Y., Gardner, L., Du, X. and Shi, Y. (2015) "Local – Overall Interactive Buckling Behaviour of Welded Stainless Steel I-Section Columns", Journal of Constructional Steel Research, Vol. 111, pp. 75-87.

Zhao, O., Gardner. L. and Young, B. (2016) “Testing and Numerical Modelling of Austenitic Stainless Steel CHS Beam–Columns”, Engineering Structures, Vol. 111, pp. 263-274.

Zhao, O., Rossi, B., Gardner, L., Young, B. (2015) “Behaviour of structural stainless steel cross-sections under combined loading - Part I: Experimental study”, Engineering Structures, Vol. 89, pp. 236-246.

Zhou, F., Tong, L. and Chen, Y. (2013) “Experimental and Numerical Investigations of High Strength Steel Welded H-Section Columns”, International Journal of Steel Structures, Vol. 13, No. 2, pp. 209-218.

Ziemian, R.D. (2010) “Guide to Stability Design Criteria for Metal Structures”, Sixth edition, John Wiley & Sons, Inc., Hoboken, New Jersey, US.